Dielectric measurements at GHz frequencies

Master Thesis verfasst von

Lars Wendel

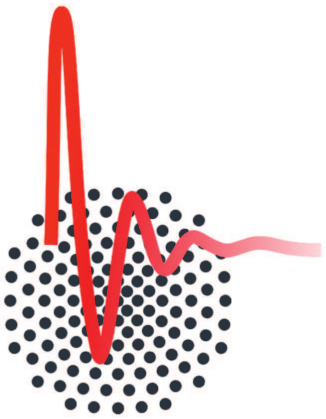

1. Physikalisches Institut
Universität Stuttgart

Hauptberichter	**Prof. Dr. Martin Dressel**
Mitberichter	**Prof. Dr. Jörg Wrachtrup**
Betreuer	**Dr. Marc Scheffler**
	Nikolaj Ebensperger

09. April 2019

Contents

1. Motivation

Amongst the many dielectric materials that are topic of present research, two examples might be mentioned: $SrTiO_3$ and nano-confined water molecules in single crystals.
In $SrTiO_3$ a quantum paraelectric or incipient ferroelectric behavior can be observed [1]. For low temperatures $SrTiO_3$ is in a paraelectric phase, and the dielectric constant as a function of temperature follows a Curie-Weiss behavior. However, a real phase transition is not fully reached, indicated by the absence of a divergence in the permittivity at lowest observable temperatures. Quantum fluctuations then start to come into play and stabilize the frequency of the soft mode which leads to a saturation of the permittivity [2]. The dielectric constant of $SrTiO_3$ is strongly anisotropic and depends vastly on temperature and frequency range and can go up to around 20000 [3, 4].
To confine water molecules in single crystals and observe the (quantum) paraelectric behavior, suitable hosts are needed. Possible candidates are single crystals of beryl or cordierite belonging to the gemstone family, where the water molecules are confined in structural channels [5, 6]. These large open channels run parallel to the crystal c-axis. In beryl the channels consist of six SiO_4 tetrahedral rings, while in cordierite they consist of four SiO_4 and two AlO_4 tetrahedral rings. The water molecules are trapped in the center of the channels during the growth process and can occur in two distinct orientations: Either the electric dipole is perpendicular (type I) or parallel (type II) to the c-axis. For type I paraelectric behavior of the water molecules can be observed. This is due to the prevented hydrogen bonding, while the dipole-dipole interactions are kept which results in incipient ferroelectricity. The dielectric permittivity follows a Curie-Weiss behavior and saturates for low temperatures due to quantum fluctuations [6]. Whereas the permittivity of $SrTiO_3$ ranges up to very large values, the dielectric constant of confined water molecules only goes up to around 20. Measurements were performed up to THz frequencies, where especially the cordierite system lacks information about the microwave regime. The different frequency regimes require separate approaches to probe the sample under study [7–9]
Different high frequency dielectric measurement techniques can access the desired dielectric properties in the GHz range of the bulk material. The methods can be roughly classified in four categories: Transmission and reflection line techniques, free-space methods, open-ended coaxial-probe techniques and resonant techniques [10–14]. Each technique has advantages and limitations regarding sample material and shape and which frequencies are possible to probe. Generally, the measurement methods can be classified if discrete frequencies are measured or the measurement is of broadband type. In broadband approaches the electromagnetic wave passes the material and allows to access frequencies continuously over a wide range. An example is the transmission line method where frequencies from the MHz up to the GHz range can be accessed [15]. However, this method lacks heavily in accuracy due to the non-resonant fixture type. Furthermore, unwanted parasitic losses occur in the microwave regime, strongly

influencing the measurement. Since the accuracy is of major interest, resonant techniques are suited for bulk dielectric measurements [16–18]. The obtained results are of highest accuracy compared to the other mentioned techniques. However, one big disadvantages is the accessibility of only a single frequency. The different resonant approaches are directly fabricated for the sample under test and are therefore able to probe only a single frequency in the spectrum. Especially regarding frequency-dependent dielectric properties this is an enormous weakness.
Microwave waveguide resonator utilize the cavity perturbation theory and are able to probe numerous discrete frequencies [19]. Most of all, planar microwave resonators provide a wide field of potential researches [20–24]. It is possible to probe higher harmonics of a fundamental resonance frequency and perform measurements at cryogenic temperatures, while remaining at highly accurate results. A further upside is the simple fabrication of the the planar resonators as well as an fast and straightforward sample preparation of the studied materials. However, planar waveguide resonators are used for studies on dielectric thin films [25], whereas probing bulk dielectrics with this method is a recent research area.
In this thesis a new resonant approach for bulk dielectric samples is developed in the microwave regime up to 20 GHz. With simulations utilized, different possible approaches are firstly studied regarding their suitability and functionality. This is investigated with focusing on the challenges which occur by going from thin films under study to bulk dielectrics. The respective approaches are then tested within experiments to check the simulated predictions. Finally, a new method is established by measuring known dielectrics and comparing the results to the literature.
This thesis begins with a short guide into fundamental theoretical principles required for characterizing resonators and the analysis of microwave resonator experiments. Afterwards, the state of art of high frequency dielectric measurements is presented including several exemplary methods. Following, simulation and experimental basics and the consistency between them are elucidated. The first approach where the bulk dielectric sample acts as perturbation to the waveguide is then discussed for two different planar resonator structures. The new method with the resonator directly shaped on the sample under study is subsequently analyzed and discussed in detail including model requirements, simulations and experiments on TiO_2, MgO and $LaAlO_3$. This work finishes with an outlook for possible future experiments for the established resonant approach.

2. Theoretical principles

2.1. Theory of electromagnetic waves in matter

To describe the propagation of electromagnetic waves in matter, Maxwell's equations must be solved. The presence of a medium with certain properties such as electric dipoles or magnetic moments can change the propagation drastically. With this included, Maxwell's equations read in their general form [26]

$$\nabla \times \mathbf{E} + \frac{1}{c}\frac{\partial \mathbf{B}}{\partial t} = 0 \tag{2.1}$$

$$\nabla \cdot \mathbf{B} = 0 \tag{2.2}$$

$$\nabla \times \mathbf{H} - \frac{1}{c}\frac{\partial \mathbf{D}}{\partial t} = \frac{4\pi}{c}\mathbf{J} \tag{2.3}$$

$$\nabla \cdot \mathbf{D} = 4\pi\rho\,, \tag{2.4}$$

with c the velocity of light in free space, $\mathbf{J}$ being a current density and ρ a charge density. Apart from the electric field strength $\mathbf{E}$ and the magnetic induction $\mathbf{B}$, the magnetic field strength $\mathbf{H}$ and the dielectric displacement $\mathbf{D}$ also occur in the equations. These quantities are connected through material parameters via [26]

$$\mathbf{D} = \epsilon_1 \mathbf{E} = \mathbf{E} + 4\pi\mathbf{P} \tag{2.5}$$

$$\mathbf{B} = \mu_1 \mathbf{H} = \mathbf{H} + 4\pi\mathbf{M}\,. \tag{2.6}$$

Here, the permittivity (or dielectric constant) ϵ_1 and the permeability μ_1 are introduced, as well as the polarization density $\mathbf{P}$ and the magnetization $\mathbf{M}$. Since the response of the medium can experience not only a change in magnitude but a phase shift, the dielectric constant $\hat{\epsilon}$ needs to be defined to be complex [26]

$$\hat{\epsilon} = \epsilon_1 + i\epsilon_2 = \epsilon_1 + i\frac{4\pi\sigma_1}{\omega} \tag{2.7}$$

$$= 1 + i\frac{4\pi}{\omega}\hat{\sigma}\,, \tag{2.8}$$

with ω the angular frequency of the electric field. At last, the complex conductivity $\hat{\sigma}$ was introduced. The conductivity and the dielectric function are two fundamental properties in optical studies, while focusing on the permittivity $\hat{\epsilon}$ in this work.
Note that all equations, as well as the quantities are formulated in Gaussian units (cgs).

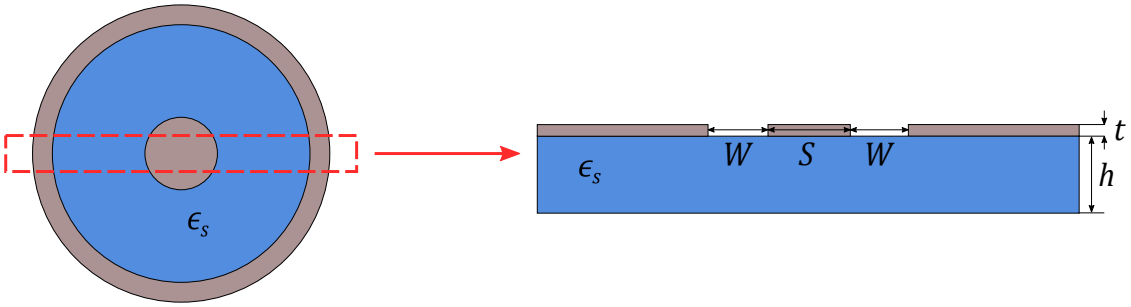

Fig. 2.1.: Schematic cross-section of a coplanar waveguide and its derivation from a coaxial cable. Geometric parameters of a CPW are depicted.

2.2. Microwave waveguides

Different types of structures such as coplanar waveguides [20, 27, 28], microstrips [29, 30] or striplines [21, 31, 32] provide a wide field of potential applications in the interest of microwave spectroscopy. It is possible to perform measurements over large frequency and temperature ranges [22, 33, 34]. A prominent example to probe interesting materials with the help of microwave waveguides are ESR studies [35–37]. This work is focusing on two of the structures: Firstly, the coplanar waveguide including the conformal mapping technique for the calculation of important parameters, and secondly, the microstrip examined with and without sample.

2.2.1. Coplanar waveguide resonators

The coplanar waveguide (CPW) was invented by C. P. Wen in 1969 [38] and has since been progressed in various applications [39, 40]. There are different types of CPWs, whereas concentrating on the conventional coplanar waveguide in this work [41]. In figure 2.1 a fundamental cross-section as well as the derivation from a coaxial cable can be seen. On the top surface of a dielectric substrate there is the conductive layer with thickness t shaping a center conductor with width S with ground planes on either side separated by a gap with width W. This allows the propagation of a quasi-TEM mode with low dispersion [42]. The fabrication process is simplified due to one single conducting layer on top of a substrate compared to a microstrip or stripline design [43].

One possibility to apply coplanar waveguides in microwave spectroscopy is by creating a resonant structure. This can be achieved in two ways: Either by implementing gaps in the center conductor forming a $\lambda/2$-resonator or via inductively coupling a further center conductor forming a $\lambda/4$-resonator, both visualized in figure 2.2.
In terms of the $\lambda/2$-resonator, the gaps separated at a certain distance l act as impedance mismatch. The propagating waves are partially reflected and due to interference a standing wave forms between the gaps if the resonance condition

$$\nu_n = \frac{nc}{2l\sqrt{\epsilon_{\text{eff}}}}\,, \tag{2.9}$$

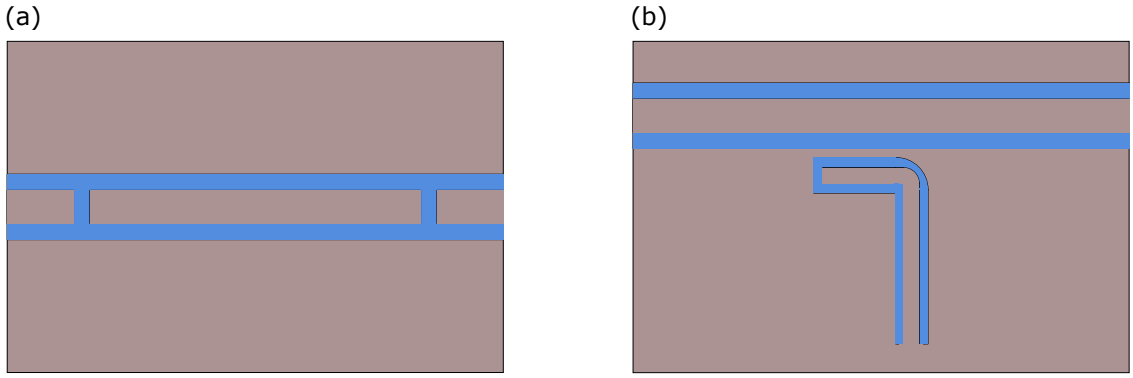

Fig. 2.2.: Schematic top view of (a) a CPW $\lambda/2$-resonator and (b) a CPW $\lambda/4$-resonator.

with ν_n the resonance frequency of the nth-mode, ϵ_{eff} the effective dielectric constant and n being a positive integer is met. By increasing the frequency, higher harmonics can be easily excited, where $(n = 1)$ corresponds to the fundamental frequency. The transmission enhances when the resonator is excited.
As regards the $\lambda/4$-resonator, there are no gaps in the central conductor, meaning it is acting as a simple transmission line, a so-called feedline. The resonator with length l is then coupled inductively with a closed end and parallel part next to the feedline allowing the propagating waves to excite the resonator. Similar to above a standing wave pattern forms with the resonance condition

$$\nu_n = \frac{nc}{4l\sqrt{\epsilon_{\text{eff}}}}\,, \tag{2.10}$$

causing a reduction in the transmission through the feedline. Higher harmonics can be excited, but only odd multiples $(n = 3, 5, 7, ...)$ of the fundamental frequency $(n = 1)$.
The excitation at the resonance frequency ν_n giving rise to an enhancement of the transmission for a $\lambda/2$-resonator or a reduction for a $\lambda/4$-resonator, respectively, can be described by a Lorentzian function [26]

$$L(\nu) = L_0 \frac{\nu_{\text{B}}}{(\nu - \nu_n)^2 + \nu_{\text{B}}^2}\,, \tag{2.11}$$

with an amplitude L_0 and the full width at half maximum (FWHM) ν_{B}. For a $\lambda/2$-resonator L_0 is positive, whereas it is negative for a $\lambda/4$-resonator.
The quality factor Q is a good measure for the losses in a resonator. It is defined by the total energy stored in the resonator divided by the energy dissipated each cycle. Thus, the quality factor can characterize the energy of the wave or the number of photons in the resonator and for microwave resonators it can be found by [44]

$$Q = \frac{\nu_0}{\nu_{\text{B}}}\,. \tag{2.12}$$

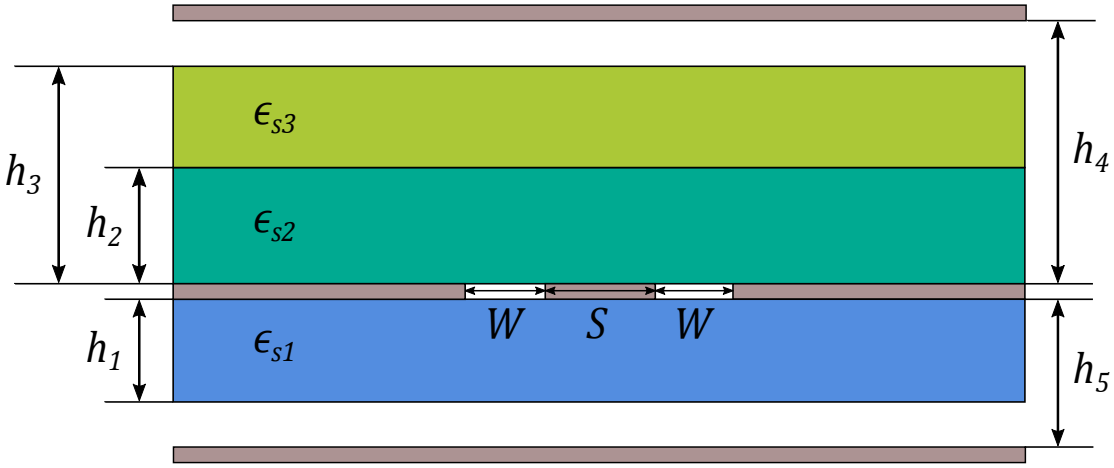

Fig. 2.3.: Cross-section of a triple-layered structure of a coplanar waveguide between two conductive shields placed at bottom and top.

The quality factor states information regarding the performance of the resonator. However, the so-called loaded quality factor Q_L which is obtained in the measurements, is made up of all quality factors in the systems. It is defined by [44]

$$\frac{1}{Q_\mathrm{L}} = \frac{1}{Q_\mathrm{i}} + \frac{1}{Q_\mathrm{e}}\,, \tag{2.13}$$

with the internal quality factor Q_i and the external quality factor Q_e, induced by the external circuit. If the resonator is undercoupled, it holds $Q_\mathrm{i}/Q_\mathrm{e} \ll 1$. The measured quality factor is then determined by the internal quality factor $Q_\mathrm{L} \approx Q_\mathrm{i}$.

Conformal mapping method

For the determination of fundamental properties of the coplanar waveguide the conformal mapping technique can be applied [41, 43, 45]. With that, closed form expressions for the effective dielectric constant ϵ_eff (introduced in equation (2.9)) and impedance Z_0 are obtained. Within this technique the CPW is split into partial regions. The electric field is assumed to fill each region homogeneously. Consequently, the capacitance of each part is found and the sum gives the total capacitance. The effective dielectric constant ϵ_eff is then calculated by the ratio of the total capacitance of the CPW and the capacitance in absence of all dielectrics. Requirements for this technique are that the conductors have perfect conductivity, the structure is considered lossless, the dielectric substrates are isotropic and that the electric field fills each partial region perfectly.

In figure 2.3 a triple-layered structure of a coplanar waveguide is depicted. On top of a ground substrate with height h_1 and dielectric constant $\epsilon_{\mathrm{s}1}$ the conducting parts are displayed. Above there are two additional dielectric layers with $h_2, \epsilon_{\mathrm{s}2}$ and $h_3, \epsilon_{\mathrm{s}3}$, respectively. Two conducting shields are placed at a distance h_4 and h_5 from the CPW conductor. The total capacitance C_CPW is found as mentioned above via

$$C_\mathrm{CPW} = C_1 + C_2 + C_3 + C_\mathrm{air}\,, \tag{2.14}$$

with expressions for each partial capacitance [46]

$$C_1 = 2\epsilon_0(\epsilon_{s1} - 1)\frac{K(k_1)}{K(k_1')} \tag{2.15}$$

$$C_2 = 2\epsilon_0(\epsilon_{s2} - \epsilon_{s3})\frac{K(k_2)}{K(k_2')} \tag{2.16}$$

$$C_3 = 2\epsilon_0(\epsilon_{s3} - 1)\frac{K(k_3)}{K(k_3')} \tag{2.17}$$

$$C_{air} = 2\epsilon_0\left(\frac{K(k_4)}{K(k_4')} + \frac{K(k_5)}{K(k_5')}\right). \tag{2.18}$$

Here, C_{air} consists of the two capacitances, above and below the stack of dielectric layers. The modulus k_i of the complete elliptic integral $K(k_i)$ introduced in equation (2.15) - (2.18) is given for each layer by [46]

$$k_i = \frac{\sinh(\frac{\pi}{4h_i}S)}{\sinh(\frac{\pi}{4h_i}(S+2W))} \quad i = 1,2,3 \tag{2.19}$$

$$k_i' = \sqrt{1-k_i^2}\,, \tag{2.20}$$

and for the air by

$$k_j = \frac{\tanh(\frac{\pi}{4h_j}S)}{\tanh(\frac{\pi}{4h_j}(S+2W))} \quad j = 4,5 \tag{2.21}$$

$$k_j' = \sqrt{1-k_j^2}\,. \tag{2.22}$$

The effective dielectric constant of the triple-layered structure is found next via [46]

$$\epsilon_{eff} = \frac{C_{CPW}}{C_{air}} = 1 + q_1(\epsilon_{s1} - 1) + q_2(\epsilon_{s2} - \epsilon_{s3}) + q_3(\epsilon_{s3} - 1)\,, \tag{2.23}$$

with the respective dielectric constants of each layer ϵ_{si} and the partial filling factors

$$q_i = \frac{K(k_i)}{K(k_i')}\left(\frac{K(k_4)}{K(k_4')} + \frac{K(k_5)}{K(k_5')}\right)^{-1}. \quad i = 1,2,3 \tag{2.24}$$

Furthermore, the impedance of the coplanar waveguide can be expressed with the phase velocity $v_{ph} = c/\sqrt{\epsilon_{eff}}$ as [46]

$$Z_0 = \frac{1}{C_{CPW}v_{ph}} = \frac{1}{cC_{air}\sqrt{\epsilon_{eff}}} \tag{2.25}$$

$$= \frac{60\pi}{\sqrt{\epsilon_{eff}}}\left(\frac{K(k_4)}{K(k_4')} + \frac{K(k_5)}{K(k_5')}\right)^{-1}. \tag{2.26}$$

The impedance of a coplanar waveguide can be set by adjusting the geometry parameters. Due to the fact that h and ϵ_s of a dielectric substrate are normally fixed, this can be done by changing S and W or in general terms changing the ratio of S/W.

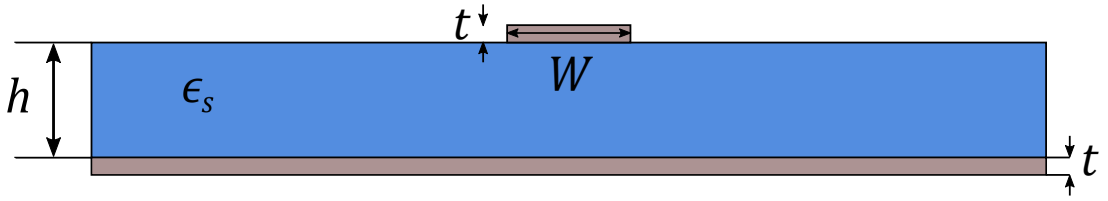

Fig. 2.4.: Cross-section of a microstrip structure. On top of a grounded dielectric substrate is the strip planted.

2.2.2. Microstrip resonators

Besides the coplanar waveguide, the microstrip is a popular and widely used planar transmission line [47, 48]. This is due to the comparably simple fabrication process and the good integration in other microwave circuits [44]. In figure 2.4 a simple cross-section is shown. On top of a grounded dielectric substrate with a certain height h a conductor with thickness t and width W is applied. Typically, the thickness of the ground plane below the dielectric equals to t of the strip. The open structure of the microstrip makes it convenient to use, but causes some complications, namely the non-TEM mode propagating. However, a pure TEM for the quasi-static analysis is assumed [43]. As for the coplanar waveguide, the impedance and effective dielectric constant need to be formulated.
There are different expressions for the characteristic impedance Z_0, namely by Wheeler, Schneider or Hammerstad and Jensen [47, 49–51]. The form of Wheeler is sufficient within this work. For narrow strips ($W/h \leq 3.3$) and alumina-type substrates $8 \leq \epsilon_s \leq 12$ the impedance is given as [50]

$$Z_0 = \frac{\eta_0}{\pi\sqrt{2(\epsilon_s+1)}} \cdot \left(\ln\left(\frac{4h}{W} + \sqrt{\left(\frac{4h}{W}\right)^2 + 2} \right) - \frac{1}{2}\frac{\epsilon_s - 1}{\epsilon_s + 1}\left(\ln\frac{\pi}{2} + \frac{1}{\epsilon_s}\ln\frac{4}{\pi} \right) \right) , \tag{2.27}$$

with η_0 the impedance of free space. Here the characteristic impedance can be changed by adjusting W of the strip.
For the effective dielectric constant ϵ_{eff} of a microstrip exist different formulas as well [47, 51–53]. Here, the approximate function of Schneider is meant to have an accuracy of 2 % and holds [47]

$$\epsilon_{\text{eff}} = \frac{\epsilon_s + 1}{2} + \frac{\epsilon_s - 1}{2} \cdot \frac{1}{\sqrt{1 + 10\frac{h}{W}}} . \tag{2.28}$$

The effective dielectric constant takes into account that most of the electric field is contained in the dielectric, but a part of the total energy exists in the air above the structure.

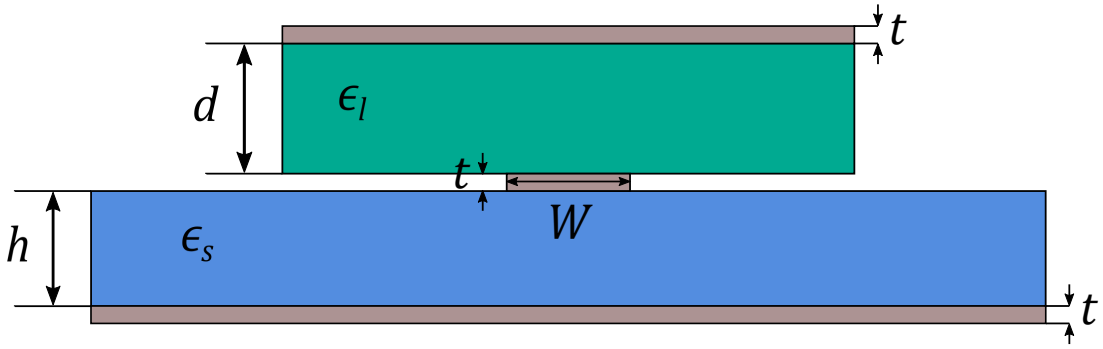

Fig. 2.5.: Cross-section of a microstrip structure with sample placed on top. The sample needs to be grounded for the electric field to penetrate it.

The microstrip can be used in microwave spectroscopy by creating a resonator. Due to the design of the microstrip it is possible to build a $\lambda/2$-resonator by adding gaps in the strip on the top surface of the dielectric. The physics are then applicable from the coplanar waveguide above mentioned. A standing wave forms if the resonance condition (2.9) is satisfied and hence the transmission increases. Again, the excitation can be modeled by a Lorentzian function as in (2.11). Furthermore, the quality factor can be calculated with equation (2.12).
If an unknown dielectric sample with height d and ϵ_l is under study, it can be easily placed on the strip between the resonator gaps. To make a statement about the dielectric properties, the electric field must penetrate the sample. Since most of the electric field is stored in the dielectric substrate, there needs to be a slight adjustment in the structure. The placed sample of interest has to be grounded as well, leading to a composition reminding of a stripline. This enables the electric field to propagate through the sample. In figure 2.5 the so-called embedded transmission line (ETL) is visualized.
For this setup the effective dielectric constant needs to be recalculated and the following expression is obtained [54]

$$\epsilon_\mathrm{eff} = \left(\frac{\epsilon_\mathrm{s} + \epsilon_\mathrm{l}}{2}\right) \cdot \frac{U(K(\epsilon_\mathrm{s}, \epsilon_\mathrm{l}))}{U(K(1,1))}\,, \tag{2.29}$$

with

$$U(x) = 1.15 - \ln(x) + 0.08x^2 \tag{2.30}$$

$$K(\epsilon_\mathrm{s}, \epsilon_\mathrm{l}) = \frac{1}{\epsilon_\mathrm{s} + \epsilon_\mathrm{l}} \cdot \left(\frac{\epsilon_\mathrm{s}}{\left(\frac{2h}{W}\right)} + \frac{\epsilon_\mathrm{l}}{\left(\frac{2d}{W}\right)}\right)\,. \tag{2.31}$$

3. High frequency dielectric measurements

A dielectric material is electrically insulting and by applying an external electric field so-called dielectric polarization occurs, which can be measured by the complex-valued permittivity. In dielectric spectroscopy this generally temperature- and frequency-dependent parameter is studied for the specimen under test for different electric and magnetic field orientations, frequencies and temperatures. By understanding the dielectric properties it is possible to determine the use of dielectrics for many applications.
This chapter firstly introduces the permittivity, defines dielectric losses and highlights the important role for dielectric measurements. Subsequently, an overview of the possible measurement methods is presented, including general information, as well as advantages and disadvantages. After that, one of those methods, the resonant techniques are examined. Following this, microwave waveguide resonators are discussed for the use in dielectric spectroscopy and their advantage compared to the other presented resonant techniques. This chapter closes out with an insight to one of the major error source in dielectric measurements and a short strategy presented within this work.

3.1. Permittivity and dielectric losses

Permittivity is obtained by Maxwell's equations introduced in chapter 2.1. It describes the interaction of the external electric field with the electric dipole moment of the sample. Permittvity is a macroscopic parameter since it averages over a certain volume of dipoles. The quantities depend on the orientation of the field relative to the dipole orientation, therefore this anisotropy is characterized by describing the permittivity as a tensor.
Permittivity expresses macroscopically the polarizability of the material, the electronic polarization in atoms when an external field is applied. As a consequence of the external field, atoms and defects readjust dynamically their position which is called relaxation. The dielectric response strongly depends on the material phase, degree of crystallinity and existence and mobility of dipoles and defects [14]. Besides, for different frequency regions the mechanisms of polarization changes. The dipolar polarizability arises from a permanent electric dipole moment that can change orientation in an applied electric field [55]. This mechanism occurs strongly at microwave frequencies. For higher frequencies the electronic contribution of the total polarizability takes over. In general terms, the dielectric response of the material lags behind the electric field for high frequencies which causes losses.
To count for these losses, the macroscopic measured permittivity needs to be defined complex. The real part of the complex permittivity, the so-called dielectric constant ϵ_1 is a measure of

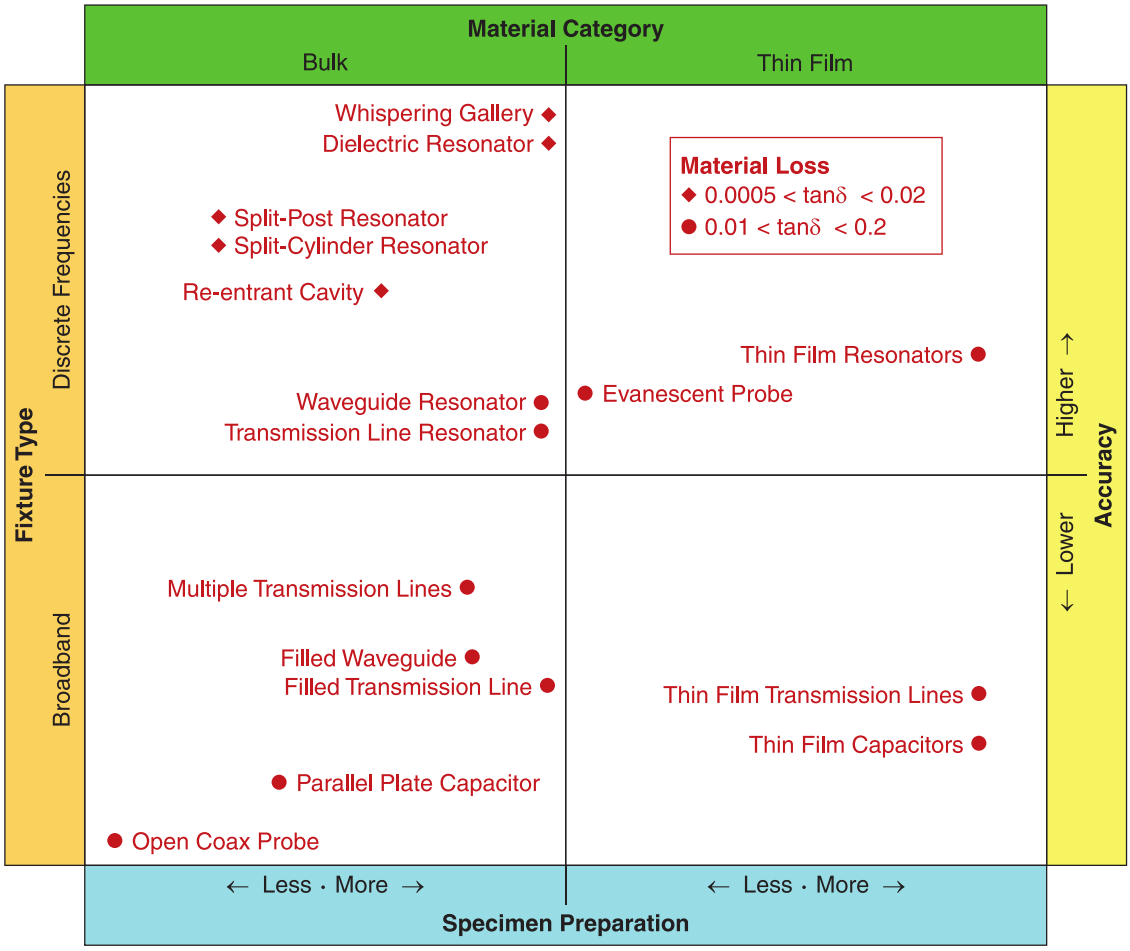

Fig. 3.1.: Dielectric measurement methods grouped according to material category / sample preparation and frequency band / relative accuracy [14].

the stored energy in the material. The imaginary part ϵ_2 is a measure of the absorption in the material [56]. The ratio of imaginary to real part of the complex permittivity is called loss tangent

$$\tan\delta = \frac{\epsilon_2}{\epsilon_1}, \tag{3.1}$$

and is a measure of losses in the material. In the microwave regime, the permittivity of low-loss materials generally slowly decreases as function of frequency, whereas the loss tangent slowly increases [14].

3.2. Overview of measurements methods

When investigating a material for its dielectric properties, spatial dimensions and geometry of the sample are the first important criteria to select a convenient technique. Here the main categories are bulk or thin. Bulk materials are of macroscopic dimensions, while thin

materials are on sub-micrometer scale in one dimension, including thin films.
For each category a couple of different methods have been developed, with each having adanvtages and disadvantages depending on the aim of the measurement. In figure 3.1 different measurement methods are displayed, classified by frequency band versus material category. All shown methods can be summarized in four supercategories [10]: Transmission and reflection line techniques, free-space methods, open-ended coaxial-probe techniques, and resonant techniques. However, there are some hybrid techniques [57].
For dielectric measurements at high frequencies, especially in the microwave regime, a vector network analyzer (VNA) needs to be connected to the sample under study through a test fixture, such as probe or transmission line [14].

3.2.1. Transmission / reflection line method

The transmission and reflection line method is a widely used broadband measurement technique, where only the fundamental mode is assumed to propagate [11, 15]. To measure a dielectric sample it simply must be placed inside the transmission line and the propagating wave needs to be directed at the sample. With the help of a VNA the complex scattering parameters of both ports are measured. For the transmission line method the transmitted signal (S_{21}, S_{12}) is of importance whereas for the reflection line method it is the reflected signal (S_{11}, S_{22}). The scattering parameters are directly connected to the complex permittivity by a set of equations which can be analytically solved [11]. For both methods a sample preparation is needed to fit the sample exactly in the structure. The accuracy of the measurement depends on the electric field inside the sample. For transmission and reflection line methods calibrations before the actual measurements are needed [15].
Advantages are the determination of permittivity and permeability at the same time. Disadvantages are the limitation of accuracy by air gap effects and penetration of the field in the sample, a difficult fabricaton process for single crystals and high frequencies, and limited frequencies only up to 10 GHz due to parasitic losses [56].

3.2.2. Free-space method

The free-space method is suited for broad frequency ranges and for materials which need to be unmodified for measurements. This non-destructive technique can be used for example for materials such as vegetables or soils and allows measurements at high temperatures or in hostile environments [12]. It requires the sample to be large and flat and usually there is a pair of spot-focusing horn lens antennas facing each other, which are connected via coaxial cables to a VNA. Since the method is operating in open space, possible inaccurate results can be obtained. Before the actual measurement a calibration is needed: There are different possible approaches, such as the line-reflect-line (LRL), the through-reflect-match (TRM) or the trough-reflect-line (TRL) [58, 59]. After calibrating the empty sample holder, as well as with the sample placed onto it, the S-parameters for reflection and transmission coefficients are obtained within the measurement. The dielectric properties then can be determined by post processing the measured data. Time-Domain gating is implemented to filter the signal for multiple reflections in the sample, just as diffraction of energy from the antennas [60].

Advantages are the broad measurable frequency range, no need of surface modification or separate enclosure of the sample and the determination of electric and magnetic properties at the same time. Disadvantages are the required specific shape of the sample, multiple reflections between sample and antennas and diffraction effects [56].

3.2.3. Open-ended coaxial-probe method

In this technique a coaxial probe is terminated with the sample under study [61]. It is possible to cover a broad frequency range and a wide range of temperatures. This non-destructive method is suited for a variety of solids and liquids, including biological specimens which need in-vivo measurements [13]. The electromagnetic fields at the probe end penetrates into the sample and the reflected signal can be directly measured. This method requires a calibration, where an open end, closed end, and a loaded end need to be measured for the complex reflection coefficient. When the probe is in contact with the sample it has a certain admittance $Y_{\mathrm{L}}(f, \epsilon)$, which depends on the internal admittance of the coaxial line and more importantly the external admittance depending on frequency and dielectric constant of the examined sample. With an iterative process the value of the dielectric constant can be found [62]. However, there are limitations in the model for the calculation, since Y_{L} is a relatively complicated function of frequency, permittivity and physical characteristics of the sample [63].
Advantages are the easy sample preparation and the relatively short measuring time for a number of samples after calibration. Disadvantages are, that only reflection measurements are possible and air gaps between sample and probe can affect the measurements [56].
Additionally, the broadband open-ended coaxial-probe method can be used in microwave spectroscopy for conductive materials with the so-called Corbino geometry [64, 65].

3.3. Resonant techniques

Resonant measurements are the most precise methods to determine dielectric properties [14]. However, this comes with some limitations: Usually the resonant means work only at single frequencies and are suitable for low-loss materials. Generally, the measurement is done in one of two ways: Either is the resonant measurement performed on the sample itself or the cavity perturbation technique is used [56]. The first approach holds for larger samples but only with very low losses, while the second one is suitable for permittivity measurements with samples at any size and shape with medium to high losses. Resonant techniques provide the better accuracy compared to broadband methods, however, the sample preparation is of utmost importance to make them suitable for cavities [66]. With the resonance characteristics depending on the sample, resonance frequency and quality factor determine the dielectric properties. For that the S-parameters are measured, while a calibration is not needed for resonant techniques. The accuracy of the measurement of the dielectric constant generally is limited by the presence of air gaps between the sample and the conducting parts of the resonant structure, by computational inaccuracies and by uncertainties in the physical dimensions of sample and resonant structure [67]. In the following, three resonant structures

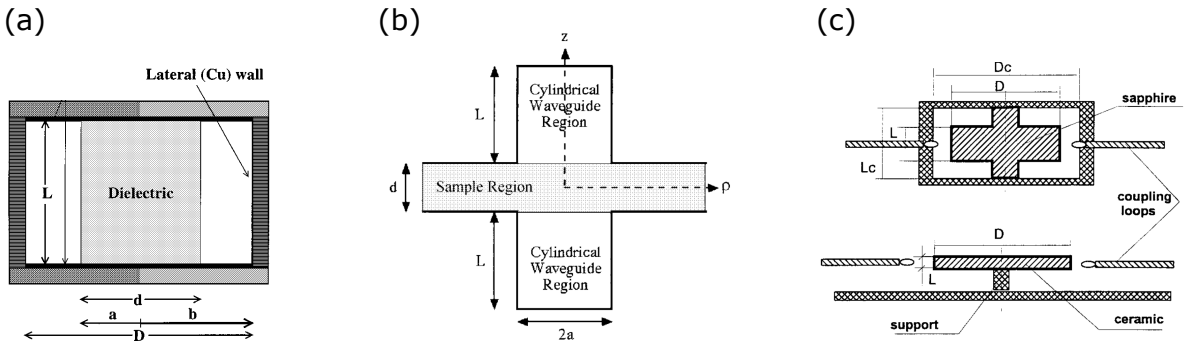

Fig. 3.2.: Schematic cross-sectional views of (a) a dielectric resonator [16] (b) a split-cylinder resonator [66] (c) two whispering-gallery mode resonant structures [67].

are examined, the dielectric resonator, the split-cylinder resonator and the whispering-gallery mode resonator.

3.3.1. Dielectric resonator

For the dielectric resonator method [16, 68] the cavity is directly designed for the dielectric sample under study as depicted in figure 3.2(a). The sample must be in cylindrical shape and is enclosed in a copper cylindrical cavity between two metallic shields. The loss of the system consists of the dielectric loss and by entirely enclosing the dielectric in the cavity parasitic losses are eliminated. Further reduction of losses is possible by applying superconductors as shields. The diameter of the dielectric sample needs to be large for this method to ensure a large volume of the cavity filled by the dielectric.
The TE_{011} mode is employed within this technique due to the symmetry of the system but is only valid for isotropic samples. By measuring the S-parameters of the system, resonance frequency and unloaded quality factor can be obtained. The real part of the relative permittivity is then calculated from the resonance frequency utilizing transcendental equations depending on the symmetry of the system [68]. The loss tangent is directly calculated from the quality factor with some correction for the surface resistance of the cavity. It is possible to measure the sample over a wide temperature range with the dielectric resonator. However, the accuracy of the dielectric constant and loss tangent depends mostly on the accuracy of the resonance frequency measurements and quality factor measurements, respectively. Furthermore, the accuracy of the geometric dimensions defines the accuracy of the results.

3.3.2. Split-cylinder resonator

The split-cylinder resonator technique [17, 66] uses a cylindrical cavity, cut in two halves with the sample placed in between, as shown in 3.2(b). The dielectric under study is required to be flat and larger than the diameter of the two cavity sections. A full-wave analysis of the split cylinder resonator must be applied to derive the resonance condition. In the model it is assumed that the fields are confined in the sample and the cylindrical cavities. A TE_{011} mode

is excited but evanescent TE_{0n} modes in the cavity regions must be included to consider for boundary conditions. For the full analysis see [66].
With the help of a VNA the resonance curve can be measured with obtaining resonance frequency and quality factor. With all important parameters (sample length, cavity diameter and length, resonance frequency) known, the dielectric constant of the sample can be iteratively calculated. For this an initial guess is needed, which should not deviate more than 50 % from the sample permittivity. The loss tangent of the sample is obtained by taking the inverse of the measured quality factor.
The results obtained with the split-cylinder method show very good accuracy and the method is applicable for different temperatures. However, this technique is limited due to the specific requirements regarding the sample size and shape as well as the elaborate calculation of the dielectric constant.

3.3.3. Whispering-gallery mode resonator

The whispering-gallery mode resonator [18, 67, 69] is a special case of the dielectric resonator as depicted in figure 3.2(c) and enables the most accurate dielectric measurements. This technique requires large dielectric samples of cylindrical shape. In such specimens higher order azimuthal modes, so-called whispering-gallery modes are utilized, which decrease radiation losses rapidly, especially for higher mode numbers.
This technique makes use of the mode-matching method, where a resonant structure is subdivided into cylindrical regions and the resonant frequencies are the solution to a system of matrix equations. The measurement procedure for determining the real permittivity is as follows [67]: 1) The resonant frequencies for several whispering-gallery mode families of the structure are computed based on initial values. 2) The resonance frequency spectrum is measured and the fundamental mode identified. 3) Permittivity is computed from the measured resonant frequency. 4) The resonant frequency is computed (step 1) with the derived permittivity and compared.
The whispering-gallery mode technique is perfectly suited for measuring low-loss dielectrics, with the sample requested to be isotropic or uniaxially anisotropic. It provides best accuracy and can be used over a broad temperature range. But it is difficult to identify the correct resonant modes. This identification is based on computations with initial assumed dielectric constants, requiring knowledge of the dielectric under study.

3.4. Microwave waveguide resonators

In this section another specific resonant technique is under review: Microwave waveguide resonators. Whereas the theoretical principles of several waveguides are discussed in detail in chapter 2.2, this part focuses on advantages of waveguide resonators for dielectric measurements.
The before discussed resonant techniques have one thing in common: each approach implements the resonant technique directly on the sample under study which makes them only operable at a single frequency. This discrete frequency can be located according to sample

and cavity anywhere in the microwave regime but gives only access to a limited frequency. Here one advantage of waveguide resonators comes into play: Not only the fundamental mode is accessible and can be used for dielectric measurements but also several higher modes can be excited. This then gives the possibility to probe several discrete frequencies in a broad microwave range. Another benefit of waveguide resonators is the option to operate different techniques. Like the examples before, waveguide resonators can be implemented on the dielectric sample as well but moreover they can be utilized in the cavity perturbation technique [19, 70]. Here, the sample fills the resonant waveguide and with the resulting change in resonance frequency and quality factor the complex dielectric properties can be determined. This shift depends on the geometrical dimensions of the sample just as on the used resonant cavity. With the cavity perturbation technique bulk samples and thin films can be measured for their properties using waveguide resonators [25]. For this purpose, the bulk sample does not need to be in a specific shape or size, compared to the resonant techniques above. It has the restriction that is should fit inside the cavity and contact surfaces should be polished, leading to a comparably slight sample preparation.
Besides the mentioned advantages, waveguide resonators have a relatively easy fabrication process and measurement procedure, they can be used in a wide temperature range down to cryogenic temperatures and in principle it is possible to study anisotropy as well as medium to high loss dielectric samples. All this combined makes microwave waveguide resonators a promising candidate for measuring bulk dielectrics.

3.5. Source of error: Air gaps

For all resonant techniques the presence of air gaps between sample and conductive parts is a major error source which limits the measurement accuracy. This large systematic uncertainty is caused by air gaps introducing a series capacitance that results in a severe bias in the calculated permittivity [14]. The capacitance of the air gaps is a non-linear function of the complex permittivity of the sample, and the uncertainties increase with increasing real part of the permittivity [71]. With knowledge of the space between sample and conductive parts, this systematic error can be reduced, however, precise determination of the gap size is difficult. The air space causes discontinuity across the sample boundary. The measurement system such as waveguide resonators have a normal component of the electric field which penetrates into the dielectric sample. With an additional gap between conductor and sample, there is a discontinuity in the normal component leading to depolarization effects which cause this large error [67]. If the field is continuous across the boundary, e.g. for resonant techniques shaped on the dielectric sample, air gaps do not play a significant role. If air gaps cannot be prevented, they may be corrected within theoretical models, however, the formulas generally undercorrect for the real part, while overcorrecting the imaginary part of the permittivity [11].

3.6. Strategy of this work

The goal of this work is to precisely determine the dielectric properties of bulk dielectrics in the microwave regime up to 20 GHz. With the help of resonant measurements by utilizing planar microwave resonators several discrete frequencies can be probed. The possibility to access higher harmonics and thereby maintaining good accuracy is an advantage compared to other resonant techniques. The acquired knowledge of preliminary studies on thin films [25] is used and expanded within this project. This strategy requires solutions to overcome challenges which occur by going from thin films to bulk materials. For example, the penetration of the electric field in the sample under study differs for these different spatial dimensions. Simulations are utilized to assess possible approaches for their suitability before testing them in the experiment.
The before introduced cavity perturbation theory is a subject within this project. If a dielectric sample is placed on top of a CPW resonator, the characteristics change, which can be analyzed for the desired properties. Whereas this approach can be applied for thin films, this work clarifies the functionality for bulk samples. Furthermore, this project discusses another technique where the resonant structure is fabricated on the material under study. Here other occurring challenges are reviewed such as coupling or performance. With all different methods investigated and discussed, this work establishes a new measurement approach. Results are presented regarding the accessible frequency and temperature range and the feasible thickness of potential bulk dielectric samples.

4. From simulation to experiment

This chapter introduces microwave simulations and why it is convenient to use them associated to experiments. In the first part the basic concepts including the finite integration technique are presented. Secondly, the experimental fundamentals are shortly depicted, with the used setups and materials implied as well as a short insight in the measuring procedure. As a last point the consistency of the before established theory, simulation and experiment is shown.

4.1. Fundamental concepts of microwave simulations

Simulations are a suitable tool to model physical principles and play a major role in different fields of research [25, 72]. Not only to demonstrate the physics but also to assess the utility of models and approaches. Simulations are used when complex problems are not analytically solvable. Instead, by approaching numerical attempts, the whole complex problem is divided into a number of sub-problems. Every element is then treated by its own, leading to equations for the wanted quantity. By approximating and putting them in broad agreement to the original problem, the local parts can be recombined. With boundary conditions and initial values can the set of local equations be solved numerically giving a well-approximated solution of the whole complex problem [73].

The numerical approach discussed is the so called finite integration technique (FIT) [74]. Maxwell's equations (2.1) - (2.4) need to be solved for every electrodynamic problem. The FIT reformulates these in their integral form to simulate problems with complex geometries. The basis of this technique is the introduction of a grid of sub-elements [75]. The electromagnetic field problem is divided in a finite number of tetra- or hexagonal volume cells, with the condition that all elements fit perfectly to each other. For each cell the electric voltages on the edges and the magnetic facet fluxes through the surfaces are addressed. In a second grid of cells the dielectric fluxes of the surfaces and the magnetic grid voltages of each cells are treated. The resulting equations are a discrete representation of Maxwell's equations on both grids and can be put in relation via matrix operators. In the sub-elements the electromagnetic quantities are solved exactly. Here the approximation of the FIT comes into play: The quantities of the cells cannot be transferred completely without extrapolation. The size of the meshing structure therefore is of importance. The advantage of the FIT is the form of the cells leading to a precise modeling of the complex geometry [75].

The commercially available software *CST Microwave Studio* has been used for the desired simulations in this project [76]. It makes use of the finite integration technique introduced above. The CAD environment allows the construction of structures with advanced geometry

and the possibility to adjust parameters automatically. As a consequence, the structures can be simulated sequentially with the change of the wanted parameter. The frequency domain solver is used due to its suitability for resonator simulations [77]. Besides the electromagnetic field distribution the solver delivers the microwave S-parameters. As mentioned above, the mesh can be created with different types of cells, here the tetrahedral volum meshing is used for the better approximation of curved elements. The accuracy of the simulation strongly depends on the mesh because of the extrapolation between cells. A finer mesh leads to more accurate solution, but needs a larger amount of computational time [78].
CST Microwave Studio gives the possibility to an automatic refinement of the mesh. The mesh is refined where a larger number of cells is requested. However, this automatic process of refinement takes a lot of time and resources and it is possible that the results of a simulation run can be distorted due to the refinement due to the updating of the mesh. The automatic refinement therefore is turned off. To ensure accurate results anyway, the mesh is adjusted manually introducing finer areas for important components of the structure and otherwise making the mesh coarse. For each model a manually refined mesh is found, making a compromise between computational time and the accuracy of the desired results, especially resonance frequency and quality factor of a resonator.

4.2. Experimental basics

4.2.1. Setups

Bath cryostat and VTI

For all microwave measurements a liquid helium bath cryostat was used, schematically depicted in figure 4.1 with a liquid helium bath inside an insulating vacuum. Inside a various temperature inset (VTI) the sample chamber is placed with all measurement and control cables. To reach temperatures below the boiling point of liquid helium, the needle valve needs to be opened slightly to let liquid helium flow into the sample chamber. By pumping the VTI and lowering the pressure, temperatures from 1.4 K to 300 K can be reached. For a stable temperature level the heater works simultaneously against the helium flow with the sensor giving the actual temperature of the sample chamber. The microwave chip inside the box is via microwave coaxial cables connected to the ports of a vector network analyzer (VNA). A manual for the setup can be found in [79, 80].

SQUID

In the SQUID (superconducting quantum interference device) superconducting samples have been characterized for their critical temperature. To do so, the sample is placed insight a small sample holder and then put inside an superconducting loop. At different temperatures and a constant magnetic field the sample is moved in and out of the loop, leading to a change in the magnetic flux. The magnetization of the sample as function of temperature can be measured and with this the critical temperature can be obtained. In the appendix an

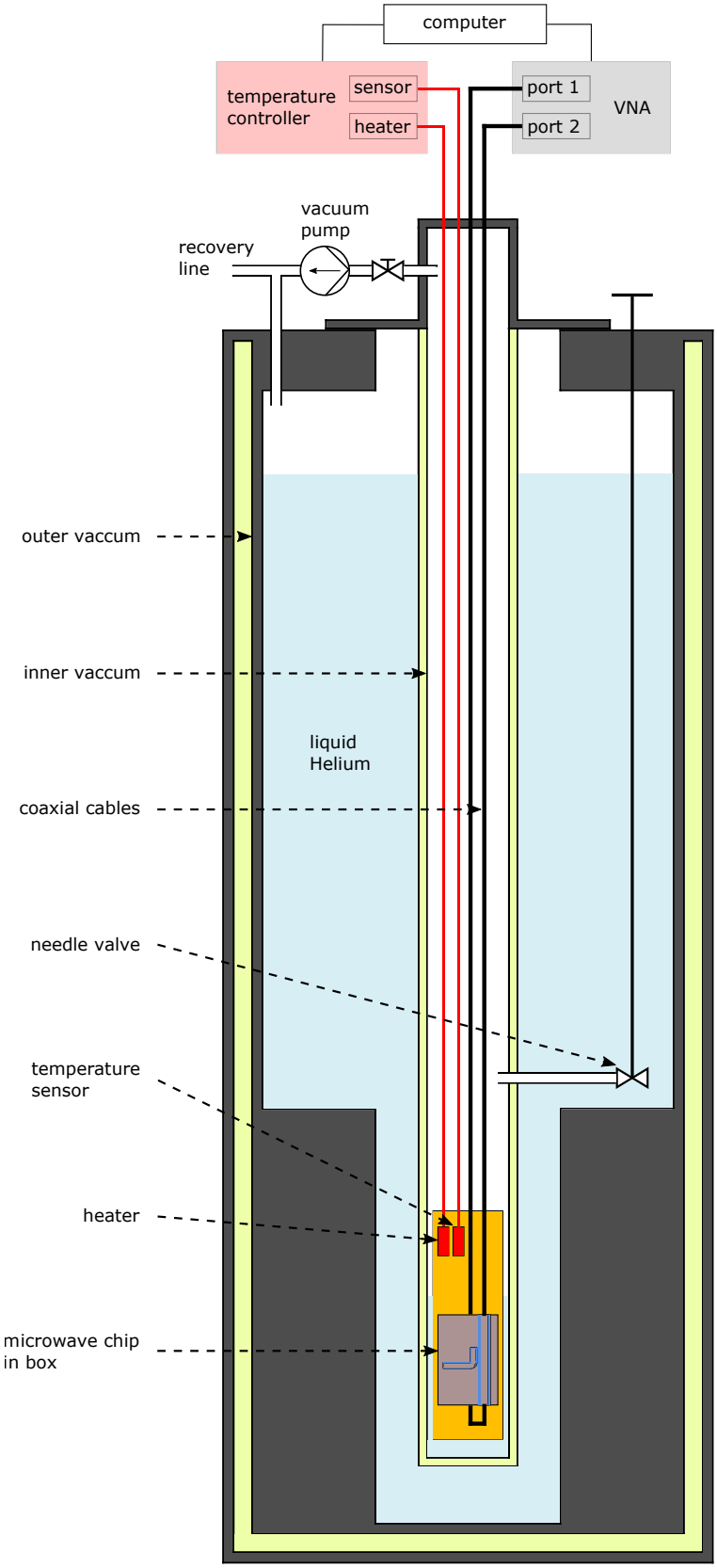

Fig. 4.1.: Schematic view of the bath cryostat. Including the variable temperature insert (VTI), microwave chip, vacuum pump and control and measurement devices.

exemplary measurement is displayed. For a detailed operation manual of the SQUID see [81, 82].

4.2.2. Materials

Sapphire (Al_2O_3)

Al_2O_3 is a material with very low dielectric losses making it a perfectly fitting substrate for microwave resonators. The dielectric constant ϵ_1 depends on the orientation of the optical c-axis and ranges from 9.3 to about 11.5 for a broad frequency range [69, 83, 84]. Changes in ϵ_1 are very small in the frequency range of this project and can therefore be neglected. Additionally, temperature-dependent changes in ϵ_1 are negligible, ensuring a constant value in temperature and frequency for this project [84].

Magnesium oxide (MgO) and lanthanum aluminate ($LaAlO_3$ or LAO)

Both, MgO and LAO, are low-loss dielectric materials with isotropic dielectric constants ϵ_1. In the frequency and temperature ranges of this project, MgO as well as LAO show no or only slight changes in ϵ_1 [84]. For MgO ϵ_1 is around 10, whereas it is around 24 for LAO [83, 84].

Rutile (TiO_2)

Like the materials above, TiO_2 is a low-less material but with a comparably high dielectric constant ϵ_1. It is anisotropic and depends on the orientation of the optical c-axis and ranges from 131 to 256 for microwave frequencies at low temperatures [85]. In the frequency range examined in this project ϵ_1 is frequency-independent. For higher temperatures up to room temperature, ϵ_1 decreases, but below 10 K it shows only slight changes making it constant in this temperature range [86].

Copper (Cu), niobium (Nb) and lead (Pb)

As pointed out in Section 2.2, there is a conductive layer needed on top of the dielectric substrate to create planar microwave resonator.
One material for this purpose is copper: With its high electrical conductivity it is well-suited for temperature ranges from room temperature to low temperatures.
The other material deposited on the dielectric is the superconductor Nb, which is a perfect electrical dc conductor below its literature critical temperature of about 9.2 K [55]. The experimental critical temperature strongly depends on the surface and material of the underlying dielectric and is related to the quality of the film.
For the microstrip measurements, the conductive material being used is Pb. It has a relatively simple handling and is also superconducting at cryogenic temperatures below 7.2 K [21, 87, 88].

4.2.3. Measuring and fitting procedure

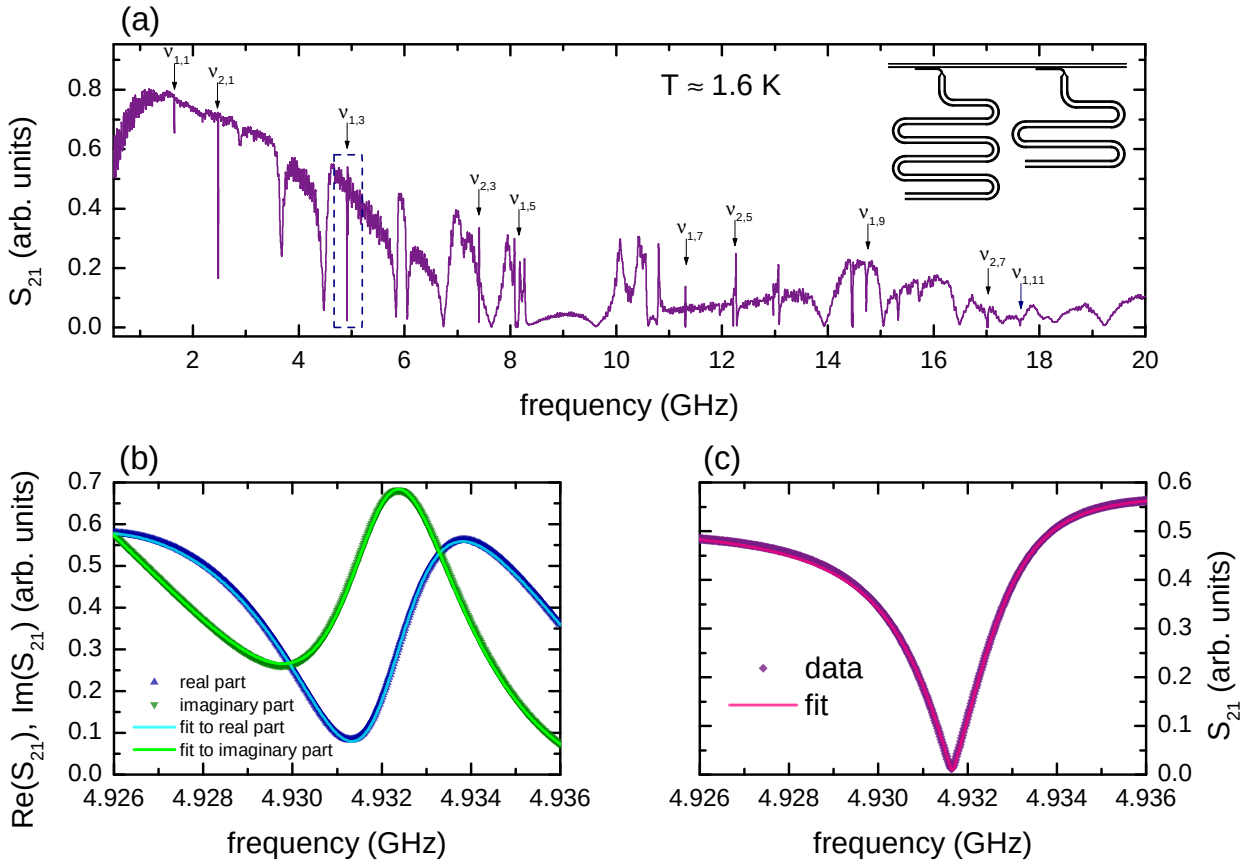

Fig. 4.2.: (a) Transmission spectrum of two resonators up to 20 GHz. Arrows indicate resonances and the surrounded resonance is shown in detail. The inset shows both measured resonators. (b) Complex transmission spectrum of the highlighted resonance around 4.932 GHz with corresponding fits to real and imaginary part. (c) Absolute transmission spectrum of the same resonance with the corresponding fit.

For the data acquisition the resonator chip is placed inside a box with microwave connectors. The box is then put inside the sample chamber inside the VTI and connected to VNA via coaxial cables as depicted in figure 4.1. The VNA covers a wide frequency range from 50 MHz to 20 GHz and is thus perfectly suited for microwave spectroscopy. It gives direct access to the microwave S-parameters, with the transmission coefficient S_{21} being of major interest. The transmission spectrum of the microwave resonator is obtained, with an example shown in figure 4.2(a) up to 20 GHz. S_{21} decreases with increasing frequencies originating from the damping of the signal in the coaxial cables. The exemplary spectrum is due to a pair of $\lambda/4$-resonators (shown in the inset) with a shared feedline on a Al_2O_3 substrate only differing in the length of the resonator. The excitation of both resonators manifest as sharp absorption dips in the spectrum. Here, the resonances are marked with $\nu_{j,n}$ and highlighted with arrows, with j displaying the different resonators and n being the harmonic frequencies. Note, that

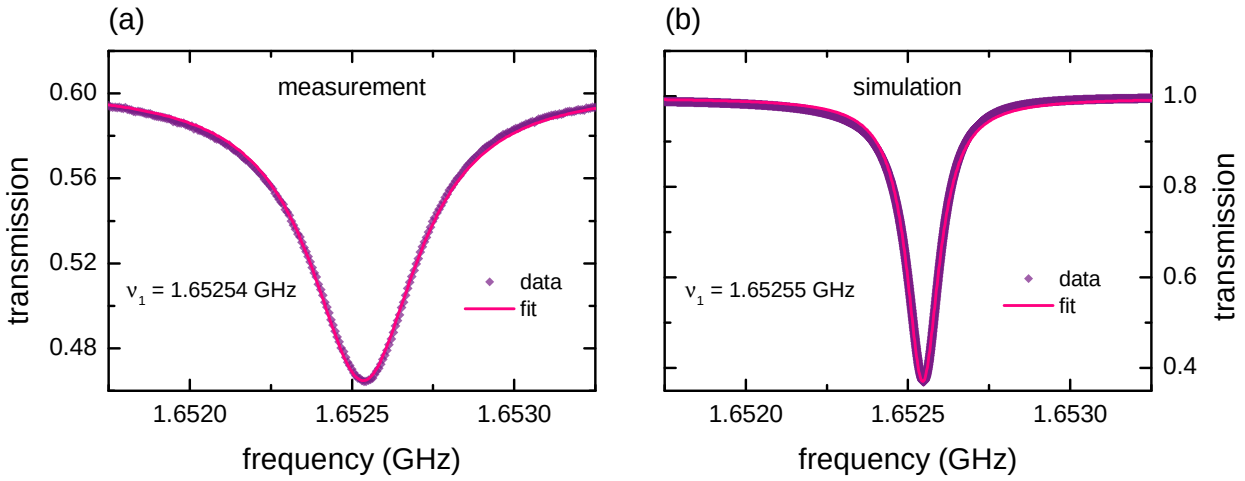

Fig. 4.3.: (a) Transmission spectrum of the measured coplanar Nb resonator on a Al_2O_3 substrate at a temperature of 1.6 K. (b) Transmission spectrum of the simulated likeness on a substrate with $\epsilon_s = 10.07$.

only odd multiples exist for a $\lambda/4$-resonators (see equation (2.10)).
For the further procedure, the different resonances have been picked and measured individually. To analyze the resonances and to obtain resonance frequency and quality factor, Lorentzian fits (see equation (2.11)) have been performed. Since in microwave spectroscopy unwanted reflections in the cables occur and interfere with the actual measuring signal, a complex Lorentzian model is fitted to the data. In figure 4.2(b) the complex spectrum of S_{21} for a selected resonance is depicted with the according fits to real and imaginary part of the signal. Thus, the data can be fitted adequately, which can be seen in figure 4.2(c) with the absolute spectrum and the appropriate fit. A detailed depiction of the fittig procedure can be found in [89].

4.3. Consistency between theory, simulation and experiment

In this part the reliability of the simulation is under review. For this, an exemplary resonator is measured and additionally created within the simulations. The simulated and experimental results are then compared with the theoretical predictions, which were introduced in Section 2.2. This needs to be accomplished for the CPW and the microstrip separately.

4.3.1. Coplanar waveguide

A $\lambda/4$-resonator out of Nb with meander structure and a total length of $l = 19\,435\,\mu m$ on a Al_2O_3 substrate with height $h_s = 430\,\mu m$ is designed. The ratio of of S/W of the feedline as well as the resonator is found in a way to match it to the impedance of $50\,\Omega$ of the microwave cables. To do so, equation (2.26) is used. The measurement is performed at a temperature

of 1.6 K, where the Nb layer is superconducting. In figure 4.3(a) the transmission spectrum ($T_\nu = S_{21}^2$) is shown with a Lorentzian fit perfectly describing the line shape of the data. The fundamental resonance frequency is found to be $\nu_1 = 1.652\,54\,\mathrm{GHz}$.
Subsequently, an exact model of the measured resonator is created within the simulations with all geometrical properties adopted. The low losses of the Al_2O_3 are taken into account within the simulations, whereas a perfectly conducting material was assumed for the superconductor. Simulations were then performed in a range of $9.3 \leq \epsilon_\mathrm{s} \leq 11.5$ for the dielectric constant of the substrate. In figure 4.3(b) the transmission spectrum is depicted with a Lorentzian fit with fundamental resonance frequency at $\nu_1 = 1.652\,55\,\mathrm{GHz}$.
The resonance frequencies for the measured and simulated results are almost identical for $\epsilon_\mathrm{s} = 10.07$ of the simulated substrate. The dielectric constant of Al_2O_3 is expected to have a value of $\epsilon_1 \approx 10$, since it is cut in r-plane and the meander structure causes a mean value of the anisotropic dielectric constant. The minor deviation of the simulated result is justified within the experimental errors. The experimental and simulated resonance frequency are now checked against the value which one would theoretically expect. All geometrical parameters are considered in the prediction by the conformal mapping method:

$$\nu_1^\mathrm{theo} = 1.655\,51\,\mathrm{GHz} \tag{4.1}$$
$$\nu_1^\mathrm{sim} = 1.652\,55\,\mathrm{GHz} \tag{4.2}$$
$$\nu_1^\mathrm{exp} = 1.652\,54\,\mathrm{GHz}\,. \tag{4.3}$$

The theoretical prediction deviates less than 0.2 % from the experimental and simulated result which ensures the consistency between theory, simulation and experiment.

4.3.2. Microstrip

The same procedure needs to be done for a microstrip resonator. A $\lambda/2$-resonator with a total length of $l = 7700\,\mu\mathrm{m}$ on a Al_2O_3 substrate with height $h_\mathrm{s} = 430\,\mu\mathrm{m}$ is designed. According to equation (2.27) the width of the strip is found to match the impedance of the microwave coaxial cables. In figure 4.4(a) the transmission spectrum of the measurement performed at 1.5 K with a Lorentzian fit to the data is shown. Note, that for a $\lambda/2$-resonator resonances appear as peaks in the spectrum. The fundamental resonance frequency is found to be $\nu_1 = 7.325\,37\,\mathrm{GHz}$.
Afterwards, the microstrip resonator is exactly modeled and simulated for a sweep of the dielectric constant of the substrate. In figure 4.4(b) the resulting transmission spectrum is displayed with fundamental resonance frequency at $\nu_1 = 7.326\,13\,\mathrm{GHz}$. The result of experiment and simulation match for $\epsilon_\mathrm{s} = 10.05$ of the simulated substrate, which is highly reasonable within the experimental error.

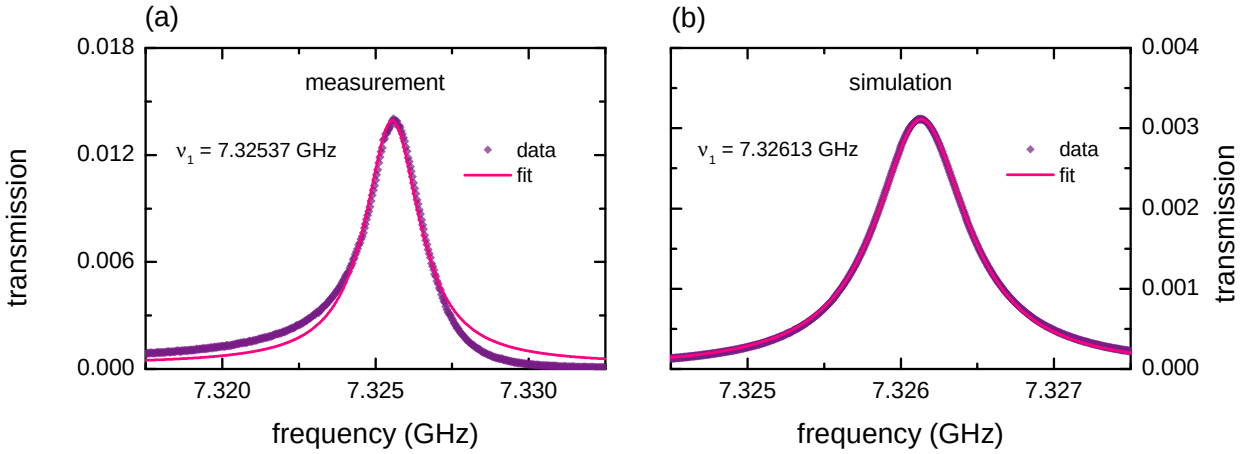

Fig. 4.4.: (a) Transmission spectrum of the measured microstrip Nb resonator on a Al_2O_3 substrate at a temperature of 1.6 K. (b) Transmission spectrum of the simulated likeness on a substrate with $\epsilon s = 10.05$.

To compare now the simulated and experimental results with the theory, the effective dielectric constant (see equation (2.28)) and with it the resonance frequency can be calculated:

$$\nu_1^{\text{theo}} = 7.545\,44\,\text{GHz} \tag{4.4}$$
$$\nu_1^{\text{sim}} = 7.326\,13\,\text{GHz} \tag{4.5}$$
$$\nu_1^{\text{exp}} = 7.325\,37\,\text{GHz}\,. \tag{4.6}$$

The theoretical prediction varies around 3 % from the experimental and simulated value, which needs to be kept in mind for the evaluation of the results later on, but nevertheless ensures consistency.

5. Sample as perturbation of planar microwave waveguide resonators

This chapter reviews the suitability of two different microwave waveguide resonators for dielectric measurements of bulk samples utilizing the cavity perturbation technique. This method was already explained in detail in chapter 3.4. In equation (2.9) and (2.10) the resonance frequencies of a $\lambda/2$-resonator and $\lambda/4$-resonator, respectively, are defined. The effective dielectric constant ϵ_{eff} plays a major role since it does not only depend on the dielectric constant of the sample but also takes into account effects by the waveguide like multiple substrates and geometry. By placing a sample inside a resonator, ϵ_{eff} changes, leading to a different resonance frequency compared to an empty cavity. The dielectric properties are then obtained with this shift in frequency, using for example the conformal mapping method introduced in 2.2.
In the first part the CPW resonator with an external bulk dielectric is examined by firstly simulating the model, then verifying the insights in experiments and concluding in a discussion part where both is put in relation. The same approach holds for the second part where a microstrip resonator with an added bulk sample is studied: First simulation, then experiment and lastly in a discussion part. In figure 5.1 both investigated designs are shown with the electric field highlighted which penetrates the bulk sample.

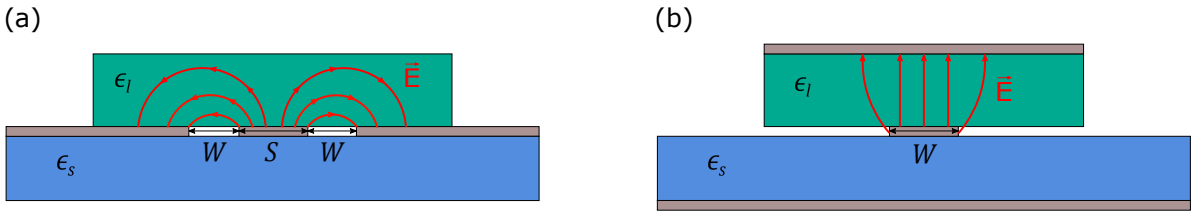

Fig. 5.1.: Schematic cross-section of (a) a coplanar waveguide (b) a microstrip with sample placed on each and the penetrating electric field displayed.

5.1. Coplanar waveguide resonator

Most of the electric field of a CPW is concentrated in the gaps between inner and outer conductor, however, the space above the conductor is partially filled by the electric field. A $\lambda/4$-resonator design is checked like depicted in figure 2.2(b), where the resonator is coupled inductively to a common transmission line. This design revealed a convenient functionality for dielectric measurements in preliminary studies [25]. In figure 5.2 this design is depicted with a bulk sample placed over the resonator.

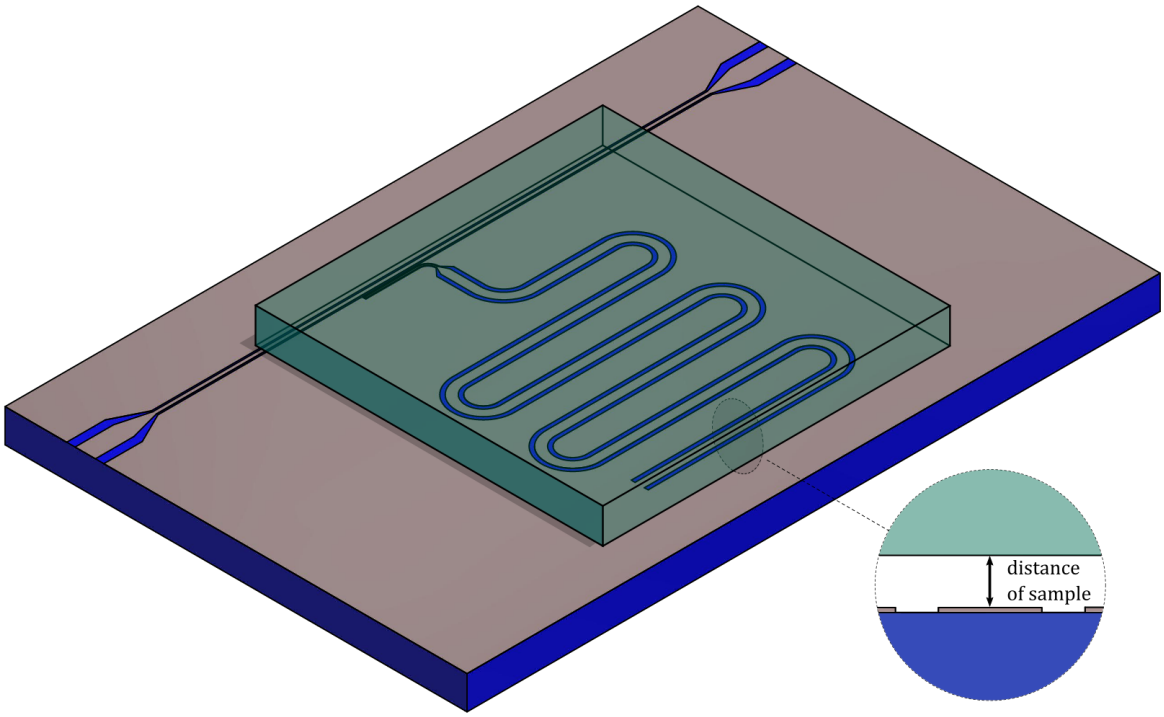

Fig. 5.2.: Schematic layout of a CPW $\lambda/4$-resonator coupled to a feedline with an external bulk sample (dark green transparent) on top. The distance between the dielectric sample and the conductive layer belongs to an air gap. Resonator and feedline are on the same substrate (blue). The simulations and experiments for a CPW with a sample utilize this design.

5.1.1. Simulations

First of all, the overall applicability of such a design is under test using simulations. To do so a resonator as in figure 2.2(b) is created with *CST Microwave Studio*. On a dielectric substrate with $\epsilon_s = 10$ and height $h_s = 430\,\mu m$ (corresponding to the material Al_2O_3) a $\lambda/4$-resonator is shaped into a perfectly conducting material (corresponding to a superconductor, e.g. Nb) of thickness $t = 300\,nm$. This values are chosen since they correspond to previous works where Nb with this thickness was sputtered on a Al_2O_3 substrate with this height [25]. For the transmission line (so-called feedline) and the actual resonator the geometry parameters

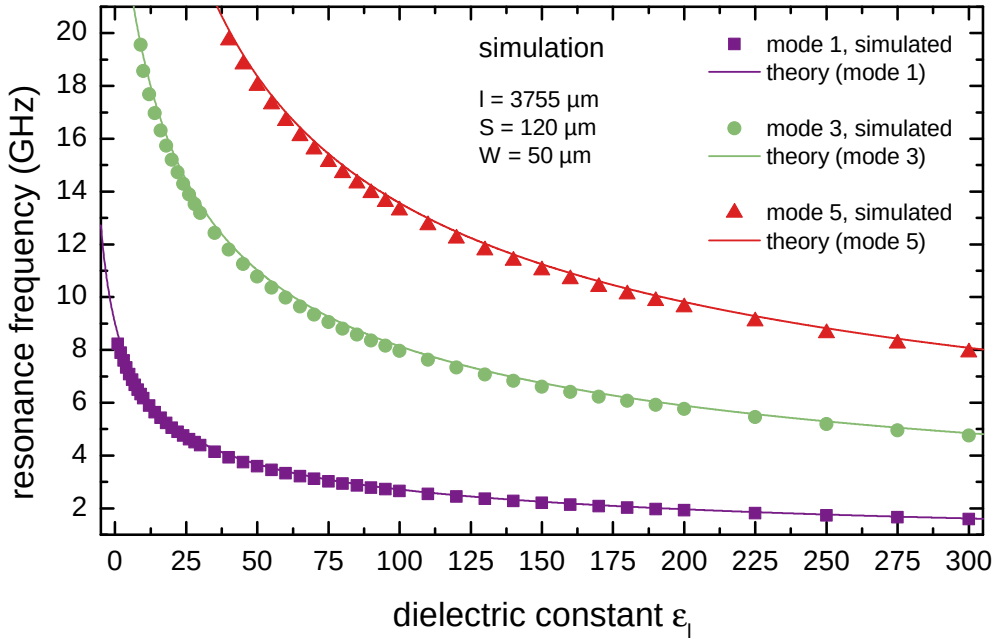

Fig. 5.3.: Simulation of the depicted design in figure 5.2 with $l = 3755\,\mu\text{m}, S = 120\,\mu\text{m}$, $W = 50\,\mu\text{m}$ and external sample placed on top at zero distance. The dielectric constant of the sample is swept up to a value of $\epsilon_l = 300$ and the obtained resonance frequencies are compared for the fundamental and two following harmonics to the theoretical predictions according to equation (2.10).

S, W must be adjusted to match the impedance of the CPW) to the standard of $50\,\Omega$ for coaxial cables and microwave connectors. Here a ratio of $S/W = 2.4$ is found (cf. equation (2.26)). The resonator is built with a total length of $l = 3755\,\mu\text{m}$ with a parallel arm to the feedline of length $500\,\mu\text{m}$ and a related resonance frequency of $\nu_1 = 8.255\,\text{GHz}$ of the fundamental mode.
Subsequently, a bulk dielectric sample with height $h_l = 500\,\mu\text{m}$ is placed with zero distance over the substrate, covering only the whole resonator. All dielectrics, substrate as well as sample are assumed to be lossless within the simulations. The dielectric constant of the sample is then swept up to a value of $\epsilon_l = 300$ and the shifted resonance frequencies ν'_n for fundamental and higher harmonic modes are obtained. These values are then compared to theoretical predictions using equation (2.10) with ϵ_{eff} calculated with the conformal mapping technique (cf. equation (2.23)). The results are displayed in figure 5.3. The simulated frequencies fit perfectly for all displayed modes to the prediction, minor deviations may origin from the mesh density or the fact that the simulations are performed lossless. A CPW $\lambda/4$-resonator would therefore be a suited candidate to measure bulk dielectrics.

Non-zero distance considerations

The above fit between simulation and theory is only valid for zero distance between resonant structure and sample, however, in real experiments a non-zero separation should be expected

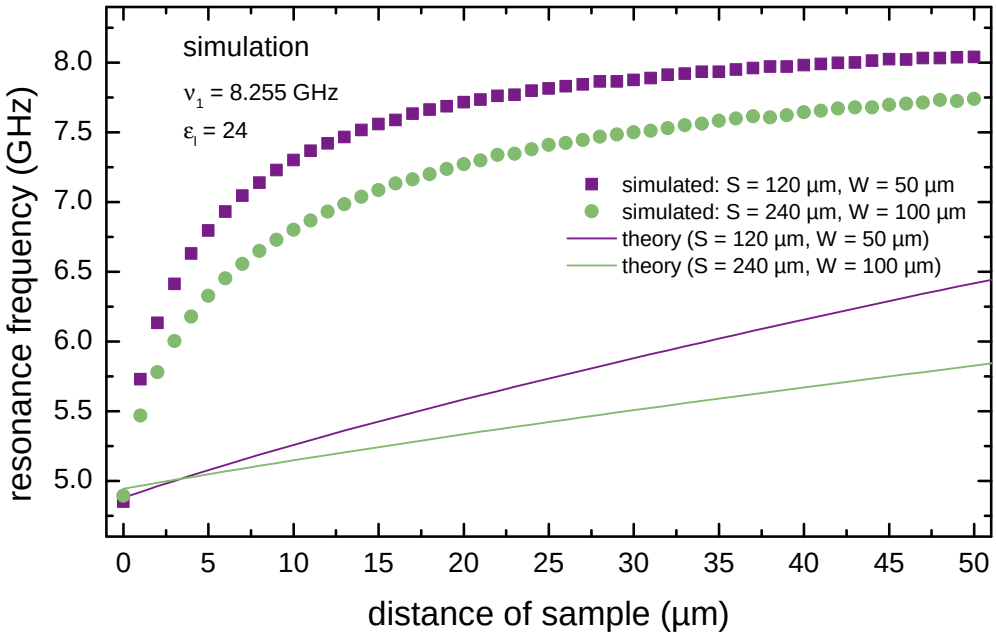

Fig. 5.4.: Simulation of the shown design in figure 5.2 for $l = 3755\,\mu\text{m}$ and external sample with $\epsilon_\text{l} = 24$ placed on top. The distance of the sample is swept from zero to 50 µm for $W = 50\,\mu\text{m}$ and $W = 100\,\mu\text{m}$ and the obtained frequencies of the fundamental modes are compared to the theoretical prediction.

due to of imperfections and roughness between sample and resonator. This is displayed in figure 5.2 with an additional distance between sample and resonator chip. Furthermore, the penetration of the electric field can be manipulated by the gap width W between inner and outer conductor as suggested in figure 5.1(a), meaning a larger W should cause a larger fraction of the field penetrating the sample. To account for these effects, the same model as above is used but the permittivity of the sample is fixed at $\epsilon_\text{l} = 24$ (corresponding to the material LAO), whereas the distance of the sample is swept from zero up to 50 µm for two different values of W. Moreover, only the fundamental mode is considered. Again, the simulated frequencies are compared to the theory which can be seen in figure 5.4.
Firstly, what catches the eye is the frequency shift of the simulated values for increasing distance of the sample for both gap widths of the resonator. Moreover, this shift is rather large even for a slim distance of 1 µm. This can be contributed to the effects of an air gap between the conductive structure and the sample, introduced in chapter 3.5. Because of the discontinuity at the sample boundary caused by the additional space, depolarization effects occur and only a fraction of the electric field can penetrate the sample. This can be illustrated by looking at the dependence of the resonant frequency of the effective dielectric constant: According to equation (2.10) it holds $\nu_1 \propto \frac{1}{\sqrt{\epsilon_\text{eff}}}$, where the ϵ_eff is (roughly) a composition of the permittivities of substrate, air gap and sample

$$\epsilon_\text{eff} = \tilde{\epsilon}_\text{substrate} + \tilde{\epsilon}_\text{gap} + \tilde{\epsilon}_\text{sample}\,. \tag{5.1}$$

The contribution of the substrate $\tilde{\epsilon}_{\text{substrate}}$ is always constant.
Zero distance: $\tilde{\epsilon}_{\text{gap}}$ vanishes and $\tilde{\epsilon}_{\text{substrate}}$, $\tilde{\epsilon}_{\text{sample}}$ define the resonance frequency.
Non-zero distance: $\tilde{\epsilon}_{\text{gap}}$ has a slight contribution and due to the depolarization effects the field does not sufficiently penetrate the sample causing a small contribution of $\tilde{\epsilon}_{\text{sample}}$. This leads to a smaller ϵ_{eff} compared to the zero distance case and therefore to a higher resonance frequency. For increasing distance the contribution of $\tilde{\epsilon}_{\text{air}}$ increases while $\tilde{\epsilon}_{\text{sample}}$ decreases which leads to a stabilization of ϵ_{eff} and a saturation in the resonance frequency.
By looking at the resonance frequencies for different W's in figure 5.4 the upper explanation can be confirmed: A larger width between inner and outer conductor causes a higher fraction of the electric field in the sample, despite the depolarization effects. Therefore the behavior for increasing distance is the same but ϵ_{eff} is larger which decreases the values of the resonance frequency compared to the smaller width.
Also, by looking at figure 5.4, the resonance frequencies obtained by simulation strongly differ from the theoretical predictions. If we look at the conformal mapping technique in chapter 2.2 the air gap can be considered in the calculation for the effective dielectric constant by adding an additional dielectric layer as depicted in figure 2.3. This leads to an effective dielectric constant and the shown resonance frequency values, which are below the simulated ones. Within the conformal mapping technique all partial regions are perfectly filled with the electric field and the discontinuities at the boundary between sample and air gap are not considered [41]. Since depolarization effects are absent, the field can surpass the boundary unaffected, while in reality it is strongly weakened there. This strong discrepancy between theory and simulation is therefore caused by the effects of boundary discontinuities which are considered in simulation but not in theory, making the theory unusable to describe the simulated results. This needs to be verified or falsified with the help of experiments.

5.1.2. Experiments

To check the suitability of coplanar waveguide resonators for bulk dielectric measurements a $\lambda/4$-resonator with total length of $l = 19\,435\,\mu\text{m}$ is shaped out of a Nb layer with thickness $t = 300\,\text{nm}$ on a Al_2O_3 substrate with height $h_s = 430\,\mu\text{m}$. To match the impedance of the resonator to the $50\,\Omega$ of the microwave connectors, $S = 120\,\mu\text{m}$ and $W = 50\,\mu\text{m}$ are chosen corresponding to the ratio of $S/W = 2.4$. A list with the relevant parameters can be found in the appendix in table A.1. The unloaded resonator is then measured at a temperature of around 1.5 K. At this temperature the Nb layer is superconducting, reducing the losses only to the dielectric substrates. The fundamental resonance frequency of the unloaded resonator is found to be $\nu_1 = 1.653\,\text{GHz}$, which is in good agreement with the theory (cf. chapter 4.3). Afterwards, a bulk LAO sample with height $h_l = 500\,\mu\text{m}$ is placed over the resonator in the cavity and the measurement is repeated at the same temperature. The resulting spectrum is displayed in figure 5.5.
By placing the sample onto the resonator, the resonance frequency shifts as predicted by the cavity perturbation theory. To quantitatively analyze the shift of the fundamental frequency from unloaded to filled resonator, equation (2.10) for both cases are used. The ratio of the

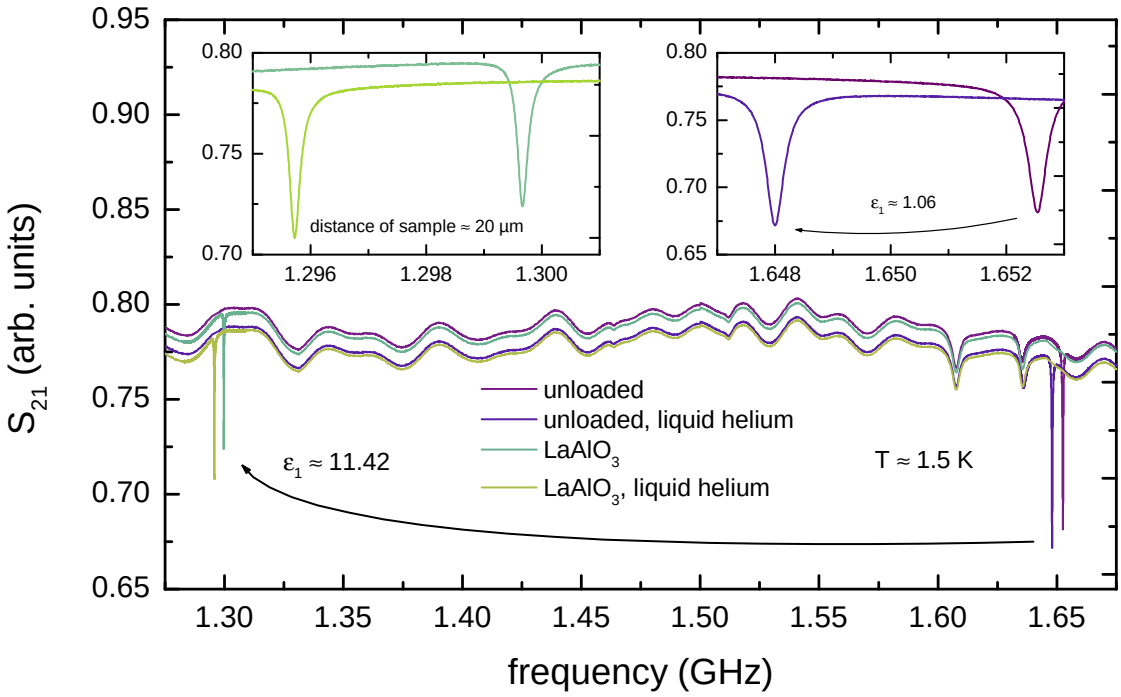

Fig. 5.5.: Spectrum of the measured fundamental resonance frequency of a CPW $\lambda/4$-resonator as depicted in figure 5.2 around a temperature of 1.5 K. Shown is the unloaded result (corresponding to figure 5.2 without sample) and the result with a bulk LAO sample paced on top of the resonator. Additionally, the effect with solely liquid helium over the resonator and the effect of liquid helium filling the separation between sample and resonator are displayed. The resonance frequencies of unloaded and loaded resonator shift with liquid helium included, depicted in both insets.

original frequency to the shifted one can be expressed by the inverse ratio of the roots of the the according effective dielectric constants:

$$\frac{\nu_1}{\nu_1'} = \sqrt{\frac{\epsilon_{\text{eff}}'}{\epsilon_{\text{eff}}}}\,. \tag{5.2}$$

With the unloaded resonance frequency $\nu_1 = 1.653\,\text{GHz}$, the loaded resonance frequency $\nu_1' = 1.300\,\text{GHz}$ and the effective dielectric constants $\epsilon_{\text{eff}} = 5.42$ of the unloaded resonator. With the conformal mapping technique the dielectric constants can be calculated from ϵ_{eff}'. For the unloaded resonator the Al_2O_3 substrate and the vacuum above the conductive structure define the effective dielectric constant ϵ_{eff}. For the filled resonator the dielectric constant of the sample are obtained by calculating equation (5.2) for ϵ_{eff}' and then solving equation (2.23) for the desired ϵ_1. With the above mentioned values this frequency shift is attributed to a dielectric constant of the sample of

$$\epsilon_{1,\,\text{LAO}} = 11.42\,, \tag{5.3}$$

whereas the literature value of the dielectric constant of the used LAO sample is at $\epsilon_{1,\,\text{LAO}}^{\text{Lit}} = 24$ [84]. With the literature value a frequency shift to even lower frequencies would have been

expected, however, this strong divergence will be discussed below.
In the analysis for the determination of the permittivity of the sample by evaluating the frequency shift, an additional separation between the Nb structure and the LAO sample is already included. For the calculation a distance of 20 µm is assumed, this value is selected due to the evaluation of effects of liquid helium in the resonator box.

Determination of the separation of sample and resonator due to liquid helium measurements

Measurements are performed with an unloaded and filled resonator, both with vacuum inside the resonator box or filled with liquid helium. To achieve vacuum inside the resonator box, the sample chamber is heated above the boiling point of helium, cooled again and the measurement is immediately started. For the measurement with filled helium, the needle valve is slightly opened to let helium inside the sample chamber. First of all, the dielectric constant of liquid helium utilizing the CPW $\lambda/4$-resonator is determined. To do so, the resonance shift from the unloaded resonator to the liquid helium filled one is analyzed, which is displayed in figure 5.5 in the right inset. The permittivity of liquid helium is found with

$$\epsilon_{1,\,\mathrm{li.He.}} = 1.06\,, \tag{5.4}$$

which in good agreement with the literature value of [90]. This result can be well compared to preliminary studies where it was shown that CPW superconducting resonators can be used to measure the permittivity of helium by direct contact to the helium bath [91].
To give now an approximation of the separation between conductive layer and sample the loaded resonator is also measured with vacuum and liquid helium which can be seen in figure 5.5 in the left inset. Then the resonance frequency shifts from the unloaded resonator to the loaded resonator, from the unloaded resonator to the loaded resonator with liquid helium and from the loaded resonator to the loaded resonator with liquid helium are compared. An initial guess of the gap is assumed and then the shifts are analyzed according to equation (5.2) for the permittivity of the liquid helium filled gap. This approach is repeated to match this obtained permittivity to the one above (5.4) gained from the unloaded measurements. With this procedure the separation between resonator and sample is approximately found to be 20 µm. This value seems reasonable considering the possible imperfections and roughness existing on sample or conductive structure or being introduced during sample placement.

5.1.3. Discussion

The suitability of CPW resonators for bulk dielectrics was under review by simulating and measuring it with an external bulk sample. In the first step a modeled resonator was simulated to check for if the theory fits to the simulated results. For a zero distance of the dielectric sample over the resonant structure it was shown that the simulated resonance frequencies for a certain dielectric constant fit very well to the theoretical prediction, which is depicted in figure 5.3. In real experiments however zero distance is not achieved, since due to imperfections and roughness a separation of around 20 µm can be assumed. This distance could be confirmed in the experiment with the help of liquid helium measurements. Simulations and experiment

show that the effective dielectric constant is too small. Since gap discontinuity effects between boundary of conductive layer and dielectric sample occur, an immense loss of intensity of the electric field is caused. As a result the dielectric Due to the rather small influence of the sample, the effective dielectric constant decreases with increasing separation leading to a strong shift to higher frequencies. In the experiments this was proven by measuring an unloaded resonator compared to a filled one with a bulk LAO sample. The resonance shift could be assigned to a dielectric constant of around 11.42 which differs strongly from the literature value of 24. This is due to the fact that the electric field does not penetrate the sample well due to depolarization effects at the boundary. A larger width between inner and outer conductor can slightly compensate for this depolarization but even larger widths do not lead to the desired result.
Another problem which occurred was that the theoretical prediction does not fit to the results for a non-zero distance. Whereas in simulations and experiments this depolarization effects come into play leading to insufficient field in the sample and to a smaller effective dielectric constant, this does not play a role in the theory provided by the conformal mapping technique. In the method an additional dielectric gap can be easily assumed, however there are no discontinuity effects included which causes each part being completely filled by the electric field. Hence, the effective dielectric constant is larger than the one which is obtained in simulation and experiment.
As a consequence this makes CPW resonators not suitable to obtain exact results in dielectric measurements of bulk samples. The main feature is the electric field which does not penetrate the dielectric sufficiently due to effects in the non-zero gap between conductor and sample. Furthermore, the frequency shift caused by the sample cannot be correctly analyzed with the conformal mapping technique since discontinuity effects at the boundary are not included.

5.2. Microstrip resonator

The waveguide under study now is the microstrip, where a conductor-backed dielectric substrate has an inner conductor of width W on top of it. To study a dielectric material, it needs to be placed on top of the inner conductor and a further conductive layer backs the sample, creating a so-called embedded transmission line (ETL) [54]. This leads then to the highlighted electric field in figure 5.1(b) going through the sample. The electric field distribution can be manipulated by changing the width of the inner conductor. Since inner and outer conductor are separated by the substrate, it is convenient to shape a $\lambda/2$-resonator by introducing gaps in the inner conductor, which is shown in figure 5.6. The overall setup is similar to a stripline waveguide, where the dielectrics sandwiching the inner conductor are of the same material and the additional conductive layer on top is under study [32].

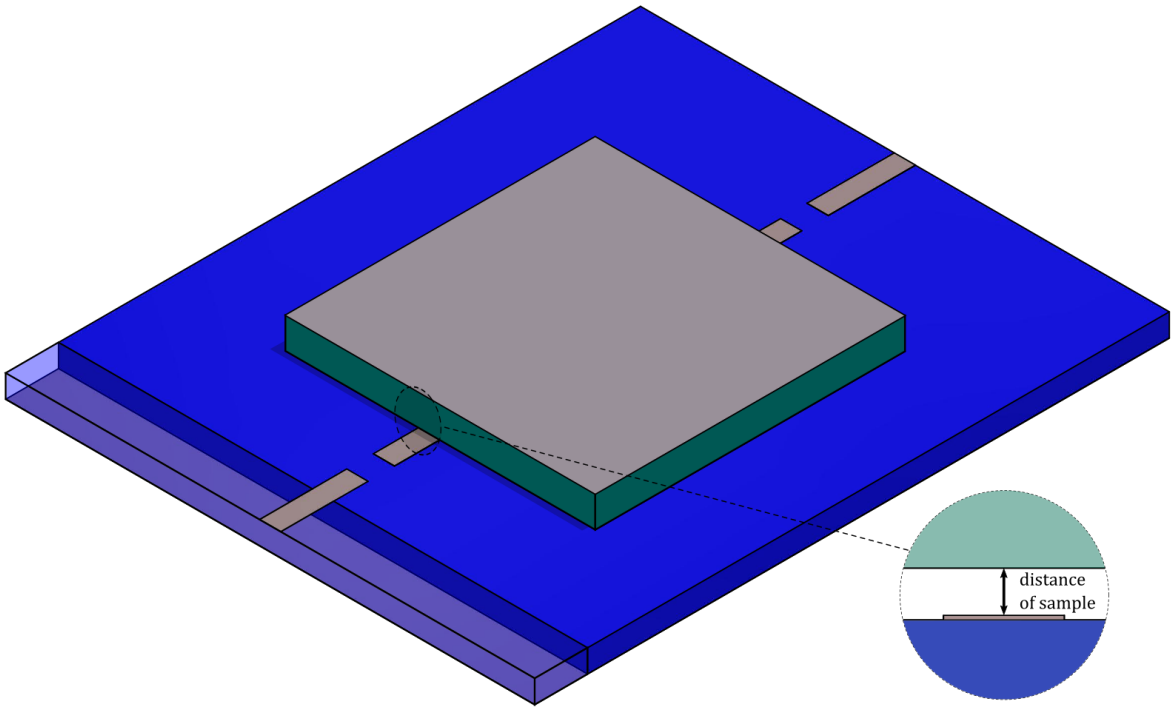

Fig. 5.6.: Schematic layout of a microstrip $\lambda/2$-resonator with an external bulk sample (dark green) on top. The sample has a conductive layer on top and is placed between the gaps of the inner conductor. The substrate (blue) has a conductive sheet on the back side which can be seen in the transparent part. The distance between the dielectric sample and the inner conductor belongs to an air gap. The simulations and experiments for a microstrip with a sample utilize this design.

5.2.1. Simulations

As for the CPW, the suitability of a microstrip resonator for external dielectric bulks is firstly tested in simulations. All dielectrics are simulated lossless. First of all a simple microstrip

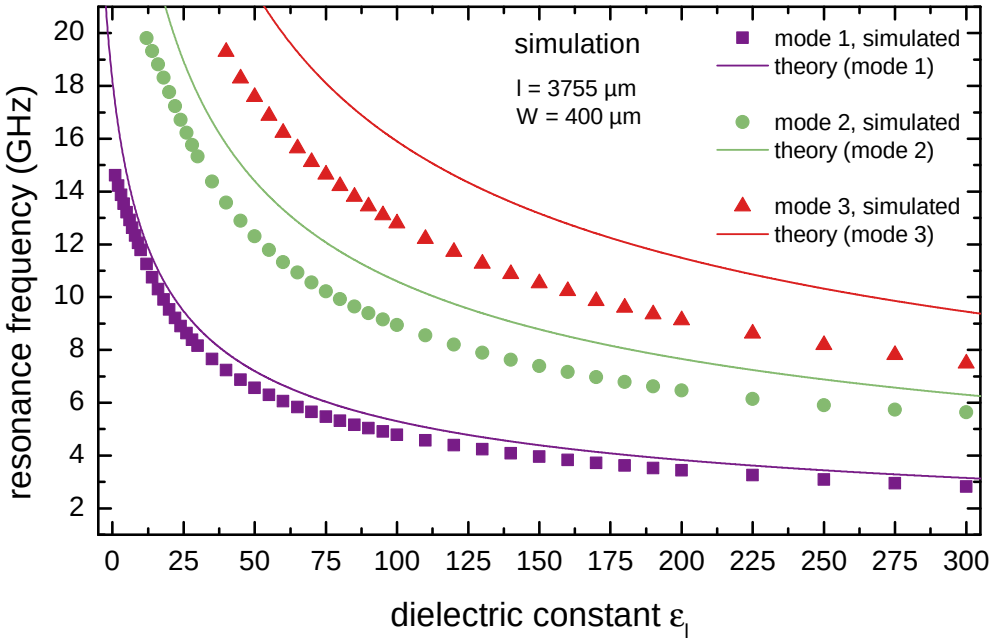

Fig. 5.7.: Simulation of the shown design in figure 5.6 with $l = 3755\,\mu\text{m}, W = 400\,\mu\text{m}$ and an external sample placed on top at zero distance. The dielectric constant of the sample is swept up to a value of $\epsilon_\text{l} = 300$. and the obtained resonance frequencies are compared for the fundamental and first two harmonics to the theoretical predictions according to equation (2.9).

resonator without sample is designed. Over a conductor a dielectric substrate with $\epsilon_\text{s} = 10$ and height $h_\text{s} = 430\,\mu\text{m}$ (corresponding to the material Al_2O_3) an inner conductor with width W is shaped. Both conductors are assumed to be perfectly conducting (corresponding to a superconductor) and have a thickness of $t = 1\,\mu\text{m}$. To match the impedance of the microstrip to the $50\,\Omega$ standard, equation (2.27) is used and $W = 400\,\mu\text{m}$ is found. To create a $\lambda/2$-resonator, gaps in the inner conductor at a distance $l = 3755\,\mu\text{m}$ are introduced leading to a fundamental resonance frequency of $\nu_1 = 14.619\,\text{GHz}$ of the microstrip resonator.
Afterwards, a bulk sample of height $h_\text{l} = 500\,\mu\text{m}$ is created a zero distance over the inner conductor covering the resonator gap to gap. The dielectric constant of the sample is then swept up to a value of $\epsilon_\text{l} = 300$ and the shifted resonance frequencies ν'_n for fundamental and higher harmonic modes are obtained. These values are then compared to theoretical predictions using equation (2.10) with ϵ_eff calculated with equation (2.29). The results are displayed in figure 5.7. Theory and simulated results seem to fit for the fundamental mode, however, there is a certain difference which is even more distinctive for the second and third mode. To validate for this difference the permittivity of the sample is fixed with $\epsilon_\text{l} = 24$ and the resonance frequencies obtained by simulation and theory are compared for different values of the width W of the inner conductor.
The results are displayed in table 5.1. The simulated frequencies increase with decreasing conductor width which is expected. For decreasing width the amount of the electric field penetrating the sample decreases (cf. figure 5.1(b)) causing a reduction of the effective

Tab. 5.1.: Comparison of resonance frequencies of an ETL resonator with $\epsilon_l = 24$ of the sample for simulated results and theoretical predictions. The impact of the inner conductor width is depicted for five different values.

	res. freq. (GHz)	
width (µm)	simulation	theory
400	8.905	9.607
200	9.031	9.621
100	9.138	9.626
40	9.246	9.634
10	9.352	9.600

dielectric constant. This leads then to an increase in the resonance frequency since it holds $\nu \propto \frac{1}{\sqrt{\epsilon_{\text{eff}}}}$. In the theoretical prediction however, the resonance frequency changes only a little for an decrease of the width. In equation (2.29) the width is considered but obviously does not have much of an impact. For $W = 10\,\mu\text{m}$ simulated and theoretical values fit well with respect to the mesh size of the simulation. To match the resonator impedance to $50\,\Omega$ the width needs to be $W = 400\,\mu\text{m}$, where a difference of almost 1 GHz can be observed. For the second and third mode this difference then doubles or triples, respectively, shown in figure 5.7.

Non-zero distance considerations

Due to the real non-zero separation between sample and conductor which was already discussed in the upper analysis of the CPW, the above used ETL model is used to consider this non-zero distance. To do so the dielectric constant of the sample is fixed with $\epsilon_l = 24$ and the separation is increased step by step. In figure 5.8 the simulated results are displayed. The explanation of the behavior of the obtained resonance frequencies can be inherited from the non-zero distance considerations for the CPW above (cf. chapter 5.1.1): For non-zero distance ϵ_{eff} and ν_1 are defined by the permittivity of substrate and sample and can be described by the theoretical prediction. With an additional gap present the impact of the permittivity of the sample decreases due to depolarization effects at the sample boundary, while at the same time the impact of the permittivity of the gap increases. Thus, the behavior of the resonance frequency as a function of separation thickness is similar for an external sample on a CPW resonator or a microstrip resonator.
Another problem is that the theoretical model assumes only one dielectric layer above the inner conductor to calculate ϵ_{eff} [54]. For an additional layer on top to express the gap the theory gives no formula to calculate ϵ_{eff}. Therefore, the theoretical behavior for a separation between sample and conductor cannot be determined. Maybe the discontinuity effects at the sample boundary could be considered in a possible theory, or it is not considered at all as in the conformal mapping technique for the CPW. Anyway, ϵ_{eff} and ν_1 cannot be theoretically predicted for a non-zero distance. However, the simulation based results must be compared to experiments.

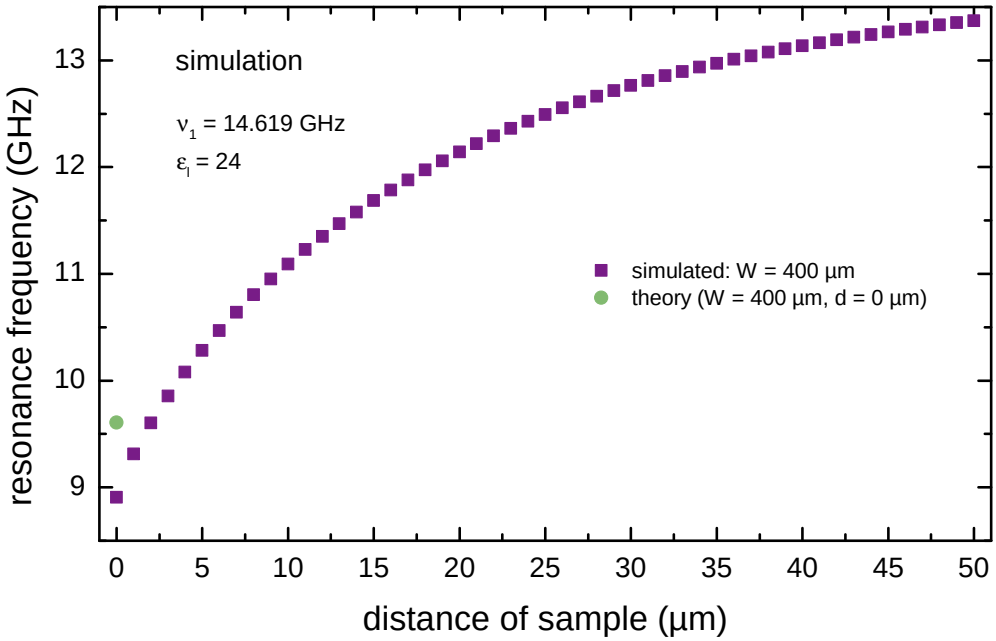

Fig. 5.8.: Simulation of the shown design in figure 5.6 $l = 3755\,\mu\text{m}$ and an external sample with $\epsilon_\text{l} = 24$ placed on top. The distance of the sample is swept from zero to $50\,\mu\text{m}$ for $W = 400\,\mu\text{m}$ and resonance frequency of the fundamental mode is obtained. The theoretical model states only a resonance frequency for zero distance between the sample and the inner conductor.

5.2.2. Experiments

To examine the applicability of microstrip resonator for measuring the dielectric properties of bulk samples a $\lambda/2$-resonator is created. A Al_2O_3 substrate with height $h_\text{s} = 430\,\mu\text{m}$ and permittivity $\epsilon_\text{s} = 10$ is backed with a conductive sheet. On top a conductive transmission line is shaped with $W = 400\,\mu\text{m}$ and two gaps $g = 500\,\mu\text{m}$ at distance of $l = 7700\,\mu\text{m}$. The width is chosen like this to match the impedance to the $50\,\Omega$ of the microwave connectors. Conductive sheet as well as inner conductor have a thickness of $t = 1\,\mu\text{m}$ and are made out of lead which is superconducting below 7 K. A list with the relevant parameters can be found in the appendix in table A.2. With a VNA the transmission spectrum is measured at around 1.5 K and the fundamental and first harmonic mode are identified at $\nu_1 = 7.325\,\text{GHz}$ and $\nu_2 = 14.263\,\text{GHz}$, respectively. These values differ slightly from the theoretical prediction (cf. chapter 4.3). Following this a bulk LAO sample with height $h_\text{l} = 500\,\mu\text{m}$ is placed over the resonator from gap to gap, a conductive layer on top with a foil is implemented and the measurements is repeated at the same temperature. In figure 5.9 the spectrum of an unloaded and filled microstrip resonator is depicted with the resonance frequencies highlighted.
Utilizing the cavity perturbation technique the resonance shift is analyzed. To do so equation (5.2) is applied to determine the effective dielectric constant ϵ'_eff of the filled cavity. This must be done for the first and second mode separately but for both cases the effective dielectric constant of the unloaded resonator $\epsilon_\text{eff} = 6.63$ is used. The desired dielectric constant of the

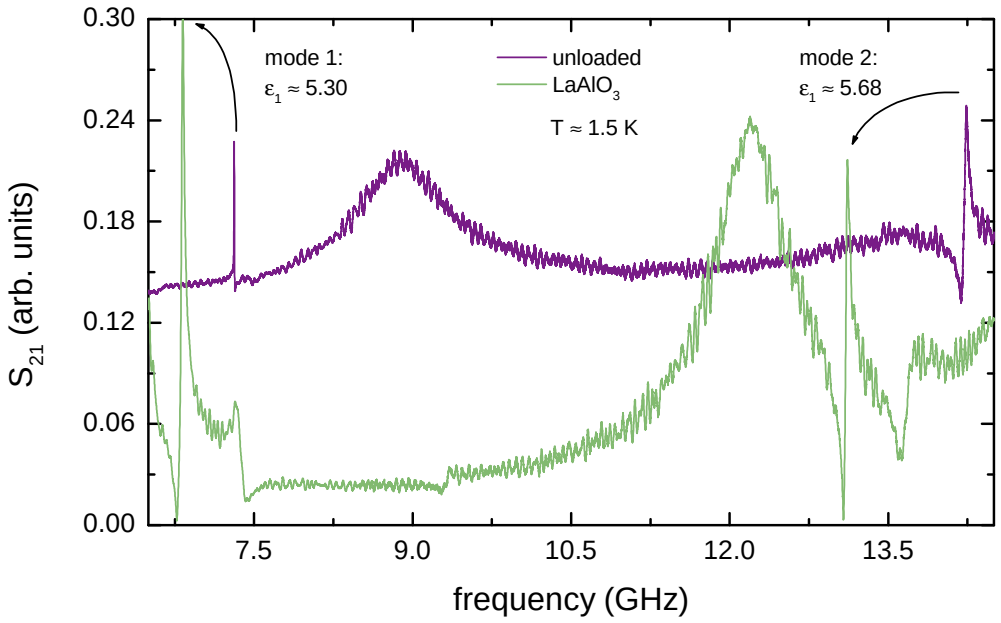

Fig. 5.9.: Spectrum of the measured fundamental and first harmonic resonance frequency of a microstrip $\lambda/2$-resonator around a temperature of 1.5 K. Shown are besides the unloaded results the resonance frequencies after placing a bulk LAO sample on the microstrip (cf. figure 5.6 with and without sample).

sample can then be calculated by employing equation (2.29). With the unloaded resonance frequencies mentioned above and the resonance frequencies with implemented sample of $\nu_1' = 6.385\,\mathrm{GHz}$ and $\nu_2' = 13.172\,\mathrm{GHz}$ the resonance shift is attributed to a permittivity of

$$\epsilon_{1,\,\mathrm{LAO},\,\mathrm{mode}\,1} = 5.30\,, \tag{5.5}$$

$$\epsilon_{1,\,\mathrm{LAO},\,\mathrm{mode}\,2} = 5.68\,. \tag{5.6}$$

These values differ vastly from the literature value of the dielectric constant of $\epsilon^{\mathrm{Lit}}_{1,\,\mathrm{LAO}} = 24$. This is due to the assumption of a zero distance in equation (2.29), which is not the case due to the extensively discussed impurities. For a non-zero distance there is no tool to analytically determine this resonance shift, therefore the real permittivity of the sample cannot be studied.

5.2.3. Discussion

The microstrip resonator was under review to host an external bulk sample. Due to the design, the microstrip should be well suited for bulk dielectrics due to the homogeneous field penetration compared to the electric field contribution in a sample placed on top of a CPW. At first the model was tested with simulations and the obtained resonance frequencies were compared to the theoretical predictions. A difference could be observed, which was attributed to the conductor width. In simulations this parameter has an influence whereas it is not considered in the theory (cf. table 5.1). In addition, the theory cannot make a statement if there are two dielectric layers over the inner conductor. This is relevant due to the real

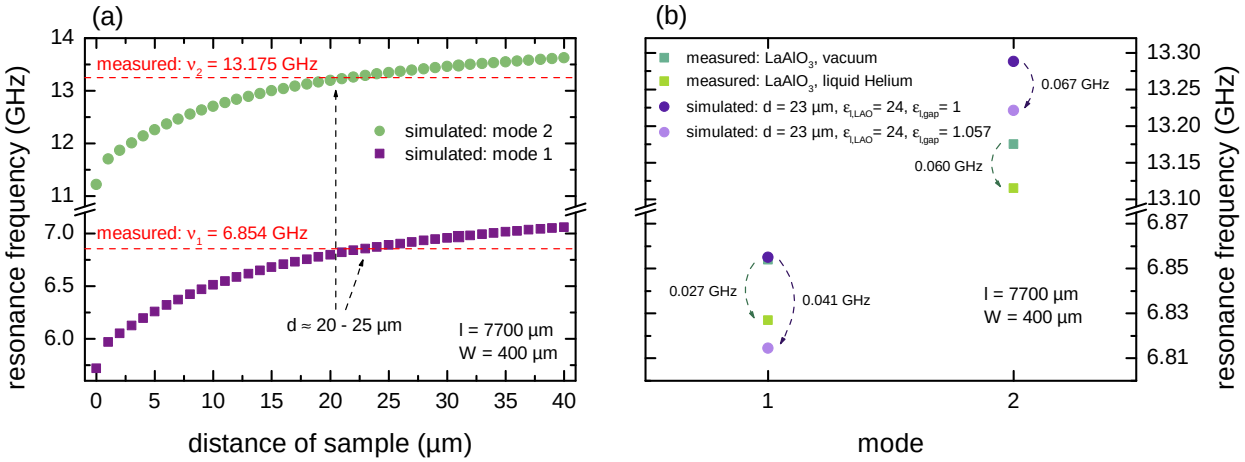

Fig. 5.10.: (a) Simulation of the recreated model of the resonator used in the experiment with the design depicted in figure 5.6. The distance of the sample is swept and the obtained resonance frequencies are compared to the measured frequencies. (b) Comparison of resonance frequencies of loaded resonator with and without liquid helium to the simulated model at a distance of 23 µm for the first and second mode.

non-zero distance between sample and conductor. Despite this two problems a microstrip resonator was created and measured without and with sample placed on top. As predicted by the cavity perturbation theory there is a resonance shift between unloaded and loaded measurement. However, this shift cannot be correctly analyzed due to the limitation of the theory to a zero distance.

To nonetheless give a statement about the gap thickness the measured resonator with sample was exactly recreated within the simulations with $\epsilon_l = 24$ of the sample and then the distance of sample to conductor was swept. The obtained resonance frequencies are shown in figure 5.10(a). For increasing distance the resonance frequency shifts to lower frequencies due to the decreasing effective dielectric constant. The results are compared to the measured resonance frequencies of the loaded microstrip. As depicted, there is an match of simulated and experimental values for the fundamental and first harmonic mode for a separation of around $20 - 25\,\mu m$. This value seems reasonable as it is of the same magnitude as for the determination with liquid helium measurements with the CPW (cf. chapter 5.1.2). To check this, the simulated microstrip was fixed for a sample distance at 23 µm and then simulated with permittivity of $\epsilon_{l,\,gap} = 1$ (corresponding to vacuum) and $\epsilon_{l,\,gap} = 1.057$ (corresponding to liquid helium), respectively. The obtained frequencies are compared to the measured resonance frequencies for loaded microstrip resonator with and without liquid helium inside the sample chamber. In figure 5.10(b) the results for the first and second mode are displayed. The shift due to the presence of liquid helium is of the same magnitude for the measured results as for the simulated ones for both modes. The simulated results depend on the mesh size and all simulations do not consider any effects due to losses in the superconductor or dielectrics. Thus, they give only an estimation but it is sufficient to confirm the thickness of

the separation of around 20 µm, which was also found with the liquid helium measurements with the CPW resonator.
Microstrip resonators are principally suited to measure dielectric properties of bulk samples since the design provides a homogeneous electrical field distribution through the sample. However, the analytical tools to determine the properties are not available for a non-zero distance of the sample, which is existing in real experiments. Therefore, the effects of the separation cannot be considered and the correct calculation of the permittivity of the sample is not possible. When placing a bulk sample on top of a CPW or microstrip resonator, it is difficult to correctly determine the dielectric properties of the material under study. This addresses the need of an approach where the resonator is directly deposited on the material under study.

6. Coplanar waveguide resonator shaped on top of sample

To eliminate the effects of air gaps another approach is needed: the deposition of the resonant structure directly on top of the sample under study. For this purpose the coplanar waveguide has major advantages due to its design, where inner and outer conductor are shaped on the same surface. However, there are some challenges with this approach, especially the coupling into the resonator. To match the impedance of resonator to the standard of the microwave connectors the dielectric constant must be well-known. With equation (2.26) the impedance can then be adjusted by changing the parameters S and W of the resonator. If a bulk dielectric is under study and the permittivity is unknown, the impedance of the resonator cannot be determined correctly and the signal may not couple sufficiently into the resonator to excite the fundamental and harmonic modes. Further problems are regarding the shape of the bulk sample due to the implementation in the resonator box and connection the microwave connectors. In the master thesis of M. Beutel [89] an approach is proposed where on top of a bulk sample of $SrTiO_3$ a $\lambda/2$-resonator is deposited. The sample is placed on top of a Al_2O_3 substrate, which has a simple transmission line with a space where the sample is placed. The model is investigated more precisely in the work of V. Engl [81], but it was found that this approach is not suitable for the desired measurements. However, the method of externally exciting the resonator on the sample under test is a promising foundation.
In this chapter a similar technique is presented and termed distant flip-chip method. In the first section the distant flip-chip approach is under review in simulations, where functionality and performance are examined accurately. Following, experimental preparations are examined, including the very important mounting of the resonator chip, as well as a short insight into the production of the included parts. Afterwards the experimental results are presented, with the procedure for temperature-dependent measurements as well as the investigated materials. The chapter closes with a discussion part, where the presented method is evaluated including an essential error estimation.

6.1. Distant flip-chip model

To avoid air gap effects a CPW is shaped on top of the bulk sample and externally excited. This model makes similar use of a feedline transmitting the signal and a inductively coupled $\lambda/4$-resonator. Whereas in chapter 5.1 both are one plane on the same substrate and the sample is placed on top, here feedline and resonator are separated on substrate and external sample, respectively. In figure 6.1 the distant flip chip model is displayed.
The CPW $\lambda/4$-resonator is deposited with thickness t, center conductor width S and gap

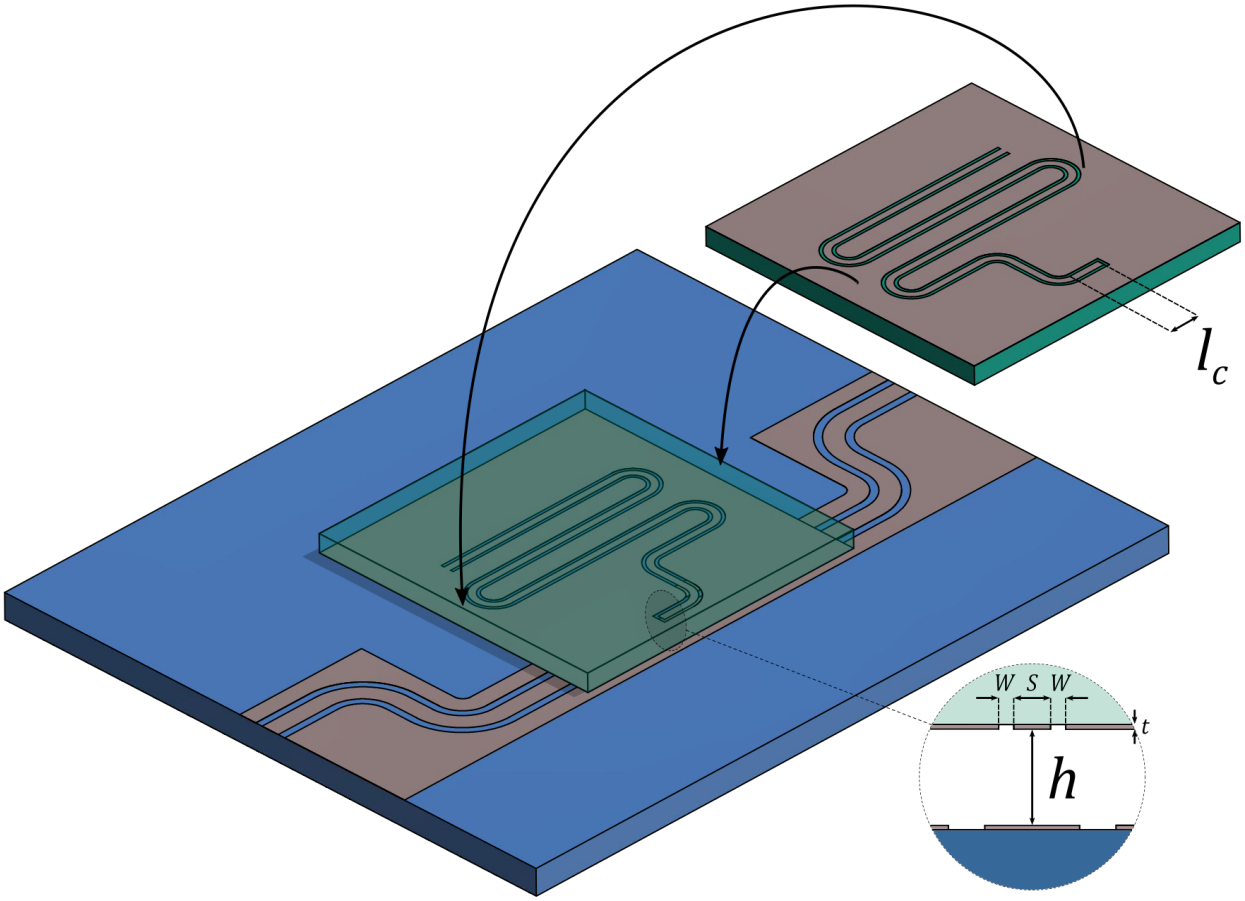

Fig. 6.1.: Scaled depiction of the introduced distant flip-chip model. The sample (dark green transparent) with deposited CPW $\lambda/4$-resonator is flipped over a common coplanar transmission line on a substrate (blue). Shown are important parameters like the distance between chip and substrate h, coupling length l_c and geometrical parameters S, W, t of the resonator.

Tab. 6.1.: List of chosen geometry values for the distant flip-chip model displayed in figure 6.1 and described in section 6.2.1.

	geometrical parameter	value (µm)
feedline	S	300
	W	120
	t	0.3
resonator	S	120
	W	50
	t	0.3
	l	3755
	l_c	500
	h	50

width W on the studied sample. The sample is then flipped and placed over a coplanar feedline in a certain distance h, so that both conductive layers are facing each other. The feedline is deposited on a substrate of well-known properties. The coplanar feedline is not spread over the whole substrate, but the outer conductors are reduced in size to prevent any side effects coming from the electric field from the resonant chip. The resonator has coupling arm with length l_c with a closed end, which is centrally placed over the center conductor of the feedline and an opposite open end. Via inductive coupling the microwave signal is transmitted and the $\lambda/4$-resonator is excited. The flipped design has the advantage that the microwave signal couples through the open space between sample and feedline, preventing losses and depolarization effects. The distance of the sample h and the coupling length l_c are of crucial importance regarding functionality and performance of the distant flip-chip method and are discussed extensively within this chapter.

6.2. Simulations

Before testing the distant flip-chip in the experiment and establishing it as a measuring method for bulk dielectrics, the model is created within *CST Microwave Studio*. Thus, the functionality can be checked by comparing it to the theoretical predictions and the performance is investigated by examining the distance of the sample h and the coupling length l_c. Within all simulations it is expected that the coupling arm is centrally aligned over the feedline.

6.2.1. Functionality

At first the functionality of the distant flip-chip is checked. Therefore, a similar model to figure 6.1 model is created. All dielectrics are assumed to be lossless and the conductor is chosen to be perfectly conducting. A coplanar feedline with $S = 300\,\mu m$ and $W = 120\,\mu m$ on top of a substrate with height $h_s = 430\,\mu m$ and permittivity $\epsilon_s = 10$ (corresponding to Al_2O_3) is created. In a certain distance a flipped chip is modeled with a CPW $\lambda/4$-resonator with $S = 120\,\mu m$ and $W = 50\,\mu m$ and total length of $l = 3755\,\mu m$ on top of a dielectric sample with height $h_l = 500\,\mu m$. Feedline and resonator have a thickness of 300 nm. The distance of the chip is fixed with $h = 50\,\mu m$ and the coupling length of the resonator is chosen with $l_c = 500\,\mu m$. The permittivity of the sample is swept up to $\epsilon_l = 300$ and the fundamental and harmonic resonance frequencies are obtained.
In figure 6.2 the results are depicted and compared with the theoretical prediction received with the conformal mapping technique. Following equation (2.10) the resonance frequencies decrease with increasing permittivity of the sample. Simulation and theory are in good agreement. However, there is a small deviation, namely that the simulated frequencies are slightly above the theoretical results. The conformal mapping states the sample as substrate with the gap and the Al_2O_3 as additional stacked dielectric layers. But the feedline is in between these two dielectric layers in the simulation. This small conductive sheet influences the electric field coming from the resonator, which penetrates into the Al_2O_3. As a consequence, the contribution of the permittivity of the Al_2O_3 reduces, resulting in a higher

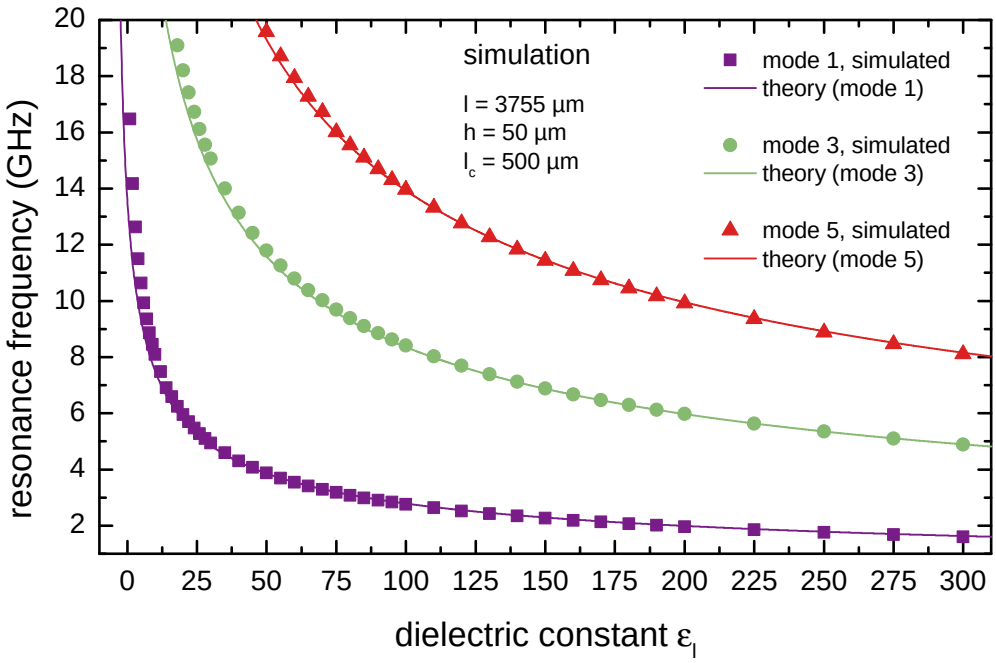

Fig. 6.2.: Fundamental and harmonic resonance frequencies of a distant flip-chip model for permittivities up to $\epsilon_\mathrm{l} = 300$ obtained within the simulation. The distance of the chip is fixed with $h = 50\,\mu\mathrm{m}$ and the coupling length of the resonator is chosen with $l_c = 500\,\mu\mathrm{m}$. As comparison the theoretical predictions for each mode are displayed.

resonance frequency compared to the prediction by the conformal mapping. This conductive sheet is not spread over the whole surface of the Al_2O_3 and has a tenable influence. This holds especially for low sample permittivities. The effective dielectric constant composes of the three dielectric layers

$$\epsilon_\mathrm{eff} = \tilde{\epsilon}_\mathrm{sample} + \tilde{\epsilon}_\mathrm{gap} + \tilde{\epsilon}_\mathrm{substrate}\,, \tag{6.1}$$

whereas the contribution of the separation and substrate are constant for a fixed distance. Since the conductive feedline is in between, this contribution is smaller than expected as explained above. For low dielectric constants of the sample this derivation dominates the effective permittivity, causing the observed difference of simulation and theory. For increasing sample permittivity the contribution of the separation and substrate is compensated, which causes simulation and theory to fit.

Influence of distance and coupling length

Subsequently, the permittivity of the sample is fixed with $\epsilon_\mathrm{l} = 24$ (corresponding to LAO) and the impact of the distance of the sample and coupling length regarding functionality is studied. To do so, the coupling length is fixed and the distance is swept. The resonance frequencies of the fundamental mode are obtained and again compared to the theory.

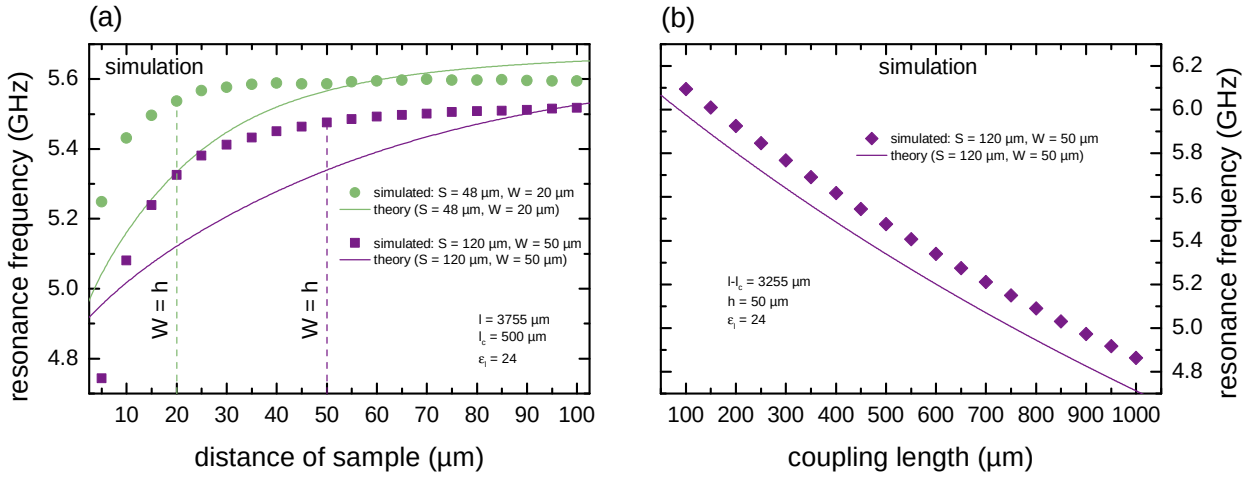

Fig. 6.3.: (a) Fundamental resonance frequency for a permittivity of the sample $\epsilon_l = 24$ and coupling length $l_c = 500\,\mu m$ for increasing distance. The resonator is simulated for different values of S, W and compared to the theory. (b) Fundamental resonance frequency for the same model with increasing coupling length l_c and fixed distance $h = 50\,\mu m$. The theoretical prediction is displayed.

In figure 6.3(a) the results are depicted for a fixed coupling length, while the distance is swept up to 100 µm. For a small distance the Al_2O_3 substrate has a large impact, which increases the effective dielectric constant and results in a smaller resonance frequency. With increasing distance of the chip over the feedline, the effect of the Al_2O_3 reduces until it is decoupled. This results in a saturation of the resonance frequency for a larger distance at higher frequencies. The value at which the frequency saturates depends on the width W of the gap in the resonator. For a smaller width the electric field should not reach the Al_2O_3 for a smaller distance. Therefore the saturation should occur at smaller distances, which can be seen in figure 6.3(a). Generally, the saturation effect starts at a distance which is approximately of the magnitude of the gap width, indicated with the dashed lines. The difference of the simulated results compared to the theory can be assigned to the feedline, which is an additional conductive sheet between the gap and the Al_2O_3. As above mentioned, this difference is of acceptable magnitude. In figure 6.3(b) the fundamental resonance frequencies are shown for a fixed distance and an increasing coupling length. Both, simulated and theoretical results decrease with larger coupling length. Since the effective dielectric constant does not change, the increasing total length is responsible for the decrease of the resonance frequency according to equation (2.10). The theory is obtained by sweeping the length in equation (2.10) from $l = 3355\,\mu m$ to $l = 4255\,\mu m$ since an increase in the coupling length l_c is an increase in the total length l.
With all important parameters taken into account the functionality of the distant flip chip is confirmed within the simulations. The above mentioned additional conductive sheet (feedline) causes a small derivation between simulation and theory, which is of acceptable magnitude. However, this should be kept in mind for an evaluation of the method in the discussion section.

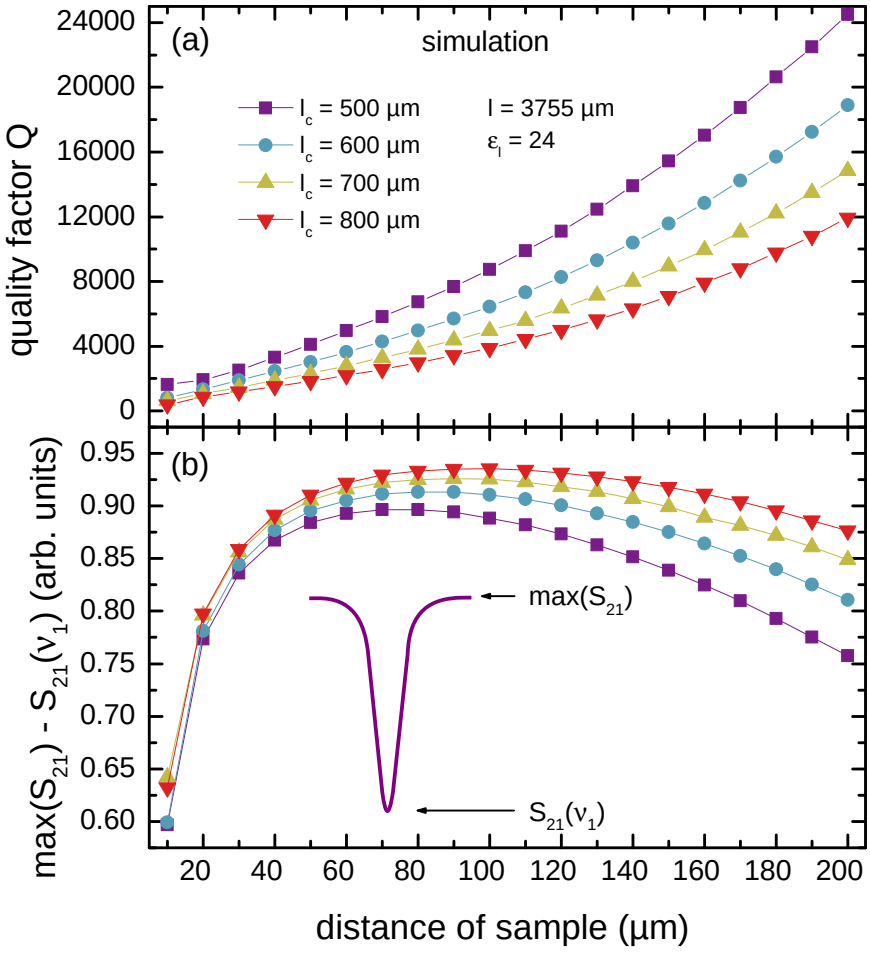

Fig. 6.4.: (a) Quality factor and (b) Relative absorption as a function of the distance between resonator and feedline for different coupling lengths of the resonator. For large distances the absorption decreases. The fundamental resonance frequency is analyzed for a lossy sample with $\epsilon_l = 24$.

6.2.2. Performance

With the functionality ensured, the performance of the distant flip-chip model must be investigated. The distance and the coupling length are of major importance since both parameters define the coupling of the microwave signal in the resonator. The simulations which were used to investigate functionality are employed. Since the performance is under review, the model is changed to lossy dielectrics, whereas the conducting parts remain perfectly electric conducting (corresponding to a superconductor below its critical temperature). The Al_2O_3 is made lossy with a predefined entry from the material library of *CST Microwave Studio* while the sample is created with $\epsilon_l = 24$ and a loss tangent of $\tan\delta = 10^{-5}$. Only the fundamental resonance frequency is studied. The performance is evaluated by the quality factor (cf. equation (2.12)) which is calculated by the obtained resonance frequency and FWHM of the resonance dip. Moreover, the relative absorption is treated, which is defined

as the difference of the maximum transmitted signal and the amplitude at the resonance: $\max(S_{21}) - S_{21}(\nu_1)$. This quantity is schematically depicted in figure 6.4.
In figure 6.4(a) the obtained quality factor is displayed as a function of the distance of the resonator chip. The quality factor increases with rising distance, this is because the coupling of the microwave signal decreases with increasing distance. Generally, the quality factor describes the ratio of stored energy in the resonator and dissipated power. If the coupling into the resonator decreases, the probability of decoupled photons decreases, resulting in an attenuated power loss due to the dissipation of photons and the quality factor increases. The resonator becomes less damped with a higher quality factor. In addition, the impact of the coupling length is depicted in figure 6.4(a). For an increasing length of the coupling arm, the coupling into the resonator increases, which reduces the quality factor. This is in agreement with the above given explanation. Further decreasing of the coupling length would enhance the performance but at the cost of the coupled signal into the resonator. This can be quantitatively described with the relative absorption, which is depicted in figure 6.4(b). For increasing distances the absorption increases before again decreasing for even larger distances. This leads to a maximum of the absorption. For longer coupling lengths, the absorption in the resonator increases which makes sense since the coupling increases. However, with coupling arms smaller than the displayed ones, the absorption decreases rapidly even for smaller distances.
As a result, the performance of the distant flip-chip requires a trade-off between good coupling (absorption) and high quality factors. With the distance and the coupling length, this coupling into the resonator can be manipulated. The investigated set of coupling lengths ($l_\mathrm{c} = \{500, 600, 700, 800\}\,\mu\mathrm{m}$) provides a good compromise with quality factors of several thousand and at the same time a high absorption into the resonator to even see a signal. This is valid for distances up to 100 µm, making it a challenge to set the distance in the experiment within this range.

6.3. Experimental preparations

The chosen substrate material is Al_2O_3, due to its convenient use and the low dielectric losses and permittivity as already mentioned. To transmit as much microwave signal as possible the impedance of the coplanar feedline is adjusted to the 50 Ω of the microwave connectors. With the center conductor width S and a gap width W the ratio of $S/W = 2.4$ has to be fulfilled, since the substrate is Al_2O_3. Therefore, only a slight fraction of the signal should be reflected at the connection between feedline and microwave connectors at the resonator box. To measure the dielectric properties of the sample the deposited CPW $\lambda/4$-resonator must be excited, which is achieved by an inductive coupling of the closed end. Therefore, the coupling arm with length l_c must be precisely aligned over the central conductor to ensure best coupling of the signal into the resonator as depicted in the inset of figure 6.1. Moreover, the distance of the sample h influences the coupling into the resonator, which was investigated within the simulations above. Since the permittivity of the bulk sample under test is usually unknown, the impedance cannot be adjusted. The geometrical parameters S, W are fixed and so is the impedance. However, to ensure a good coupling into the resonator and a sufficient

penetration of the electric field both parameters S and W are chosen to be relatively large. When the resonance condition (equation (2.10)) is met, resonance dips occur in the spectrum and the permittivity of the sample can be analyzed. Since the resonator is fabricated directly on the sample, the cavity perturbation theory cannot be applied. The dielectric properties are not obtained by analyzing the frequency shift between an unloaded and loaded cavity, but only by the resonance frequency of the resonator. The effective dielectric constant is then obtained with rearranging equation (2.10)

$$\epsilon_{\text{eff}} = \left(\frac{nc}{4l\nu_n}\right)^2 , \tag{6.2}$$

and the permittivity of the sample is calculated utilizing the conformal mapping technique for. Note that within this analysis the sample acts as a substrate and the distance between sample and feedline and the substrate of the feedline are treated as additional dielectric layers. The meander-shaped length of the resonator must be renowned, since it directly influences equation (6.2). The fundamental ($n = 1$) as well as higher harmonic modes (only odd multiples: $n = 3, 5, ...$) can be excited giving access to the permittivity for several discrete frequencies.

6.3.1. Resonator fabrication

Based on the knowledge gained with the simulations, masks are designed which can be used for optical lithography. For the feedline a mask is shaped as depicted in figure 6.1 with a center conductor width $S = 300\,\mu\text{m}$ and a gap width of $W = 120\,\mu\text{m}$. The feedline is patterned on a Al_2O_3 substrate of height $h_s = 430\,\mu\text{m}$ with a lift-off process. In this additive technique a photoresist (sacrificial material) is structured firstly on the Al_2O_3. After that copper (target material) is deposited completely over the substrate. In a final step the photoresist is washed out together with the copper on its surface and the desired conductive structure remains. The deposited copper has a thickness of around $t = 600\,\text{nm}$. This feedline is used for all measurements since the separation of resonator and transmission line within the distant flip-chip method.
Since the resonator is shaped out of the superconductor Nb, several different masks are designed. The center conductor width and the gap width are chosen to be $S = 120\,\mu\text{m}$ and a gap width of $W = 50\,\mu\text{m}$ for all resonators. Three different lengths are shaped in a meander pattern with an example shown in figure 6.1 with coupling lengths $l_c = \{500, 600, 700, 800\}\,\mu\text{m}$. Bulk dielectric materials are selected for establishing the method: The chosen samples are TiO_2, MgO and LAO, all with rectangular shape of around 5 mm side length and heights between 300 and 500 µm. A list with the relevant parameters can be found in the appendix in table A.3. The investigated samples are in a first step completely sputtered with Nb with a thickness of around $t = 300\,\text{nm}$. The Nb films are characterized in the SQUID with an exemplary shown in the appendix. After that the resonator is structured with an etching procedure. Within this subtracting technique the wanted pattern is achieved by covering the Nb with a photoresist. The mask is then placed over the sample and the whole setup is exposed to UV light. In the etching process the conductive parts which were shielded by the mask remain. Three resonators of different length are patterned on each material, leading to

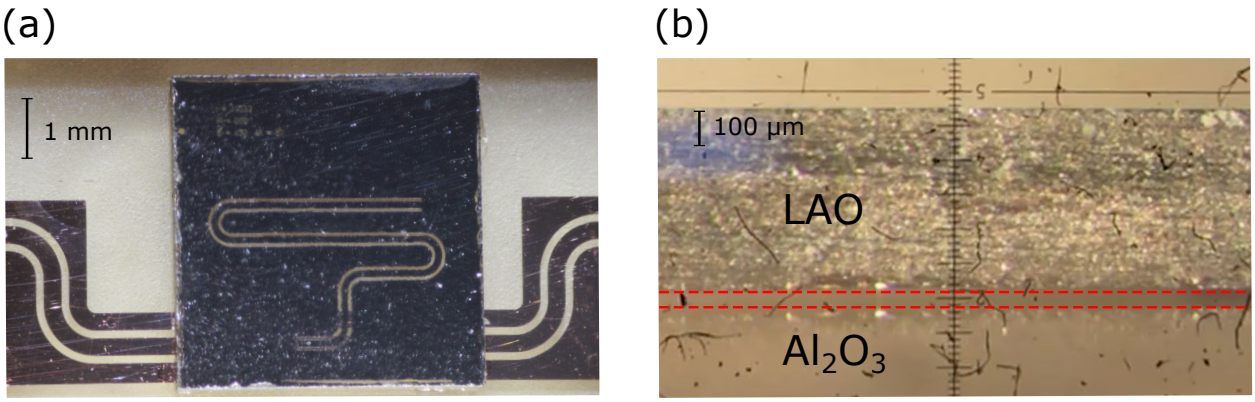

Fig. 6.5.: (a) Top view of a real distant-flip chip model. The coupling arm of the resonator is centrally aligned over the feedline, which can be observed by the transparent character of the sample. (b) Optical micrograph of a flipped chip over a Al_2O_3 substrate. The distance is obtained by the reflection of the sample in the Al_2O_3 marked with red dashed bar.

nine structured resonator chips on the bulk materials.
All optical lithography process, the lift-off as well as the etching and the Nb sputtering are executed by the 4th Physics Institute of the University of Stuttgart.

6.3.2. Chip mounting

Due to the design of the distant flip-chip model, resonator and feedline substrate are separated. This makes the mounting of the resonator chip a pivotal task for a successful measurement. An advantage of this design is the reusability of the feedline. After putting the substrate with feedline into a suited brass resonator box, it needs to be connected to the microwave connectors. Subsequently, the substrate can be used for several resonator chips on different bulk dielectrics. However, each chip must be mounted again in a reproducible manner. Especially two issues are of major interest: the exact placement of the coupling arm over the center conductor of the feedline and the distance of the chip over the feedline.
In figure 6.5(a) a top view of an exemplary flip-chip model is displayed. The used bulk dielectric is transparent, so the resonant structure can be observed despite the flipped sample. Moreover, in the gaps of the resonator the underlying feedline and substrate is visible through the sample, which makes it comparably simple to adjust the coupling arm centrally over the center conductor of the feedline. To set a certain distance of the chip over the feedline and prevent a short, a small amount of vacuum grease is attached at the corners of the flipped chip and then placed over the feedline. In figure 6.5(b) a side view of a placed chip is displayed observed through a microscope. With the reflective surface of the Al_2O_3, the distance between sample and feedline can be well estimated and is found to be $h \approx 40\,\mu m$. Since for each chip a comparable amount of grease was used, this distance holds for all measurements where grease was attached at the corners. After aligning, the placement of the

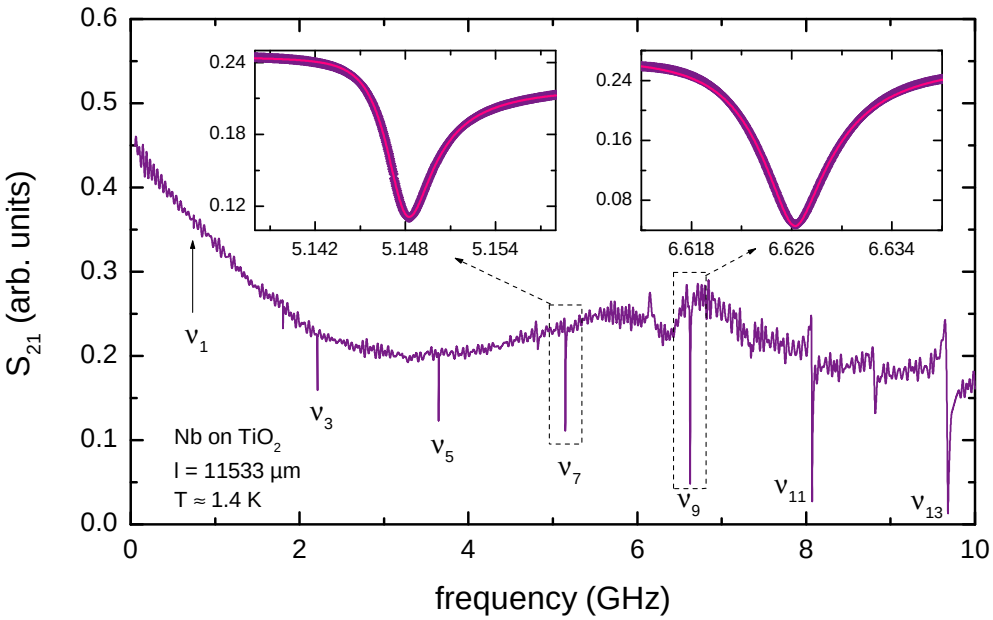

Fig. 6.6.: Transmission spectrum of a resonator chip with $l = 11\,533\,\mu m$ deposited on a TiO_2 sample up to 10 GHz. The insets show two respective dips with higher resolution and the according Lorentzian fits.

sample is fixed with Fixogum. This guarantees a constant placement and distance of the chip during the measurement time.

6.4. Experiments

Since the distant flip chip is successfully simulated, the next step is to measure the above introduced samples. This section firstly gives insight in the general temperature-dependent measuring procedure, including a necessary correction of the results for the influence of the Nb. Afterwards, the results of the three investigated dielectric materials are presented, especially the obtained permittivities and quality factors.

6.4.1. Temperature-dependent measurements

After mounting each respective resonator chip over the feedline, the resonator box is mounted inside the sample chamber of the VTI and cooled down. The transmission spectrum is obtained for the lowest possible temperature at around $T \approx 1.4$ K. The according resonance dips are identified and each resonance is observed with a higher resolution.
In figure 6.6 an exemplary spectrum up to 10 GHz is displayed. The resonance dips can be clearly identified. For higher frequencies unwanted parasitic resonances become more pronounced and make it impossible to identify the absorption dips of the resonator. The number of possible discrete resonances depends strongly on the permittivity of the studied sample (see equation (2.10)). TiO_2 has a high dielectric constant, and therefore the

fundamental frequency is lower and more harmonics can be observed. MgO with a small permittivity has a relatively high fundamental frequency and only a few harmonics can be observed. Thus, three resonator lengths are fabricated. Generally, for higher frequencies unwanted resonances become more pronounced and complicate the correct identification of the resonance dips. In addition, the microwave signal decreases for increasing frequencies, which also makes it difficult to see higher harmonics. Within the experiments, resonance frequencies up to 20 GHz and the 19th mode could be observed, depending on the investigated material and chosen resonator. Afterwards, the identified dips are obtained in 0.2 K steps up to 9 K. For the further analysis the resonance dips are fitted with a Lorentzian function, as depicted in the insets in figure 6.6, which directly yields resonance frequency and FWHM.

6.4.2. Analysis and superconductor correction

Due to measuring at different temperatures, two effects must be considered. The temperature-dependent change of the dielectric constant of the sample as well as the superconducting properties of the Nb, which shapes the resonator. While the temperature-dependent permittivity is of interest and states information about the dielectric properties of the sample, the superconducting impact is unwanted and needs to be corrected for. All investigated sample have temperature-independent permittivity at low temperatures (see chapter 4.2.2), and thus the measured resonance frequencies should not shift. This is because the effective dielectric constant does not change and it holds $\nu_n \propto \frac{1}{\sqrt{\epsilon_{\text{eff}}}}$.
However, the superconducting properties of the Nb change for different temperatures. This is considered with the London equations, which give an expression for the so called London penetration depth [92]. The penetration depth is temperature-dependent, slightly increases with increasing temperature and diverges by approaching T_c. For temperatures close to the transition temperature it can be described with an empirical equation [93]. The temperature-dependent penetration depth is assumed to change the impedance of the CPW [94]. The impedance is related to the resonance frequency of the resonator via the effective dielectric constant, thus a frequency shift occurs. With increasing temperatures, the penetration depth increases resulting in a resonance shift to lower frequencies. Above the critical temperature the Nb turns to its non-superconducting state with high resistivity. This results in the disappearance of the resonance dips. The frequency shift holds for the fundamental and harmonic modes and can be described with

$$\nu = \frac{\nu_{n,0}}{\sqrt{1 + \frac{\Gamma}{2Z_0} \frac{\lambda_0}{\sqrt{1-\left(\frac{T}{T_c}\right)^4}}}}\,, \tag{6.3}$$

with the shifted resonance frequency ν, the resonance frequency of the unperturbed CPW $\nu_{n,0}$ for $T = 0$, a geometrical factor Γ, the characteristic impedance Z_0 and penetration depth λ_0 at $T = 0$ and the critical temperature of the superconductor T_c. However, this equation is only applicable at temperatures close to T_c
When measuring the resonator chips at increasing temperatures, only a shift to lower frequencies is expected. This is assigned to the Nb, whereas the dielectric samples have no temperature-dependent permittivities.

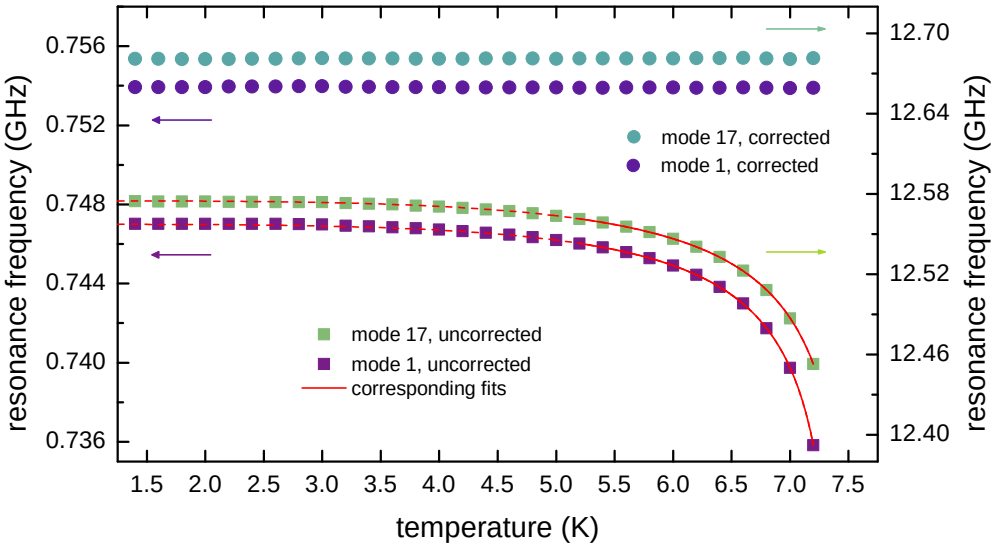

Fig. 6.7.: Resonance frequencies of the fundamental and $n = 17$ mode for temperatures up to $T = 7.2$ K of a resonator chip on TiO_2. Displayed are the uncorrected resonance frequencies, where the temperature-dependent penetration depth causes a shift and the corrected resonance frequencies with the effects of the superconductor subtracted. For temperatures close to T_c, equation (6.3) is applicable and can describe the frequency shift due to the change of the impedance.

In figure 6.7 the obtained resonance frequencies of the temperature-dependent measurements of a resonator chip on TiO_2 are displayed. Here, the fundamental mode as well as the highest observed harmonic are shown. In the lower part of the figure the uncorrected resonance frequencies can be seen. They remain constant for increasing temperatures before shifting to lower temperatures when approaching T_c. Since the permittivity of TiO_2 is temperature-independent within this range, the shift is due to the impedance change originating from the penetration depth of the Nb. To correct for this shift, equation (6.3) is fitted to the data. Whereas Z_0 and Γ are fixed and $\nu_{n,0}$, λ_0 and T_c are obtained from the fitting. The data are fitted for temperatures close to T_c, indicated with the full line in figure 6.7. With the fitting procedure, the unperturbed resonance frequency at $T = 0$ is obtained, however, the resonance frequencies for the measured temperatures are of interest. To correct for this shift, the data from the fit at the respective temperatures are investigated and it is determined how much the penetration depth decreases the resonance frequency at that certain temperature. Subsequently, the measured data points are calculated backwards with this correction factor. In figure 6.7 the corrected resonance frequencies are depicted in the upper part. For both modes these values are more or less constant for the measured temperatures as expected. Additionally, the corrected values are at higher frequencies which is in agreement with the shift to lower frequencies due to the penetration depth of the Nb. With these resonance frequencies, the effective dielectric constant and the desired permittivity of the sample can be easily calculated. This is done for each sample separately in the following sections. The quality factors obtained for each chip are calculated with the uncorrected resonance frequencies since

Tab. 6.2.: Critical temperature and penetration depth at $T = 0$ for the Nb resonators on the respective dielectric obtained with fits according to equation (6.3). The values are averaged for all according fits and the appropriate statistical errors are displayed.

	T_c (K)	ΔT_c (K)	λ_0 (nm)	$\Delta\lambda_0$ (nm)
TiO_2	7.50	0.12	718.63	137.71
MgO	8.15	0.03	439.09	53.84
LAO	6.91	0.38	784.26	169.62

the Nb is temperature-dependent and the change of the quality factors is of interest. Furthermore, T_c and λ_0 stating information about the Nb are obtained within the fit. In table 6.2 are the superconducting parameters for the Nb on the three used dielectrics displayed. The parameters are averaged for each material, since the bulk was sputtered first and afterwards cut and structured. It is assumed that the quality of the Nb film changes for different substrate materials. The Nb on the LAO has the lowest T_c but highest λ_0 for $T = 0$. Generally, all obtained critical temperatures are below the literature value of 9.2 K for bulk Nb, but this is typical for such thin films and was previously observed [25, 79]. The obtained values for the penetration depth are relatively large compared to the literature value of $\lambda(T = 0) = 39\,\text{nm}$ [55], however they are in agreement with preliminary studies [25, 79]. This large deviation may originate from approximate nature of the fit, as well as from a not completely pure Nb. Nevertheless, the trend in table 6.2 that for increasing T_c the penetration depth decreases is in good agreement with earlier studies [95].

6.4.3. TiO_2

TiO_2 has anisotropic dielectric properties, therefore, the crystal direction of the samples are important. The samples are cut in the (100)-plane, meaning the Nb is sputtered on that surface. The meander structure of the resonator is either parallel to the a-axis or parallel to the c-axis, which have different permittivities. Since TiO_2 has a tetragonal unit cell, the axis corresponding to the height of the bulk sample is also the a-axis. The two shorter resonators ($l_1 = 11\,533\,\mu\text{m}$, $l_2 = 15\,644\,\mu\text{m}$) have their meander structure parallel to the a-axis, while the longest ($l_3 = 19\,755\,\mu\text{m}$) has it parallel to the c-axis. Each resonator has a coupling arm with length $l_c = 800\,\mu\text{m}$ and the distance between feedline and resonator is $h = 40\,\mu\text{m}$ for each respective chip.
Figure 6.8 shows the determined permittivities for each TiO_2 resonator. The dielectric constants are calculated with equation (6.2) after the resonance frequencies are corrected for the shift due to the penetration depth of the superconducting Nb. An additional temperature dependence could not be observed. Some harmonic modes vanish in the background earlier than others and could not be fitted, this is the reason why not all observed modes end at the same temperature. It is only possible to analyze the TiO_2 resonator up to around 10 GHz since for higher frequencies the desired resonance dips could not be identified.

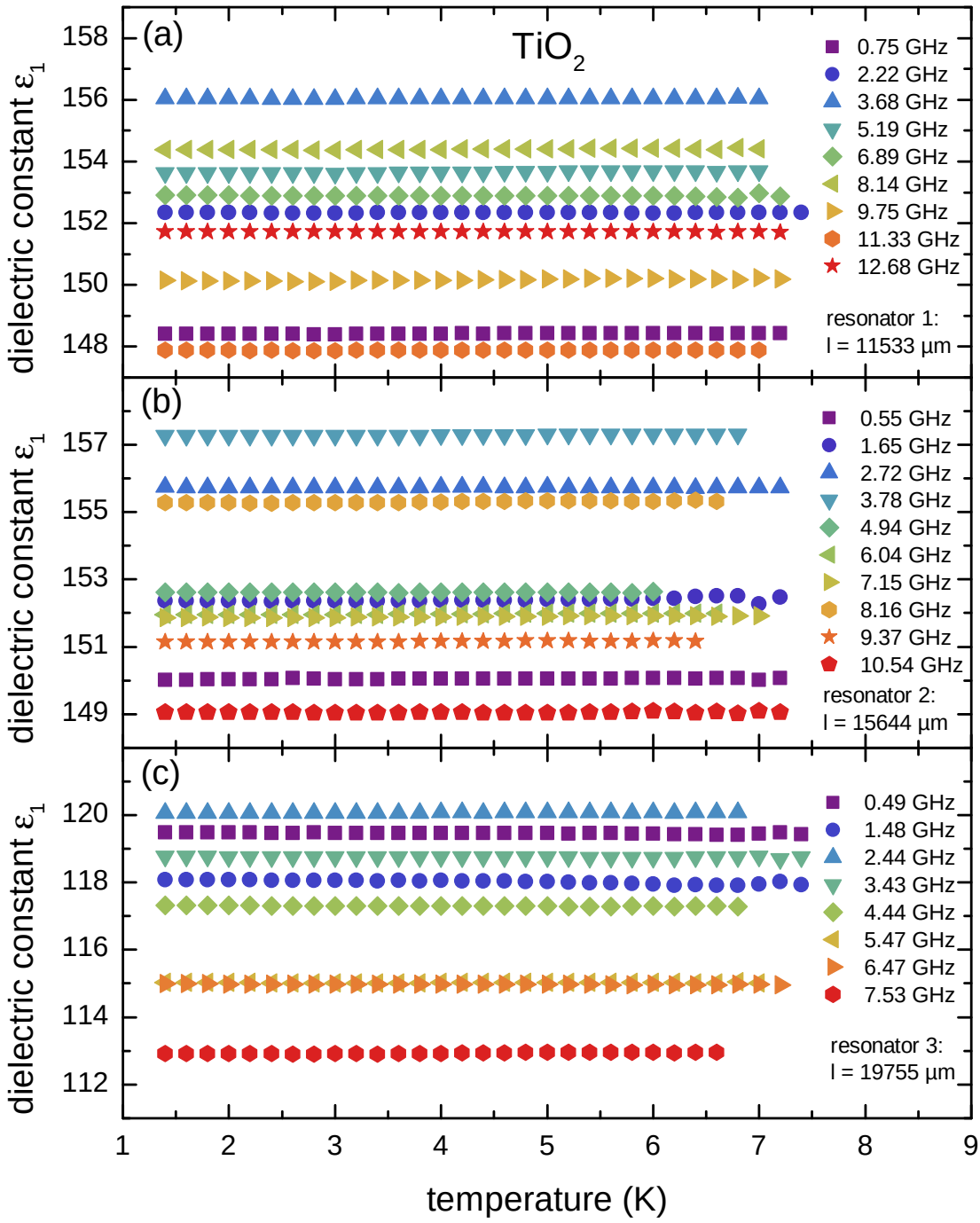

Fig. 6.8.: Dielectric constants as a function of the temperature for the three measured TiO_2 resonator chips. For each chip all observed and evaluable modes are displayed.

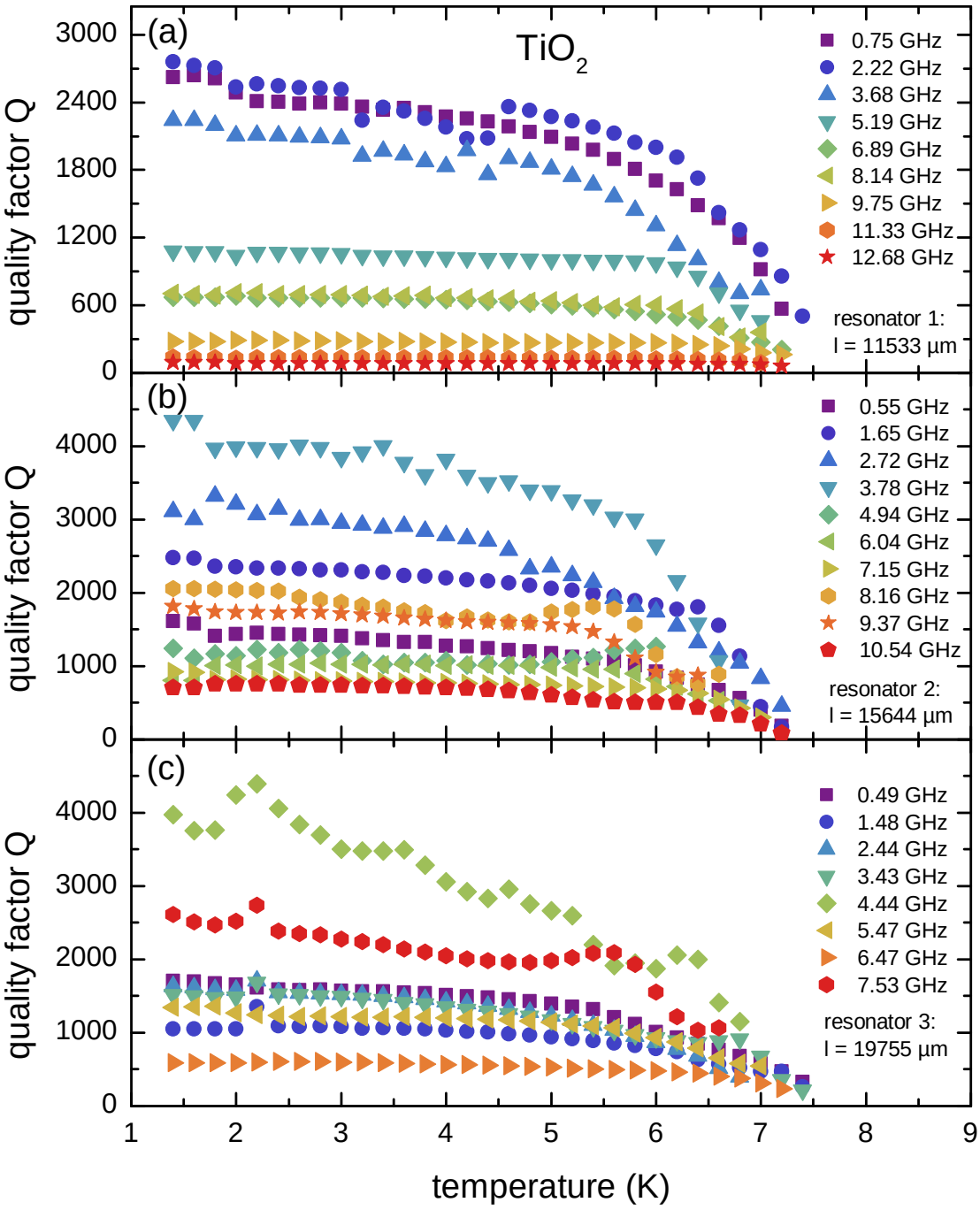

Fig. 6.9.: Quality factors as a function of the temperature for the three measured TiO_2 resonator chips. For each chip all observed and evaluable modes are displayed.

In figure 6.8(a) and (b) the obtained permittivities range between 148 and 157 for both resonators, while in (c) the dielectric constants range between 113 and 120. This is due to the different orientations of the resonators. The literature values of the a-axis and c-axis are around $\epsilon_{1,a} = 130$ and $\epsilon_{1,a} = 250$. The permittivity of the the a-axis dominates, since this axis corresponds to the thickness of the sample. For the shorter resonators the effective dielectric constants increases due to the orientation parallel to the in plane a-axis and the displayed values are obtained. For the longest resonator this is not the case due to the orientation parallel to the in plane c-axis and the dielectric constants are smaller. For all three resonator chips an error must be estimated, which will be discussed in the upcoming section. Additionally, for all resonators the permittivities for the higher harmonics spread around the dielectric constant of the fundamental mode. Since TiO_2 is not frequency-dependent regarding dielectric properties in this microwave regime, this distribution is attributed to the uncertainties of the distant flip-chip model.
To define the resonator characteristics, the Nb must be discussed. As already mentioned the critical temperature and the penetration depth are obtained with the fit for the frequency correction and are depicted in table 6.2. To further characterize the resonator, the quality factor is studied. In figure 6.9 the obtained quality factors for the resonators on TiO_2 are displayed. For all resonators the behavior is the same: Q decreases with increasing temperatures until it it vanishes at T_c. This is an expected behavior for superconducting microwave resonators. Furthermore, there is kind of a plateau at low temperatures where the maximum quality factor is limited by attenuation in the resonator, by conductor and dielectric loss [25]. By increasing the frequency a decrease in Q can be observed, as depicted in figure 6.9(a). For the shortest resonator, the maximum Q is around 3000, which indicates a smaller distance between chip and feedline as for the two longer resonators with maximum Q of around 4000. The strong influence of the distance was already mentioned in the performance simulations and will be discussed hereinafter.

6.4.4. MgO

In the fabrication of the MgO resonator chips some difficulties occurred. After sputtering the whole bulk dielectric and cutting it in the desired pieces, the Nb layer peeled off. The whole procedure was then repeated but only one cut sample could be structured with a resonator. For the other ones the Nb did not stick during the etching of the resonator. Only a resonator with length $l_1 = 11\,533\,\mu m$ and a coupling arm of length $l_c = 800\,\mu m$ at distance of $40\,\mu m$ could be measured. MgO has an isotropic dielectric constant.
In figure 6.10(a) the results for the dielectric constant are displayed. Since the permittivity of MgO is around 10, the fundamental resonance frequency for the measured length is at around 2.44 GHz. Since odd multiples occur, only four resonance dips up to 20 GHz can be identified. Additionally, the $n = 5$ mode could not be observed in the spectrum. The permittivities range between 7.5 and 9.5 for the three frequencies and show no temperature dependence. Note, that the effects of the superconducting Nb are already corrected. In table 6.2 the averaged superconducting parameters are displayed.
In figure 6.10(b) the quality factors for the resonator on MgO are depicted. The behavior is as mentioned above: Q decreases with increasing temperature and vanishes at the transition

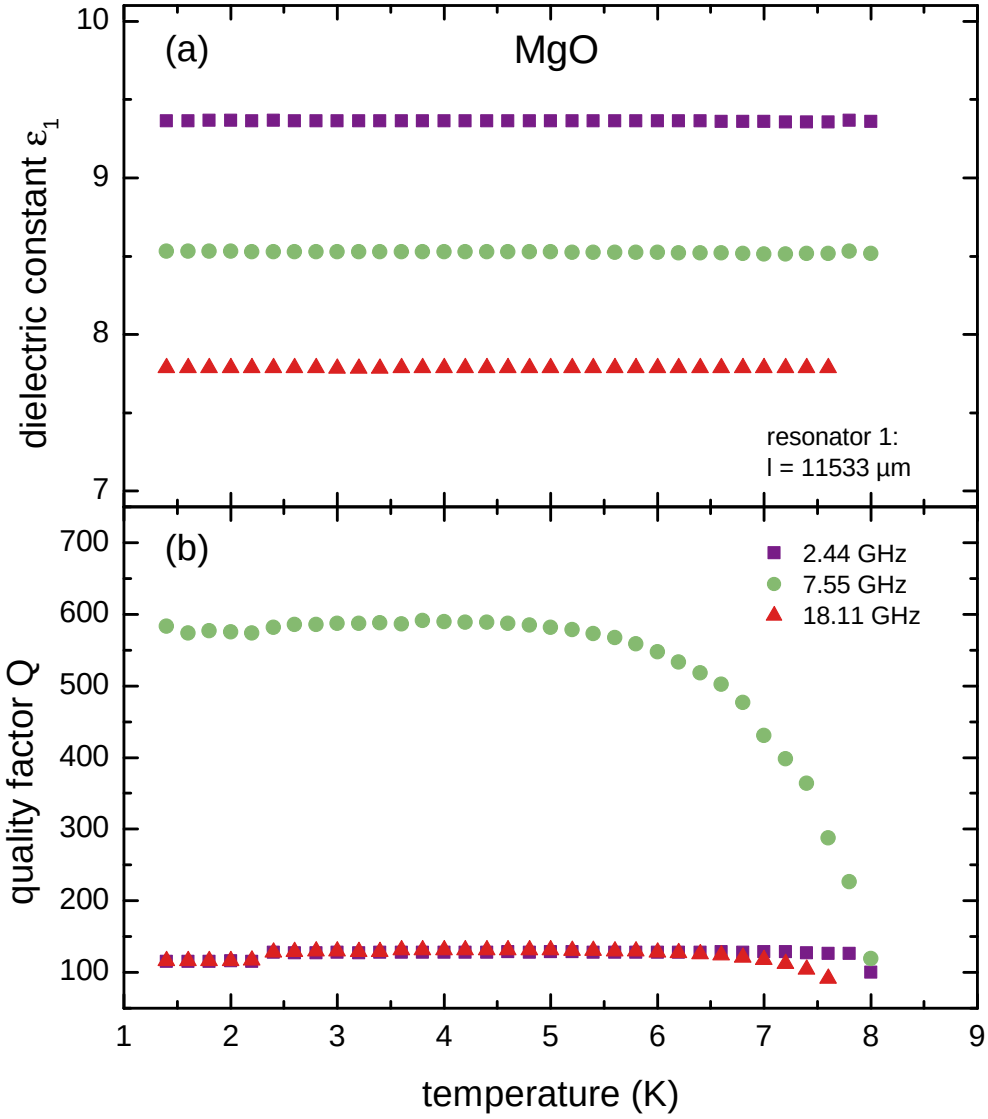

Fig. 6.10.: (a) Dielectric constants and quality factor (b) as a function of the temperature for the one MgO resonator chips. All observed and evaluable modes are displayed.

temperature. Furthermore, there is the plateau for low temperatures indicating the limitation of the maximum Q. The maximum Q of around 600 is much lower as for the quality factors of the resonator on TiO_2, this may origin from the imaginary part of the complex permittivity of MgO..

6.4.5. LAO

LAO has an isotropic dielectric constant, which makes the orientation of the sputtered crystal plane not important. All three resonator chips have a coupling arm of length $l_c = 500\,\mu m$. The two longer resonators ($l_2 = 15\,344\,\mu m$, $l_3 = 19\,455\,\mu m$) are mounted at the mentioned distance of $h = 40\,\mu m$. For the shortest resonator ($l_1 = 11\,233\,\mu m$) a larger amount of vacuum grease was used for the mounting, setting the distance to around $100\,\mu m$.
In figure 6.11 the obtained dielectric constants are displayed. For all chips the results are temperature-independent after correcting for the superconducting penetration depth. The literature value of the permittivity of LAO is 24, which is in good agreement with the values obtained with all resonator chips. The discrete frequencies are measured up to 20 GHz, however some harmonics could not be analyzed. Either they are not visible in the spectrum or they cannot be fitted with a complex Lorentzian function. In figure 6.11(a) the $n = 7$ mode is missing, in (b) the $n = 7, 9, 15$ modes are missing and in (c) the $n = 11, 15$ modes are missing. Moreover, in (a) the $n = 5, 11$ mode vanish for temperatures not close to T_c, which is attributed to the larger distance and a worse absorption for these modes.
The transition temperature and penetration depth of the Nb is depicted in table 6.2. Again, these values are averaged over all fits for the LAO resonators and the statistical error is obtained.
In figure 6.12 the obtained quality factors for the resonators on LAO are displayed. The behavior is similar to the resonators on TiO_2 and MgO: a decrease of Q for increasing temperature with vanishing above T_c. Furthermore, a plateau for low temperatures is visible. While the maximum value of the two longer resonators at a distance of $40\,\mu m$ is at around 4000, the shortest resonator has a maximum Q of almost 15000. This is assigned to the distance of $100\,\mu m$ of this resonator chip. Besides, the influence of the distance for the accuracy and an error estimation are investigated.

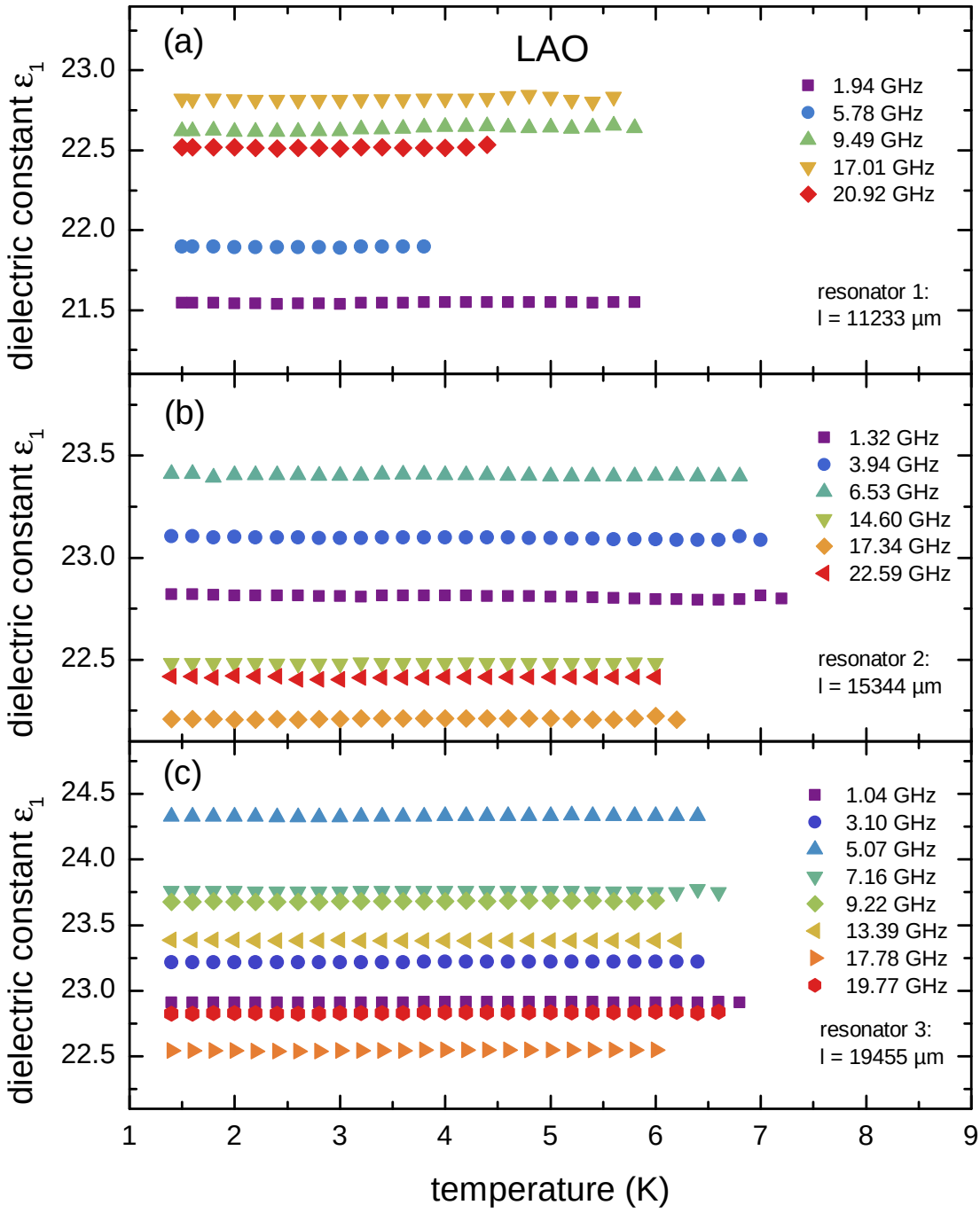

Fig. 6.11.: Dielectric constants as a function of the temperature for the three measured LAO resonator chips. For each chip all observed and evaluable modes are displayed.

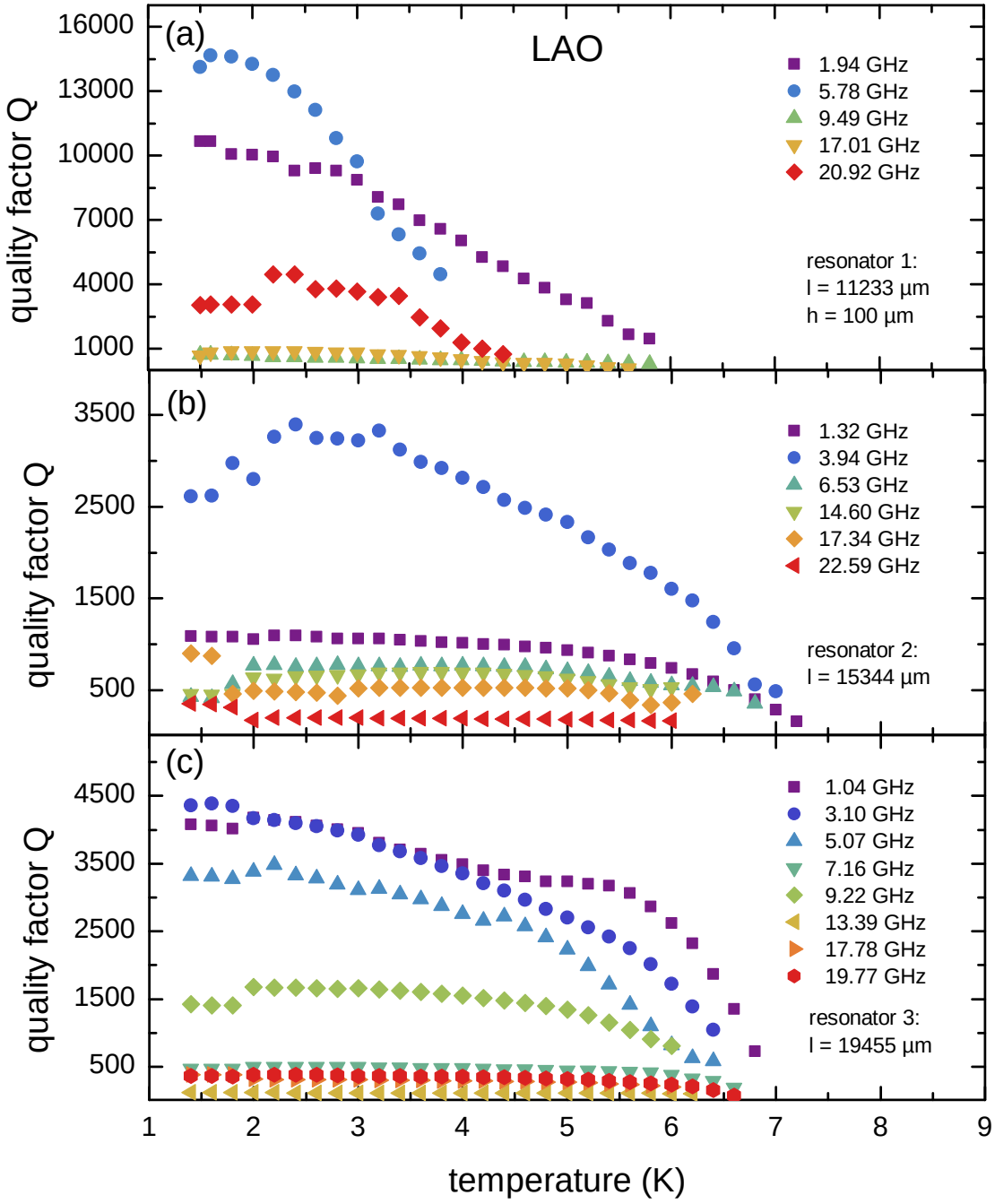

Fig. 6.12.: Quality factors as a function of the temperature for the three measured LAO resonator chips. For each chip all observed and evaluable modes are displayed. The chip with resonator 1 is at a distance of 100 µm, whereas the other two resonator chips are at a distance of 40 µm.

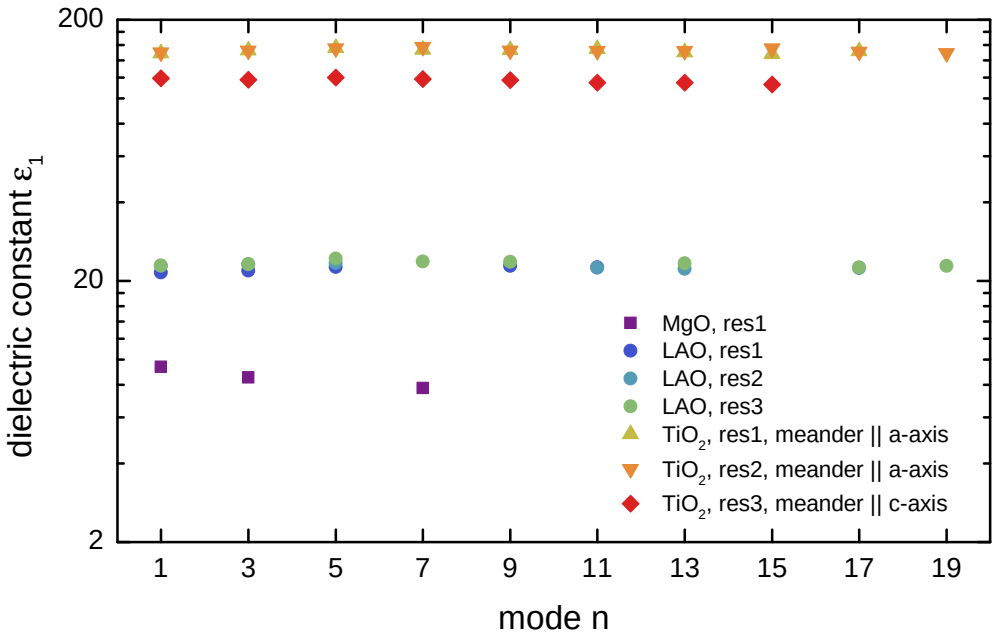

Fig. 6.13.: Dielectric constants for the investigated samples with respective resonators corresponding to the fundamental or harmonic mode. The permittivities are averaged over the measured temperatures. Depending on the dielectric constant the mode numbers range up to 20 GHz

6.5. Discussion

The possible use of the introduced distant flip-chip model for measuring bulk dielectrics was investigated. As suggested by the simulations, the functionality could be confirmed in the experiments. The expected resonance dips could be analyzed and after a correction for superconducting effects, the dielectric constant of the bulk sample could be determined. In the previous sections the temperature-dependent permittivities of each sample was obtained and no change in the range from 1.4 K up to 8 K was found. This is in good agreement with the literature, predicting an independent temperature behavior within this range for the investigated samples. To summarize all dielectric constants, the obtained values are averaged over temperature and plotted against the mode number corresponding to each resonance frequency. This is depicted in figure 6.13.
Since averaged over this temperature, a statistical error can be stated. Due to the temperature independent behavior, the permittivities change only slightly. This must be done for every data point in 6.13, however, the error bars are not shown since they are too small. The maximum statistical error of all was found to be around $\Delta\epsilon_1^{\max,\,\mathrm{T}} \approx 0.05$, which is negligible and confirms the expected independence for the measured temperatures. In the literature it is also stated that the measured materials are frequency independent for these temperatures and the measured microwave range. This can be seen additionally above, however, there is some variation for fundamental and higher harmonic modes. The calculated permittivities depend directly on the resonance frequency for each mode (cf. equation (6.2)), therefore this

fluctuation is attributed to the position of the absorption dip. In the theory, higher harmonics should have exactly the threefold, fivefold, etc. resonance frequency corresponding to the nth harmonic mode. This is not always the case in the experiment and will be discussed within an error estimation. Nevertheless the distant flip-chip model is well suited to measure bulk dielectrics in a range of several 100 µm. The thickness of the sample can be variously chosen, since the CPW resonator is directly deposited on the sample. Requirements regarding the thickness and sample material are stability to not break the sample during the sputtering process of the resonator material. In addition, the material should have a simple preparation, since a polished and clean surface is required for the sputtering. Moreover, the resonator parameters S, W need to be adjusted to ensure a sufficient electrical field distribution in the sample.
Maximum quality factors of the resonators up to 4000 for a distance of 40 µm could be achieved, however this heavily depends on the mounting of the chip over the feedline. Additionally, effects of coupling into the resonator, losses, tilted or decentralized resonator chips change the magnitude of Q, which prevents the comparison of the quality factors among the different resonators. For increasing temperatures Q decreases and vanishes after approaching T_c, which is expected for superconducting microwave resonators. For low temperatures a plateau can be identified which is due to limitation of the maximum Q by attenuation. Generally, for higher harmonic modes the quality factor decreases, however, for some measurements higher harmonics have higher Q.

Impact of distance and position of the resonator chip

As already mentioned, the distance of the resonator chip is a crucial parameter for the distant flip-chip model. Due to a measurement through a microscope, the distance was found to be $h = 40\,\mu\text{m}$, which is assumed for all measurements. However, a different distance changes the obtained results drastically, which is depicted in figure 6.14.
For the measured and corrected fundamental resonance frequency (averaged over the measured temperatures) the dielectric constant is calculated for different assumed distances by utilizing the conformal mapping technique. For small distances the resulting permittivity changes drastically, whereas the change is rather small for a larger distance when the influence of the Al_2O_3 reduces. In addition, a distance of $h = 40\,\mu\text{m}$ is displayed, this value is assumed for all analyses due to the observations with the microscope. However, two possible errors must be considered: The amount of grease for each mounting and the observation through the microscope itself. For each measurement the mounting was done in the same procedure and a similar amount of grease was used, however this amount cannot be quantified. Furthermore, the distance may be reduced over a larger time due to the own weight of the chip. Moreover, the observation and determination of the distance with the microscope (displayed in figure 6.5(b)) is not exact. With both error sources regarded, an error for the distance of $h = \pm 10\,\mu\text{m}$ is assumed. This leads to an error for the permittivity of $\Delta\epsilon_1^{\text{h}} = \pm 1$. For small permittivities (e.g. MgO) this is a relatively larger error, whereas it is comparably small for larger permittivities (e.g. TiO_2), which can be seen in the inset in figure 6.14.
The distance does not only change the calculated dielectric constant but also the performance of the resonator. Since for increasing distance the coupling into the resonator decreases,

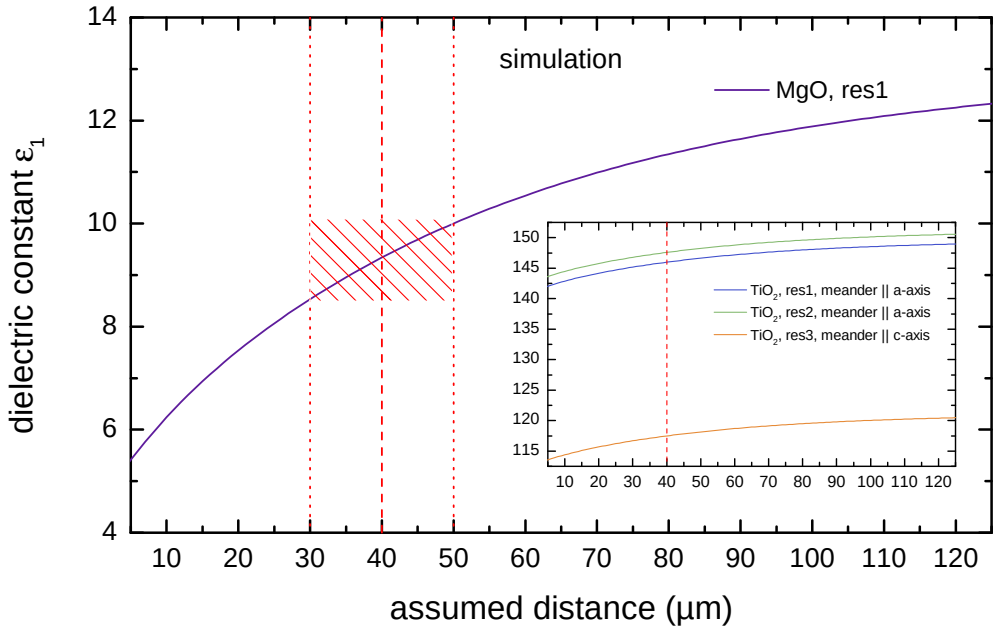

Fig. 6.14.: Dielectric constant for the measured fundamental mode for an assumed distance of the resonator chip on MgO. The distance of 40 µm used in the experiments is displayed. An error range of ±10 µm causes an error of the permittivity of $\Delta\epsilon_1^{\mathrm{h}} = \pm 1$.

the quality factor increases. The assumed distance of 40 µm with expected error of ±10 µm covers the measured quality factors very well, with some being higher or smaller than 4000. For the resonator chip with shortest length on LAO, more grease was used, increasing the distance to approximately 100 µm. This results in the high Q over 10000. For the measured low quality factor of the chip on MgO, another source of error must be studied: the placement of the resonator over the feedline. So far a perfect centrally aligned chip is assumed, however, this may not be completely true within the experiment, despite the alignment due to the transparent samples. While a slightly displaced chip does not change the measured dielectric constant, it has a certain influence on the Q.
Generally, the magnitude of Q depends on different factors. The mentioned mounting, which is different for each used chip and causes deviations, but also intrinsic losses in the dielectric sample as well as in the sputtered Nb. Due to the different external conditions, the quality factors change for each chip.

Error estimation

To give a profound error estimation for the measured dielectric constants, different sources need to be considered.

The permittivity is obtained as a function of the conformal mapping of the effective dielectric constant

$$\epsilon_1 = \mathfrak{F}(\epsilon_{\text{eff}}) = \mathfrak{F}\left(\left(\frac{nc}{4l\nu_n}\right)^2\right) , \tag{6.4}$$

while ϵ_{eff} is calculated directly with the length of the resonator and the measured resonance frequency. A fabrication error of the resonator changes the permittivity, since the length could be slightly different than expected. However, since the resonators are fabricated by the precise etching technique, the length as well as the geometrical parameters S, W are assumed to be exact and are neglected for this estimation.
The resonance frequency is directly related to the effective and therefore desired permittivity. Some different possibilities occur which may change the resonance frequency. Firstly, since the resonator is coupled to the feedline over a gap, an additional small shift between actual and expected resonance frequency occurs due to the gap acting as a series capacitor [44]. An error in the recording can be neglected due to the precise frequency resolution of the VNA. However, the position of the peaks spectrum may be influenced by the presence of the CPW feedline on the Al_2O_3 substrate. The feedline causes not only the excitation of the resonator, but also cross talk effects between feedline and resonator are possible due to the coupling over the separation. In the further analysis an error in the resonance frequency can occur. The error in the fitting with a Lorentzian function is negligible since the resonance dips could be very nicely modeled.
Additionally, the calculation of ϵ_1 from ϵ_{eff} with the conformal mapping technique is responsible for some errors. The treatment of the distance and position of the resonator chip is already discussed above and causes a large relative deviation. Another point is the conductive sheet (feedline) between Al_2O_3 and separation, which is not treated within the conformal mapping technique. This causes an additional slight shift of the calculated dielectric constant.
The substantial difference between the permittivity of fundamental and higher harmonic modes remains unsolved. This may originate from the increase of nodes and antinodes for higher mode numbers of the $\lambda/4$-resonator and a resulting change in the fraction of the electric field inside the dielectric sample. With all above mentioned possible sources of error, a deviation of 10 - 15 % of the obtained permittivities to the literature values seem reasonable.

7. Conclusions and outlook

This project addresses the realization of a new measurement technique to probe bulk dielectric samples for their dielectric properties at GHz frequencies. For that purpose, a new resonant approach was developed. This method utilizes the distant flip-chip mounting where a CPW $\lambda/4$-resonator is coupled inductively over a feedline. The dielectric constant ϵ_1 of the sample under study is accessible by analyzing the resonance frequencies of this geometry.
In a previous step, another resonant measurement technique, which utilizes the cavity perturbation theory, was intensively examined. Within this method, the bulk sample is placed on top of a planar microwave resonator and acts as perturbation. The sample causes a change in the effective dielectric constant and the resulting frequency shift can be analyzed for the desired dielectric properties. This approach was successfully performed in preliminary studies, however, the materials under test were thin films in the nm regime [25]. The acquired knowledge was transferred for bulk dielectric samples under study, but there were challenges to overcome. The electric field distribution inside the sample changes by going from the nm to the µm regime and the surface conditions are different for thin films or bulk samples. With finite element simulations and experiments, planar microwave resonators were tested for their suitability to measure the dielectric properties of an external bulk sample. For that purpose, two different geometries were studied, a CPW $\lambda/4$-resonator and a microstrip $\lambda/2$-resonator. It was found that neither is suitable for dielectric measurements of bulk samples. This is mainly due to the separation between resonator and sample caused by imperfections and roughness at the surfaces. The electric field cannot sufficiently penetrate the sample because of this additional distance.
The above mentioned new developed approach prevents this air gap effect since the resonator is shaped on top of the bulk sample under study. With the distant flip-chip mounting, the resonator is externally excited through the open space between the chip and the underlying feedline substrate. In a first step, this geometry was tested in finite element simulations, showing that the resonance frequencies ν_n match the analytical results obtained with the conformal mapping technique. This agreement was found for substrates of dielectric constants ϵ_1 up to a value of 300, covering a wide range of potential dielectric samples including nano-confined water in single crystals. The simulations enabled a study of the two relevant coupling parameters distance h of the resonator chip to the feedline substrate and the coupling length l_c, which defines the parallel part of the resonator above the feedline, and thus, optimizing the coupling strength of the resonator geometry.
The resonators were realized in experiments using the elemental superconductor Nb on different substrates while the feedline was fabricated using Cu on an Al_2O_3 substrate. The substrates under study were the materials TiO_2, MgO and LAO with dielectric constants ϵ_1 ranging from 10 to around 250. All measurements with the resonator chips reused the same feedline substrate, whereas different lengths of the resonators were fabricated to access

different operating frequencies. Since higher harmonic modes could be measured, it was possible to probe discrete frequencies up to 20 GHz. The experiments could approve the frequency-independent behavior of ϵ_1 for the three measured materials in this frequency range as expected from the literature. It was feasible to perform measurements at different temperatures down to 1.4 K. In the analysis, a correction for the temperature-dependent penetration depth of the superconductor Nb was required. Hereinafter, ϵ_1 showed no temperature dependence in the measured range, which was predicted by the literature. The maximum quality factors of the resonators reach several thousand and decrease with increasing temperature before vanishing at T_c as expected. Furthermore, the absolute values of ϵ_1 for the different dielectric materials are in good agreement with the literature. This makes the developed approach a suited candidate to measure a wide range of ϵ_1 of the samples under study. In addition, the geometry does not restrict the thickness of the studied sample, it is possible to probe bulk dielectrics thicker or thinner than the samples within this project.

In finite element simulations the distant flip-chip geometry was tested and the coupling parameters h and l_c were optimized. To further improve the simulations, the geometry can be tested with a surface impedance model for the for conductive sheet [96]. Before the resonator fabrication this might be helpful to optimize the coupling parameter l_c to increase the quality factor and simultaneously maintain a sufficient coupling.
Besides the coupling length l_c, the distance of the chip to the feedline h controls the coupling strength. Consequently, the quality factor depends on these to parameters. The experimental results strongly depend on the mounting of the resonator chip. The mounting procedure must be improved for a successful and reproducable experiment. In the master project of V. Engl, microwave boxes with removable side walls were developed [81]. These boxes allow experimental access to the resonator chip and feedline substrate from the side. For further experiments, the distance h can be adjusted in a accurate and reliable manner e.g. by using foil with known thickness. Furthermore, the exact placement of the resonator over the feedline can be improved with these boxes.
It was possible to probe dielectric samples with the new approach up to 20 GHz and down to 1.4 K. However, for specific samples under study, measurements at higher temperatures are desired. This requires different conductive materials for the resonator realization. Since Nb is superconducting below 9.2 K, high-temperature conductors can be applied to access higher temperatures. For potential measurements at room temperature, Cu is a suited material to realize the resonators. Additionally, if a specific frequency range within the microwave regime is desired, the resonator length can be adapted. However, this requires knowledge of ϵ_1 of the sample.
The measured samples are frequency- or temperature-independent for the respective frequency and temperature ranges within this project. The results of this thesis pave the way for probing materials with a frequency-or temperature-dependent behavior, e.g. STO or nano-confined water in single crystals. The master thesis of V. Engl utilizes the distant flip-chip geometry to fabricate a resonator on the substrate STO as a realization of an LAO-resonator on the substrate STO to give experimental access to the 2DEG formed in the LAO/STO interface [81]. It is feasible to probe ϵ_1, which is strongly temperature-dependent ranging from 300 at room temperature up to 20000 below 4 K. Another recent research topic is the nano-confined

water in single crystals. The approach developed in this project can be utilized to give experimental access to the dielectric properties of these samples.
The distant flip-chip model can be used for dielectric spectroscopy of bulk materials at GHz frequencies in several potential experiments. It is feasible to probe temperature- and frequency dependent dielectric samples with ϵ_1 ranging up to 20000 or more.

A. Overview of relevant parameters of the measured resonators

Tab. A.1.: List of chosen materials and geometry values of the CPW $\lambda/4$-resonator (cf. chapter 5.1) with external sample on top. The resonator is structured on Al_2O_3.

CPW	material	geometrical parameter	value (µm)
substrate	Al_2O_3	length × width × height	12000 × 10000 × 430
resonator	Nb	S	120
		W	50
		t	0.3
		l	19435
sample	LAO	length x width x height	5000 x 5000 x 500

Tab. A.2.: List of chosen materials and geometry values of the microstrip $\lambda/2$-resonator (cf. chapter 5.2) with external sample on top. The resonator is structured on Al_2O_3 and the sample has a conductive sheet on top.

microstrip	material	geometrical parameter	value (µm)
substrate	Al_2O_3	length x width x height	12000 × 10000 × 430
resonator	Pb	W	400
		g	500
		t	1
		l	7700
sample	LAO	length × width × height	5500 × 7000 × 500Al_2O_3

Tab. A.3.: List of chosen materials and geometry values of the distant flip-chip model (cf. chapter 6.1). The feedline is structured on Al_2O_3 while the resonators are structured on each sample. The total length of each resonator is $l + l_c$.

distant flip-chip	material	geometrical parameter	value (µm)
substrate	Al_2O_3	length × width × height	12000 × 10000 × 430
feedline	Cu	S	300
		W	120
		t	0.3
sample	TiO_2	length × width × height	5000 × 5000 × 300
	MgO	length × width × height	5000 × 5000 × 500
	LAO	length × width × height	5000 × 5000 × 500
resonator 1	Nb	S	120
		W	50
		t	0.3
		l	10733
		l_c	500, 800
resonator 2	Nb	S	120
		W	50
		t	0.3
		l	14844
		l_c	500, 800
resonator 3	Nb	S	120
		W	50
		t	0.3
		l	18955
		l_c	500, 800

B. Characterization of niobium films

The sputtered niobium film on the bulk LAO is characterized with the SQUID magnetometer. To do so, a LAO sample of height $h_s = 500\,\mu m$ with niobium of thickness $t = 300\,nm$ is measured before the resonator is shaped out of the niobium. The result is shown in fig B.1.

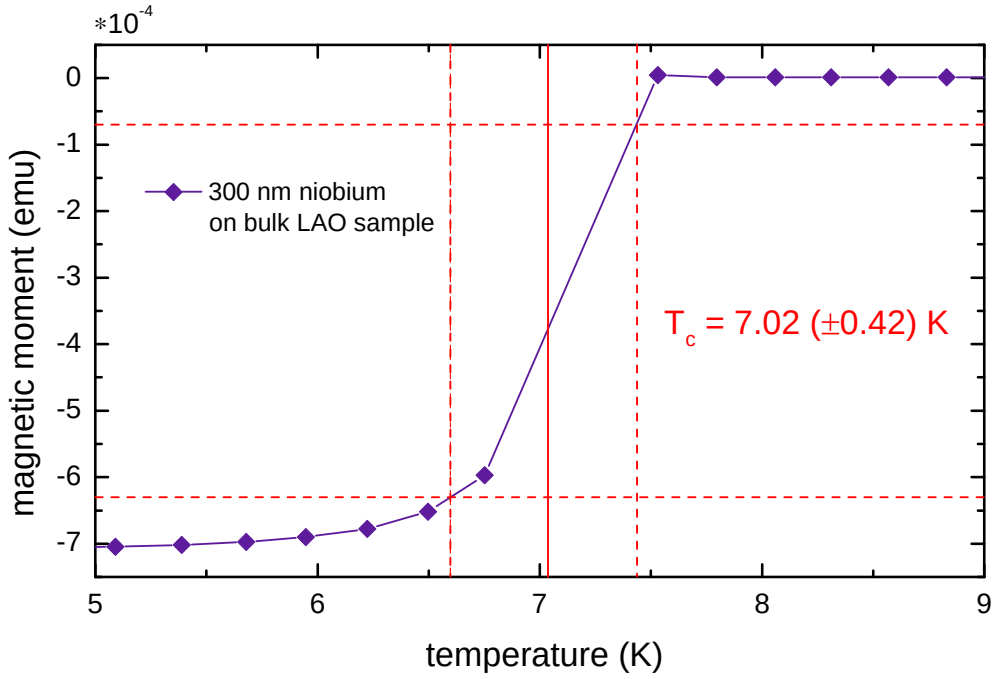

Fig. B.1.: Magnetic moment as a function of temperature of the niobium film on a LAO dielectric. The critical temperature is obtained with the 90/10 method.

Since the superconducting state corresponds to a perfect diamagnet, niobium has a negative magnetic moment below its critical temperature. T_c was characterized with the 90/10 method and is found to be 7.02 K. This value is in good agreement with the critical temperature of the niobium resonators on LAO obtained with the fit in table 6.2.

Acknowledgments

I want to thank various people for their contribution to this project. Especially, I want to thank

- Prof. Dr. Martin Dressel for giving me the opportunity to work on this project.
- Prof. Dr. Jörg Wrachtrup for being my second examiner.
- Dr. Marc Scheffler for being my supervisor and for valuable and constructive suggestions, guidance and discussions.
- Nikolaj Ebensperger for the introduction to the experiments and for helpful discussions.
- Vincent Engl for valuable discussions and a productive collaboration.
- Gabriele Untereiner for sample preparations, assembling and constructive suggestions.
- Monika Ubl and Ahmed Farag for structuring the resonators, coating with copper and sputtering of niobium.
- Mario Zinßer, Alessandro D'Arnese and Christoph Müller for experimental help and constructive discussions.
- Dr. Markus Thiemann, Björn Miksch and Dr. Guilherme Gorgen Lesseux for valuable suggestions and helpful discussions.
- the low temperature department for continuous supply of liquid helium.
- the whole 1. Physikalisches Institut for a pleasant working atmosphere.

References

[1] K. A. Müller and H. Burkard, *Phys. Rev. B* **19**, 3593 (1979).

[2] V. V. Lemanov, *Ferroelectrics* **265**, 1 (2002).

[3] R. Viana, P. Lunkenheimer, J. Hemberger, R. Böhmer, and A. Loidl, *Phys. Rev. B* **50**, 601 (1994).

[4] R. G. Geyer, B. Riddle, J. Krupka, and L. A. Boatner, *J. Appl. Phys.* **97**, 104111 (2005).

[5] A. I. Kolesnikov, L. M. Anovitz, E. Mamontov, A. Podlesnyak, and G. Ehlers, *J. Phys. Chem. B* **118**, 13414 (2014).

[6] B. P. Gorshunov, V. I. Torgashev, E. S. Zhukova, V. G. Thomas, M. A. Belyanchikov, C. Kadlec, F. Kadlec, M. Savinov, T. Ostapchuk, J. Petzelt, J. Prokleska, P. V. Tomas, E. V. Pestrjakov, D. A. Fursenko, G. S. Shakurov, A. S. Prokhorov, V. S. Gorelik, L. S. Kadyrov, V. V. Uskov, R. K. Kremer, and M. Dressel, *Nat. Commun.* **7**, 12842 (2016).

[7] B. Gorshunov, A. Volkov, I. Spektor, A. Prokhorov, A. Mukhin, M. Dressel, S. Uchida, and A. Loidl, *J. Infrared Millim. Terahertz Waves* **26**, 1217 (2005).

[8] O. Klein, S. Donovan, M. Dressel, and G. Grüner, *J. Infrared Millim. Terahertz Waves* **14**, 2423 (1993).

[9] C. H. Townes and A. L. Schawlow, *Microwave Spectroscopy* (Dover Publications, 2013).

[10] M. N. Afsar, J. R. Birch, R. N. Clarke, and G. W. Chantry, *Proc. IEEE* **74**, 183 (1986).

[11] J. Baker-Jarvis, E. J. Vanzura, and W. A. Kissick, *IEEE Trans. Microw. Theory Tech.* **38**, 1096 (1990).

[12] S. Trabelsi and S. O. Nelson, *Meas. Sci. Technol* **14**, 589 (2003).

[13] S. Gabriel, R. W. Lau, and C. Gabriel, *Phys. Med. Biol.* **41**, 2251 (1996).

[14] J. Baker-Jarvis, M. D. Janezic, and D. C. Degroot, *IEEE Instru. Meas. Mag* **13**, 24 (2010).

[15] M. D. Janezic and D. F. Williams, in 1997 IEEE MTT-S International Microwave Symposium Digest, Vol. 3 (1997), pp. 1343–1346.

[16] M. V. Jacob, J. Mazierska, K. Leong, and J. Krupka, *IEEE Trans. Microw. Theory Tech.* **50**, 474 (2002).

[17] G. Kent, in Proceedings of Conference on Precision Electromagnetic Measurements Digest (1994), pp. 352–353.

[18] J. Krupka, D. Cros, M. Aubourg, and P. Guillon, *IEEE Trans. Microw. Theory Tech.* **42**, 56 (1994).

[19] S. Donovan, O. Klein, M. Dressel, K. Holczer, and G. Grüner, *J. Infrared Millim. Terahertz Waves* **14**, 2459 (1993).

[20] M. Javaheri Rahim, T. Lehleiter, D. Bothner, C. Krellner, D. Koelle, R. Kleiner, M. Dressel, and M. Scheffler, *J. Phys. D: Appl. Phys.* **49**, 395501 (2016).

[21] N. G. Ebensperger, M. Thiemann, M. Dressel, and M. Scheffler, *Supercond. Sci. Technol.* **29**, 115004 (2016).

[22] D. S. Rausch, M. Thiemann, M. Dressel, D. Bothner, D. Koelle, R. Kleiner, and M. Scheffler, *J. Phys. D: Appl. Phys.* **51**, 465301 (2018).

[23] M. Scheffler, M. M. Felger, M. Thiemann, D. Hafner, K. Schlegel, M. Dressel, K. S. Ilin, M. Siegel, S. Seiro, C. Geibel, and F. Steglich, *Acta IMEKO* **4**, 47 (2015).

[24] M. Scheffler, K. Schlegel, C. Clauss, D. Hafner, C. Fella, M. Dressel, M. Jourdan, J. Sichelschmidt, C. Krellner, C. Geibel, and F. Steglich, *Phys. Status Solidi B* **250**, 439 (2013).

[25] N. Ebensperger, *Master thesis*, University of Stuttgart (2017).

[26] M. Dressel and G. Grüner, *Electrodynamics of Solids: Optical Properties of Electrons in Matter* (Cambridge University Press, 2002).

[27] D. Bothner, T. Gaber, M. Kemmler, D. Koelle, and R. Kleiner, *Appl. Phys. Lett.* **98**, 102504 (2011).

[28] C. Clauss, M. Dressel, and M. Scheffler, *J. Phys. Conf. Ser.* **592**, 012146 (2015).

[29] A. C. Torrezan, T. P. Mayer Alegre, and G. Medeiros-Ribeiro, *Rev. Sci. Instrum.* **80**, 075111 (2009).

[30] J. J. Henderson, C. M. Ramsey, H. M. Quddusi, and E. del Barco, *Rev. Sci. Instrum.* **79**, 074704 (2008).

[31] M. Scheffler, C. Fella, and M. Dressel, *J. Phys. Conf. Ser.* **400**, 052031 (2012).

[32] M. Thiemann, D. Bothner, D. Koelle, R. Kleiner, M. Dressel, and M. Scheffler, *J. Phys. Conf. Ser.* **568**, 022043 (2014).

[33] Y. Wiemann, J. Simmendinger, C. Clauss, L. Bogani, D. Bothner, D. Koelle, R. Kleiner, M. Dressel, and M. Scheffler, *Appl. Phys. Lett.* **106**, 193505 (2015).

[34] T. Wollandt, M. Thiemann, M. Dressel, and M. Scheffler, *J. Phys. Conf. Ser.* **969**, 012082 (2018).

[35] C. Clauss, D. Bothner, D. Koelle, R. Kleiner, L. Bogani, M. Scheffler, and M. Dressel, *Appl. Phys. Lett.* **102**, 162601 (2013).

[36] W. Voesch, M. Thiemann, D. Bothner, M. Dressel, and M. Scheffler, *Physics Procedia* **75**, 503 (2015).

[37] L. Bondorf, M. Beutel, M. Thiemann, M. Dressel, D. Bothner, J. Sichelschmidt, K. Kliemt, C. Krellner, and M. Scheffler, *Physica B* **536**, 331 (2018).

[38] C. P. Wen, *IEEE Trans. Microw. Theory Tech.* **17**, 1087 (1969).

[39] M. Houdart, in 1976 6th European Microwave Conference (1976), pp. 49–53.

[40] M. Houdart, C. Aury, and A. Jean-Frederic, in 1977 7th European Microwave Conference (1977), pp. 450–454.

[41] R. N. Simons, *Coplanar Waveguide Circuits, Components, and Systems* (Wiley-IEEE Press, 2001).

[42] I. Wolff, *Coplanar Microwave Integrated Circuits* (Aug. 2006).

[43] K. C. Gupta, *Microstrip Lines and Slotlines 2nd Ed.* (Artech House, Inc., 1996).

[44] D. M. Pozar, *Microwave Engineering* (John Wiley & Sons, Inc., 2011).

[45] G. Ghione and C. U. Naldi, *IEEE Trans. Microw. Theory Tech.* **35**, 260 (1987).

[46] S. Gevorgian, L. J. P. Linner, and E. L. Kollberg, *IEEE Trans. Microw. Theory Tech.* **43**, 772 (1995).

[47] M. V. Schneider, *Bell Syst. Tech. J.* **48**, 1421 (1969).

[48] I. J. Bahl and D. K. Trivedi, *A Designer's Guide To Microstrip Line* (May 1977), pp. 174–182.

[49] J. Svacina, *IEEE Trans. Microw. Theory Tech.* **40**, 769 (1992).

[50] H. A. Wheeler, *IEEE Trans. Microw. Theory Tech.* **13**, 172 (1965).

[51] E. Hammerstad and O. Jensen, in 1980 IEEE MTT-S International Microwave Symposium Digest (1980), pp. 407–409.

[52] J. Svacina, *IEEE Microw. Guided Wave Lett.* **2**, 385 (1992).

[53] H. A. Wheeler, *IEEE Trans. Microw. Theory Tech.* **25**, 631 (1977).

[54] A. Darwish, A. Ezzeddine, H. C. Huang, and M. Mah, *IEEE Microw. Guided Wave Lett.* **9**, 447 (1999).

[55] C. Kittel, *Introduction to Solid State Physics* (John Wiley & Sons, Inc., 2005).

[56] G. Brodie, M. Jacob, and P. Farrell, *Microwave and Radio-Frequency Technologies in Agriculture: An Introduction for Agriculturalists and Engineers* (Dec. 2015), pp. 52–75.

[57] J. A. Reedijk, H. C. F. Martens, B. J. G. Smits, and H. B. Brom, *Rev. Sci. Instrum.* **71**, 478 (2000).

[58] D. K. Ghodgaonkar, V. V. Varadan, and V. K. Varadan, *IEEE Trans. Instrum. Meas.* **38**, 789 (1989).

[59] D. K. Ghodgaonkar, V. V. Varadan, and V. K. Varadan, *IEEE Trans. Instrum. Meas.* **39**, 387 (1990).

[60] F. J. F. Gonçalves, A. G. M. Pinto, R. C. Mesquita, E. J. Silva, and A. Brancaccio, *Electronics* **7** (2018).

[61] H. C. F. Martens, J. A. Reedijk, and H. B. Brom, *Rev. Sci. Instrum.* **71**, 473 (2000).

[62] M. El-Rayes and F. T. Ulaby, *IEEE Trans. Geosci. Remote Sens.* **GE-25**, 541 (1987).

[63] W. J. Ellison and J. Moreau, *IEEE Trans. Instrum. Meas.* **57**, 1984 (2008).

[64] J. C. Booth, D. H. Wu, and S. M. Anlage, *Rev. Sci. Instrum.* **65**, 2082 (1994).

[65] M. Scheffler and M. Dressel, *Rev. Sci. Instrum.* **76**, 074702 (2005).

[66] M. D. Janezic and J. Baker-Jarvis, *IEEE Trans. Microw. Theory Tech.* **47**, 2014 (1999).

[67] J. Krupka, K. Derzakowski, A. Abramowicz, M. E. Tobar, and R. G. Geyer, *IEEE Trans. Microw. Theory Tech.* **47**, 752 (1999).

[68] J. Krupka, M. Klinger, M. Kuhn, A. Baryanyak, M. Stiller, J. Hinken, and J. Modelski, *IEEE Trans. Appl. Supercond.* **3**, 3043 (1993).

[69] J. Krupka, K. Derzakowski, M. Tobar, J. Hartnett, and R. G. Geyer, *Meas. Sci. Technol.* **10**, 387 (1999).

[70] P. J. Petersan and S. M. Anlage, *J. Appl. Phys.* **84**, 3392 (1998).

[71] J. Baker-Jarvis, M. D. Janezic, and J. Krupka, in 2006 International Conference on Microwaves, Radar Wireless Communications (2006), pp. 1093–1096.

[72] Y. Li, J.-L. Liu, T.-S. Chao, and S. Sze, *Comput. Phys. Commun.* **142**, Conference on Computational Physics 2000: "New Challenges for the New Millenium", 285 (2001).

[73] B. M. A. Rahman, F. A. Fernandez, and J. B. Davies, *Proc. IEEE* **79**, 1442 (1991).

[74] J N. Reddy, *An Introduction to Finite Element Method* (Jan. 2006).

[75] M. Clemens and T. Weiland, *Prog. Electromagn. Res.* **32**, 65 (2001).

[76] CST MICROWAVE STUDIO, `https://www.cst.com/products/cstmws`, Accessed: 2019-02-19.

[77] CST MICROWAVE STUDIO, *Workflow & Solver Overview* (2015).

[78] CST MICROWAVE STUDIO, *Understanding Time Domain Meshing in CST MICROWAVE STUDIO* (2010).

[79] M. Thiemann, *Master thesis*, University of Stuttgart (2014).

[80] M. Zinsser, *Master thesis*, University of Stuttgart (2018).

[81] V. Engl, *Master thesis*, University of Stuttgart (2019).

[82] D. Davoudi, *Master thesis*, University of Stuttgart (2019).

[83] J. Krupka, R. G. Geyer, M. Kuhn, and J. H. Hinken, *IEEE Trans. Microw. Theory Tech.* **42**, 1886 (1994).

[84] T. Konaka, M. Sato, H. Asano, and S. Kubo, *J. Supercond.* **4**, 283 (1991).

[85] E. S. Sabisky and H. J. Gerritsen, *J. Appl. Phys.* **33**, 1450 (1962).

[86] R. A. Parker, *Phys. Rev.* **124**, 1719 (1961).

[87] D. Hafner, M. Dressel, O. Stockert, K. Grube, H. v. Löhneysen, and M. Scheffler, in Proceedings of the International Conference on Strongly Correlated Electron Systems (2013).

[88] D. Hafner, M. Dressel, and M. Scheffler, *Rev. Sci. Instrum.* **85**, 014702 (2014).

[89] M. Beutel, *Master thesis*, University of Stuttgart (2016).

[90] C. Chase, E. Maxwell, and W. Millett, *Physica* **27**, 1129 (1961).

[91] G. J. Grabovskij, L. J. Swenson, O. Buisson, C. Hoffmann, A. Monfardini, and J.-C. Villégier, *Appl. Phys. Lett.* **93**, 134102 (2008).

[92] F. London and H. London, *Proc. Roy. Soc. A* **149**, 71 (1935).

[93] M. Tinkham, *Introduction to Superconductivity* (McGraw Hill, 1996).

[94] H. A. Wheeler, *Proc. IRE* **30**, 412 (1942).

[95] C. Collignon, B. Fauqué, A. Cavanna, U. Gennser, D. Mailly, and K. Behnia, *Phys. Rev. B* **96**, 224506 (2017).

[96] M. Kunze, in 2011 IEEE MTT-S International Microwave Symposium (2011), pp. 1–4.

Deutsche Zusammenfassung

Viele dielektrische Materialien sind Gegenstand aktueller Forschung, wobei zwei von besonderem Interesse sind: $SrTiO_3$ und nano-eingeschlossene Wassermoleküle in Einkristallen.
$SrTiO_3$ befindet sich bei tiefen Temperaturen in einer paraelektrischen Phase, und die Dielektrizitätskonstante kann mit einem einem Curie-Weiss Verhalten beschrieben werden. Ein vollständiger Phasenübergang wird jedoch nicht erreicht, was sich anhand einer Sättigung der Permittivität bemerkbar macht. Der Grund für dieses paraelektrische Quantenverhalten sind Quantenfluktuationen. Die Dielektrizitätskonstante von $SrTiO_3$ ist stark richtungs-, temperatur- und frequenzabhängig und erreicht Werte von bis zu 20000.
Es werden geeignete Kandidaten benötigt, um Wassermoleküle in Einkristallen einzuschließen und das paraelektrische Quantenverhalten beobachten zu können. Solche sind beispielsweise Beryll oder Cordierite. Die Wassermoleküle werden während des Kristallwachstums eingeschlossen und kommen in zwei Konfigurationen vor: Entweder mit dem elektrischen Dipolmoment senkrecht (Typ 1) oder parallel (Typ 2) zur c-Achse des Kristalls. In Konfiguration Typ 1 eingeschlossene Wassermoleküle zeigen paralelektrisches Verhalten. Die Wassermoleküle befinden sich in einer gewissen Distanz zueinander, die Wasserstoffbrückenbindungen sind unterdrückt, wohingegen die Dipol-Dipol-Wechselwirkungen erhalten bleiben. Wie für $SrTiO_3$ kann die Dielektrizitätskonstante mit einem Curie-Weiss Verhalten beschrieben werden und sättigt bei tiefsten Temperaturen aufgrund Quantenfluktuationen. Die Permittivität von eingeschlossenen Wassermolekülen erreicht Werte von maximal 20. Messungen mit eingeschlossenem Wasser in Beryll wurden bei THz-Frequenzen durchgeführt, während es noch keine Messungen von Cordierite im Mikrowellenbereich gibt.
Es gibt unterschiedliche Hochfrequenz-Messmethoden um dielektrische Eigenschaften von Bulk-Materialien im GHz-Bereich zu bestimmen. Jede Methode hat Vorteile und Limitierungen bezüglich Probenmaterial und -form und welche Frequenzen untersucht werden können. Im Allgemeinen werden die Methoden in breitbandige oder diskrete Messungen unterteilt. Bei breitbandigen Untersuchungen durchdringt die elektromagnetische Welle das Material und verschiedene Frequenzen können gemessen werden. Diese Methoden haben den Nachteil, dass sie ungenau sind und Verluste die Messung beeinflussen. Für Messungen mit Bulk-Proben ist die Genauigkeit jedoch von besonderem Interesse, deshalb sind resonante Methoden gut geeignet. Resonante Methoden werden speziell für die zu untersuchende Probe modifiziert und können nur bei einer einzelnen Frequenz des gesamten Spektrums gemessen werden. Speziell für frequenzabhängige dielektrische Eigenschaften ist dies trotz genauer Ergebnisse ein großer Nachteil.
Mit Mikrowellen-Wellenleiterresonatoren können mehrere diskrete Frequenzen gemessen werden. Speziell planare Mikrowellenresonatoren sind von großem Interessen. Neben einer fundamentalen Resonanzfrequenz werden auch harmonische Vielfache untersucht und liefern gleichzeitig genaue Messergebnisse. Ein weiterer Vorteil der planaren Resonatoren ist die

vergleichsweise einfache Herstellung, genau wie ein simple Probenvorbereitung. Bisher wurden planare Resonatoren erfolgreich für Messungen von dünnen Filmen verwendet, wohingegen Bulk-Proben kaum mit dieser Methode untersucht wurden.

Das Ziel dieses Projektes ist die Entwicklung einer neuen Messmethode für dielektrische Bulk-Proben im GHz-Bereich. Dafür wurde ein neuer resonanter Ansatz entwickelt, welcher die Distanz-Flip-Chip-Montage nutzt. Hierbei wird ein koplanarer $\lambda/4$-Resonator verwendet, der induktiv oberhalb einer Feedline einkoppelt. Die Dielektritzitätskonstante der Probe wird bestimmt, indem die Resonanzfrequenzen dieser Geometrie untersucht werden.
In dem ersten Teil wurde eine andere resonante Messmethode untersucht, bei der die Bulk-Probe auf dem planaren Mikrowellenresonator angebracht wird und als Störung der Geometrie fungiert. Aufgrund der Probe ändert sich die effektive Dielektrizitätskonstante und die daraus resultierende Frequenzverschiebung liefert Informationen bezüglich der dielektrischen Eigenschaften. Wie bereits oben beschrieben, wurde diese Messmethode für dünne Filme erprobt. Das angeeignete Wissen wurde für die Messung mit Bulk-Proben übertragen, es mussten jedoch einige Herausforderungen beachtet werden. Sowohl die elektrische Feldverteilung innerhalb der Probe, als auch die Oberflächenbeschaffenheit ist unterschiedlich, wenn ein dünner Film oder eine Bulk-Probe untersucht werden. Mithilfe von Simulationen und Experimenten wurden zwei verschiedene planare Geometrien getestet: ein koplanarer $\lambda/4$-Resonator und ein Microstrip $\lambda/2$-Resonator. Es konnte gezeigt werden, das beide Ansätze nicht geeignet für dielektrische Messungen von Bulk-Proben sind. Aufgrund des zusätzlichen Spalts zwischen Resonator und Probe, welcher durch Unreinheiten und Rauheit an den Oberflächen entsteht, kann das elektrische Feld die Probe nicht ausreichend durchdringen.
Bei der neu entwickelten Messmethode gibt es keinen solchen Spalt, da der Resonator direkt auf der zu untersuchenden Probe hergestellt wird. Mit der Distanz-Flip-Chip-Montage regt die Feedline den oberhalb liegenden Resonator an. Dabei geschieht die Einkopplung über den Abstand zwischen Feedline und Resonator. Zunächst wurde diese Geometrie mit Simulationen getestet und es wurde gezeigt, dass die simulierten und analytischen Resultate für Dielektrizitätskonstanten bis 300 bezüglich Resonanzfrequenz übereinstimmen. Weiterhin wurde die Kopplung des Resonators mit Simulationen optimiert, indem die beiden relevanten Koppelparameter Abstand h und Länge des Koppelarms l_c überprüft wurden.
Im Experiment ist die Geometrie realisiert worden, indem das leitende Material Cu für die Feedline auf einem Al_2O_3-Substrat verwendet wird, während die Resonatoren aus dem supraleitenden Nb hergestellt werden. Die untersuchten Proben waren TiO_2, MgO and LAO, deren Dielektrizitätskonstante von 10 bis 250 reicht. Das Al_2O_3-Substrat mit der Feedline konnte für jede Messung verwendet werden, während die Resonatoren mit unterschiedlicher Länge hergestellt wurden um verschiedene Frequenzen abzudecken. Es sind Messungen bis zu 20 GHz möglich, da auch harmonische Vielfache der Grundfrequenz untersucht werden. Die untersuchten Materialien zeigen keine Frequenz- und Temperaturabhängigkeit, was durch die Literatur vorhergesagt ist. Die Messungen sind möglich bis zu tiefen Temperaturen von 1.4 K. Da die Eindringtiefe des Nb temperaturabhängig ist, ist eine Korrektur der gemessen Ergebnisse nötig. Die Güten der Resonatoren erreichen Werte von mehreren Tausend und sinken mit zunehmender Temperatur. Die Absolutwerte von ϵ_1 der gemessen Proben stimmen gut mit den Literaturwerten überein. Dadurch eignet sich die entwickelte

Messmethode um Bulk-Proben mit verschiedensten Werten von ϵ_1 zu untersuchen. Weiterhin schränkt die Distanz-Flip-Chip-Geometrie die Probendicke nicht ein. Es können dickere oder dünnere Proben als die, in diesem Projekt verwendeten Dicken, untersucht werden. Außerdem ist die Methode geeignet, um in Zukunft temperatur- oder frequenzabhängige Materialien zu untersuchen. Prominente Beispiele sind STO oder eingeschlossene Wassermoleküle in Einkristallen. Um höhere Temperaturen zu erreichen, muss statt des Nb ein anderes Leitermaterial verwendet werden, beispielsweise Hochtemperatursupraleiter oder Cu.

Eigenständigkeitserklärung

Ich versichere hiermit, dass ich die vorliegende Arbeit selbständig verfasst habe. Es wurden keine anderen als die angegebenen Quellen benutzt und alle wörtlich oder sinngemäß aus anderen Werken übernommenen Aussagen als solche gekennzeichnet. Diese Arbeit wurde weder vollständig, noch in Teilen in einem anderen Prüfungsverfahren verwendet und weder vollständig noch in Teilen bereits veröffentlicht. Der Inhalt des elektronischen Exemplars stimmt mit dem des Druckexemplars überein.

Stuttgart, den 09. April 2019